


UNIVERSITÀ DEGLI STUDI DI CAGLIARI

DOTTORATO DI RICERCA IN FISICA – XXVIII CICLO

Optical and Structural Characterization of Metal Oxides and Carbon Nitride Compounds for the Development of Organic/Inorganic Hybrid Systems

Settore Scientifico Disciplinare di Afferenza: FIS/01

Presentata da: Luigi Stagi

Coordinatore dottorato: Prof. Alessandro De Falco

Tutor: Dr. Pier Carlo Ricci

Esame finale Anno Accademico 2014-2015

Contents

Introduction

Metal oxides (MOs) play a key role in many areas of chemistry, physics and materials science. They are characterized by a wide variety of high technological interest compounds (e.g. TiO_2, Fe_3O_4, Fe_2O_3, Y_2O_3, ZnO). The still increasing interest for this class of materials is mainly due to the ability to take advantage of their diversity to find new important applications in several research field. Their applicability, strengthened by the low cost, safety, ease of synthesis, ranges from (photo)catalysis to microelectronics and in vivo biological studies. Most of the MOs-based devices present outstanding performance derived by their reduced dimensions. To date, the research on nanostructured MOs is highly active in order to deeper gain knowledge about surface states and their influence on chemical and physical properties, motivating an always more multidisciplinary approach.

A key theme in the study of nanostructured MOs is the issue of the crystallographic phase transformations. In general, it is recognized that at the decrease in the size of the physical system, its structure can undergo a transformation to a thermodynamically more stable phase with greater ease. Research in this area is very active, focusing on an in-depth study of different parameters such as grain size, impurities and structural defects.

The information that can be acquired from this basic study is extremely important for applications. Take the example of titanium dioxide systems, whose main crystalline phases, anatase and rutile, have different physical and chemical characteristics and therefore different fields of application, both as single phases and as multiphasic systems. Alternatively, let us consider iron oxide systems, whose magnetic properties deriving from nanoscaled dimensions can be changed after a transformation process.

It is well-known that one of the causes that contribute to promote the phase transformation is the presence of intrinsic defects such as oxygen or metal vacancies, or interstitial and antisite defects. By studying bulk and surface defects, one can learn to efficiently control the phase transformation and the conditions of the structural stability.

However, even controlling the crystal phase, some characteristics of oxides can limit their use, e.g. high band gap with almost negligible absorption in the visible, lack of optical response (luminescence) or not conduction band edge not sufficiently negative to promote proton reduction (limited photocatalytic activity). The introduction of doping elements in the MO matrix to reduce this limitations can have the drawbacks of the new defects generation at the surface and/or in the bulk. Other limitations can be overcome by creating hybrid materials, such as organic and inorganic systems. In such scenario, it is necessary a detailed study aimed to characterize the properties of organic material and the means of implementation of the hybrid system.

To avoid losing the mentioned advantages by using the metal oxide, it is also required ease, environmental safety and even high yield synthesis for the organic. Moreover, it must provide those properties for which the oxide is deficient, including good absorption in the visible or good emission efficiency in a precise spectral region.

The other important aspect is the correct functionalization of inorganic system. Many of the difficulties in the realization of the hybrid is the adhesion and anchoring of the molecules on the surface of the oxide. One has to face the problem of surface sites, where the organic molecule can adhere and the nature of bonds. Most of the performances of the final composite system depend on the strength of organic-inorganic interactions.

The nature of the organic part, the functional groups and stability, allows to determine the conditions for the activation of the surface interacting sites, such as the environmental conditions, the solvent and the temperature of the reaction.

In this work, we will give a prominent place to optical techniques because of the well-known non-destructive approach on the materials characterization. Raman spectroscopy were employed as a fingerprinting procedure accessing to the structural properties and surface states. Steady states photoluminescence and time-resolved photoluminescence methods were utilized to explore the optical properties related to the structure features.

To complete the investigation, we made use of a combination of XRD and TEM in order to clarify the structures and morphologies of considered materials.

This thesis is organized in three sections. The first chapter examines the stability of some exemplar metal oxides systems by the combined use of Raman spectroscopy, Transmission Electron Microscopy, X-ray Diffraction. The aim of this work is to extend the comprehension of nanostructured MOs phase transformation and to analyse the conditions for which the transformation takes place. Steady state and time-resolved photoluminescence spectroscopy performed on different surface conditions of MOs systems (chemical passivation, poor oxygen atmospheres and thermal treatments) allowed us to correlate the transition mechanism with the creation of oxygen vacancies at the surfaces and, consequently, we acquired some important information in order to better control the material surface states.

The second chapter presents a study on carbon nitride (CN) based molecular materials performed with spectroscopy experiments and ab-initio calculations. Our characterizations reveal that CN materials present high chemical and physical stability and good control of the optical properties. XRD patterns and Raman spectra were analysed to deeper investigate the morphological behaviour of the polymers as a function of the synthesis conditions. Bearing the results in mind, we tentatively engineered new kinds of triazine-based molecules, examining the role of terminating functional groups on the optical response and stability of the molecule. Among the different structures, we recognized the relevant influence of cyanide group on the thermal stability, allowing to tune the luminescence as a function of temperature treatment.

In the third chapter, we propose a structural and optical characterization of some carbon-nitride/ metal oxides hybrids. Firstly, we focused on the rare earth (RE) doped Y_2O_3 system. Yttrium oxide attracts much attention for its potential applications as a chemically and thermally stable host matrix, showing a high efficient red emission when doped with Eu^{3+}, for a bulk material. However, when reduced to nanoscale, the RE efficiency drastically decreases and the application of the matrix in the ambit of photonic becomes impossible. By using what we learned from our fundamental studies on oxides, we overcame the problem of efficiency losses by the means of MO surface passivation with an organic. The latter revealed the dual role as replacing species for hydroxides quenchers and activators of doping RE by energy transfer mechanism. Concerning to the energy transfer phenomenon among RE ions, we dedicated a study on the exemplar case of Ce and Tb co-doped Y_2SiO_5, whose properties and the inter-ions interaction present a general character.

TiO_2/CN hybrids were realized by chemical methods and atomic layer deposition, stressing the importance of functional and terminating groups of molecular systems. TEM images confirm the achievement of the hybrid structures and time-resolved luminescence measurements highlighted the presence of strong interaction between the organic and inorganic parts.

Finally, we have engineered and realized a heterostructure formed by two organic compounds separated by an inorganic shell, presenting high optical efficiency and wide emission in the visible range optically when pumped in the blue spectral region. The organic systems participate to the large visible emission while the interposed inorganic shell has the double function of preserving the internal organic core and giving the proper linkage of the outset organic shell. This proof of feasibility can be also seen as the starting point for new composite heterostructures further implementable with additional inorganic shells and organic layers.

Chapter 1

Metal Oxides Nanomaterials

1.1 Crystal Structures and Surface Properties of Metal Oxides Nanomaterials

Many of the properties of nanostructured metal oxides greatly depend both on the crystallographic phase and on the surface characteristics. This gave rise to a lively research aimed at studying the basic mechanisms governing the outstanding properties, such as the interactions between nanoparticles, phase stability and interaction with the environment under optical irradiation, in order to improve the performance of devices based on the use of oxides.

In this chapter, we report some results on nanocrystalline metal oxides systems, obtained by the employment of spectroscopic techniques and in situ characterization.

Focus will be placed on the phenomena resulting from surface states and experiments were carried out in different conditions or on systems undergone a treatment of surfaces to increase or inhibit their effects.

In this regard, we will present the results concerning Raman spectroscopy experiments, in which the radiation will have the dual role of probe for the identification of the structural phase and energy source to trigger the reactions.

Finally, we will demonstrate how a suitable treatment of the surface of the nanoparticles is able to significantly increase the structural stability of the nanosystem, thereby providing new ways for synthesis processes aimed at the realization of architectures from new properties.

1.2 Nanocrystalline Titanium Dioxide

Titanium dioxide (TiO_2) is a strategic material for a very wide range of technological applications encompassing production of pigments [1], nonlinear optics devices [2], gas sensor [3], antimicrobial and medical applications [4], catalysts for air and water purification [5], energy storage [6][7]. These applications essentially exploit the TiO_2 chemical and physical wideband-gap semiconductor properties (bandgap larger than 3 eV), high refractive index, efficient charge-transfer processes across interfaces,

hydrophilicity, chemical stability and non-toxicity. Among the others, the material science research is mainly focused on TiO_2 nanostructures for photocatalytic properties [8]–[10], photoassisted hydrogen production from water [11], and dye-sensitized solar cells (DSSC)[11]-[13].

Titanium dioxide is a polymorphic material with three allotropic forms, namely *anatase*, *rutile*, and *brookite*. Characterized by the highest thermodynamic stability at room temperature and pressure, rutile exhibits a tetragonal $P4_2/mnm$ crystalline structure. Instead, brookite and anatase are respectively orthorhombic *Pbca* and tetragonal $I4_1/amd$. The unit cells are drawn in Figure 1.1.

In combination with a high dielectric constant, the large band gap nominates rutile as a natural candidate to semiconductor electronics, where it is widely employed. However, anatase attracts a considerable interest, mostly due to its superior photocatalytic properties [14].

The physical and chemical properties of rutile, brookite, and anatase are affected by size and related surface effects. The size reduction of coherent diffraction domains down to the nanometer range induces, for these TiO_2 systems, a marked change of band gaps and refractive indexes as well as the rates of charge transfer across interfaces. In turn, this results in enhanced photocatalytic properties [8] in the anatase phase, with important consequences for the photoassisted production of hydrogen from water [11], and the efficiency of dye-sensitized solar cells [12],[13]. The enhancement of photoactivity is even larger for nanometer-sized systems containing different TiO_2 phases [14], probably due to an effective separation of charge carriers in the different phases, which suppresses the electron-hole recombination mechanism [14].

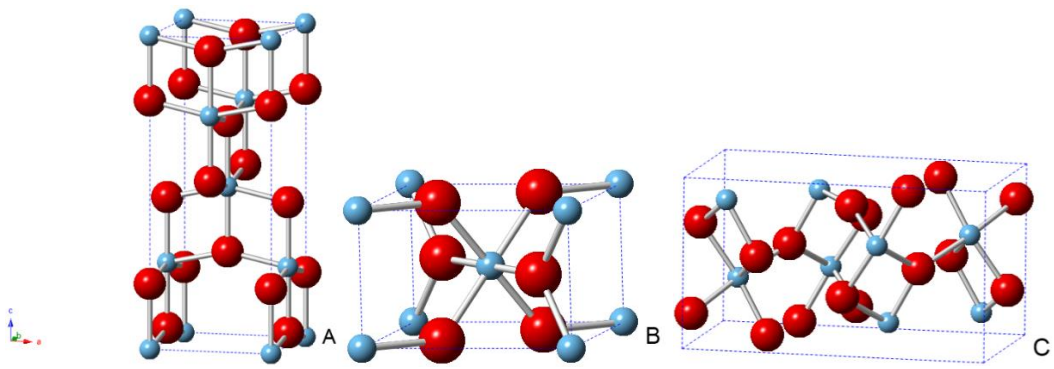

Figure 1.1: Crystal Structure of TiO_2. (A) Anatase ($I4_1/amd$), (B) Rutile ($P4_2/mnm$), (C) Brookite (Pbca).

1.2.1 Raman Spectrum of TiO_2 Nanoparticles and the Quantum Confinement

The crystal phases of TiO_2 samples can be clearly identified by Raman spectroscopy. The anatase phase belongs to space group D_{4h}^{19} - $I4_1/amd$ and it presents 15 optical modes. Accordingly the reduced representation is

$$\Gamma_{opt} = A_{1g} + 2A_{2u} + 2B_{1g} + B_{2u} + 2E_u + 3E_g \quad (1.1)$$

where B_{2u} is inactive, whereas A_{1g}, B_{1g} and E_g are Raman active modes and the A_{2u} and E_u are infrared active modes.

Rutile TiO_2 crystallize in D_{4h}^{14} - $P4_2/mnm$ space group and it reduced representation is

$$\Gamma_{opt} = A_{1g} + A_{2g} + A_{2u} + 2B_{1u} + B_{1g} + B_{2g} + E_g + 3E_u \quad (1.2)$$

where A_{1g}, E_g, B_{1g} , B_{2g} and E_u, A_{2u} are Raman and Infrared active modes respectively. A_{2g} and B_{1u} are inactive.

The Raman frequencies for anatase bulk structures are 144 (E_g)*, 197 (E_g), 399 (B_{1g})*, 513−519 cm^{-1} (A_{1g} mode superimposed with B_{1g} mode)*, and 639 (E_g)* cm^{-1}, with the strongest vibrations identified by asteriks. Rutile Raman frequencies are 143 (B_{1g})*, 447 (E_g)*, 612 (A_{1g})*, and 826 (B_{2g}) cm^{-1}.

The Figure 1.2 shows the unpolarized Raman spectrum of TiO_2 nanopowders collected at room temperature (rutile Sigma-Aldrich (634662), particle size <100 nm).

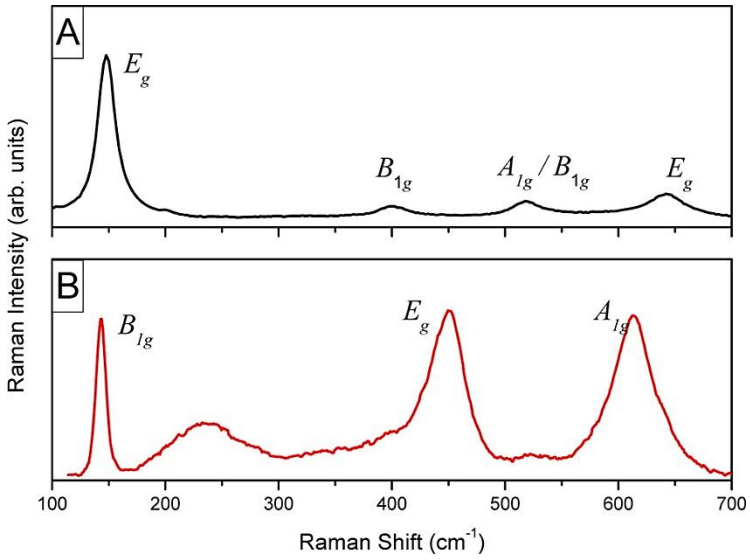

Figure 1.2 : Raman spectra of TiO_2 anatase (A) and rutile (B) nanoparticles.

In anatase spectrum (Fig. 1.2A), a significant deviation from bulk value of E_g mode (144 cm^{-1}) at high wavenumbers (148 cm^{-1}) is observed. We attributed this effect to phonon confinement (PC). In a perfect extended crystal, only the phonons closer to the center of the Brillouin zone (BZ) contribute to the inelastic scattering of an incident radiation. Conversely, a larger portion of the BZ is allowed to effectively participate in scattering processes when the crystal is nanometer sized, due to the weakening of the general selection rule $q_0 \approx 0$. Therefore, both the position and shape of the bands in the Raman spectra can change.

Assuming nanocrystals of spherical shape, the Raman intensity at first order can be written as [15]

$$I(\omega) = \int \frac{|C(0,\boldsymbol{q})|^2 d^3\boldsymbol{q}}{[\omega-\omega(\boldsymbol{q})]^2+(\Gamma_0/2)^2} \tag{1.3}$$

$$|C(0,\boldsymbol{q})|^2 = \exp\left(-\frac{q^2d^2}{16\pi^2}\right) \tag{1.4}$$

where the integral is extended to the Brillouin zone (BZ), Γ_0 is the Raman linewidth, *d* the diameter of nanoparticle and $\omega(\boldsymbol{q})$ is the phonon frequency. Using the approximation of a spherical BZ and an isotropic dispersion curve, the Raman mode E_g can be interpreted by the relationship

$$\omega(q) = \omega_0 + \Delta[1 - \cos(qa)] \tag{1.5}$$

where $\Delta = 20$ cm^{-1} , $a = 0.3768$ and $\omega_0 = 144$ cm^{-1}.

Since the nanopowder exhibit the main peak of the E_g mode at 148 cm^{-1}, we can estimate an average dimension of 10 nm for the analyzed nanoparticles.

In Figure 1.2B, the reference spectrum of rutile powders is reported: besides the main vibrational peaks, the typical contribution of the second-order scattering at 235 cm^{-1} is observed.

1.2.2 Surface related luminescence in TiO_2 Nanoparticles

The photocatalytic performance of TiO_2 materials are determined by recombination process of photogenerated charge carriers [16]. Among the most profitable experimental techniques for the comprehension of the recombination mechanism, we include Electron Paramagnetic Resonance (EPR) and time resolved IR spectroscopy. However, photoluminescence (PL) and time-resolved (TRPL) experiments are now frequently employed to low quantum yield materials, such as TiO_2, thanks to the

availability of continuous and pulsed light sources, often with high brightness. It has been revealed that the carrier relaxation process is highly dependent on the excitation intensities and energies, leading to different results. In particular, under high power densities the electron-hole recombination lifetimes is in the order of few nanoseconds, attributed to fill trapping. On the other hand, slow recombination takes place in weak intensity regime. Consequently, our experiments has been performed in the weak intensity regime, aimed to explore the surface dependent luminescent response.

1.2.2.1 Experimental details

Two sets of TiO_2 powders were investigated. The first set was prepared by sol–gel technique, with the preliminary formation of an amorphous solid (xerogel) and a subsequent thermal treatment of the final powders at 300 °C for 6 h under oxygen stream. The average crystallite size is about 10 nm [17].

The second set of dry anatase phase TiO_2 powders was provided by Plasmachem (PL-TiO-NO) the average particle size of the commercial samples is 4–8 nm. The surface of these samples (hereafter "TiO_2–HNO_3") was passivated with HNO_3. In order to perform light irradiation and Raman measurements TiO_2 nanoparticle powders. The powders were illuminated with different power excitation beam focused through a 10X objective with 0.25 NA, allowing the exposure of about 2500 mm^2 of sample surface to irradiation with a light penetration depth of about 10 μm for intrinsic excitation (the optical absorption was considered negligible at the irradiation wavelength) with the applied objective. Raman scattering measurements were carried out in backscattering geometry using a 405.0 nm line by a wavelength stabilized diode module (Ondax Inc., Surelock LM series) coupled with a Reflecting Bragg Grating (Optigrate–Braggrade 405) to narrow the laser line. Measurements were performed at room temperature with a triple spectrometer Jobin-Yvon Dilor integrated system with a spectral resolution of about 1 cm^{-1}. Spectra were recorded in the Stokes region by a 1200 groove/mm grating monochromator and a Liquid nitrogen-cooled charge coupled device (CCD) detector system.

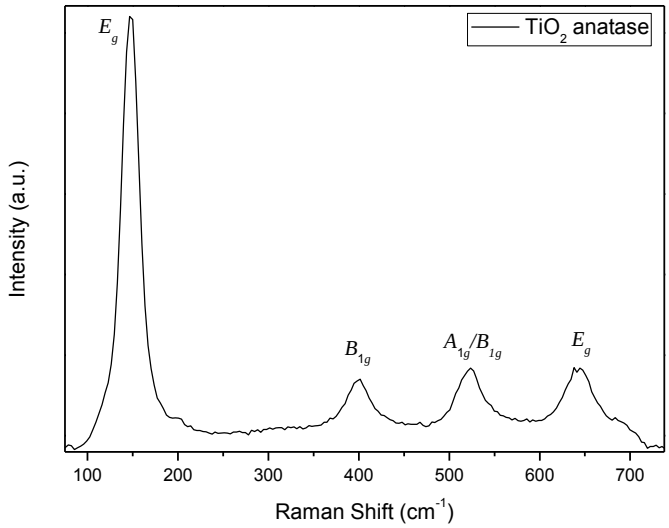

Figure 1.3: Raman spectra of as-prepared TiO_2 nanoparticles.

1.2.2.2 Results and discussion

Figure 1.3 shows the Raman spectrum of TiO_2 nanoparticles prepared by the described sol-gel technique. As prepared nanopowders present the characteristic modes of pure anatase at 148, 399, 520 and 619 cm^{-1}.

Figure 1.4 reports the steady time luminescence spectrum of TiO_2 sample with excitation wavelength at 405 nm, where a large and asymmetrical band centered at about 470 nm is observable. To deeper investigate the character of anatase emission, we performed time resolved measurements, excited at 405 nm, with gated technique (see Appendix 1), pointing out the double nature of the band. At 0.1 μs from the excitation pulse (with gate 0.05 μs) the spectral profile reveals two components: a principal fast component (with lifetime in the order of few tens of ns) centered at 470 nm, i.e. the maximum in steady state excitation, and a slower component (in the ms range) centered at about 600 nm (fig. 1.5).

The time features of the photoluminescence band were studied in details. Figures 1.6A and 1.6B report the time decay curves. The times of decay for the two components are estimated through a single exponential decay fit

$$I(t) = I_0 e^{-\frac{t}{\tau}} \quad (1.6)$$

and results in τ_1 = 33 ns and τ_2 = 1.4 ms, respectively.

In order to investigate the contribution of surface defects to the reported experimental evidences, we first created oxygen vacancies at the surfaces of the TiO_2 nanopowder by treating the samples in vacuum at 200 °C for 3 h [18],[19]. The treated samples present an intense blue luminescence and the component relative to the emission at 600 nm is more pronounced. For sake of clarity, the PL spectra of pristine and treated samples are reported in the same graph (fig. 1.7).

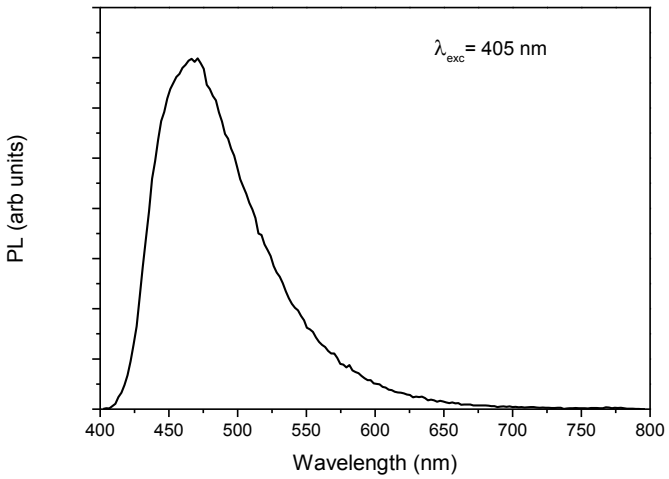

Figure 1.4: Steady time luminescence spectrum of TiO_2 sample with excitation wavelength at 405 nm.

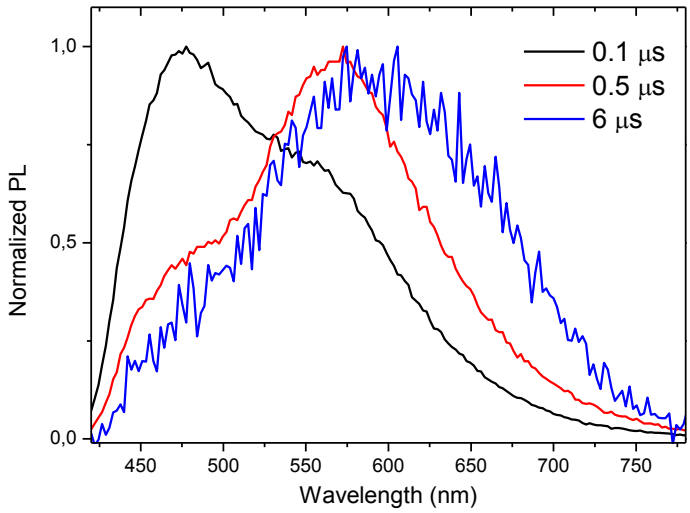

Figure 1.5: Spectral profile at different delay time from the excitation.

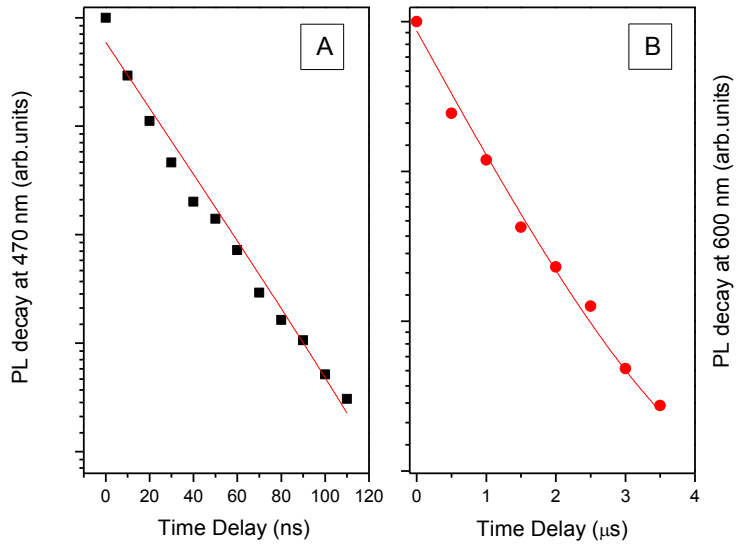

Figure 1.6: Time resolved photoluminescence of TiO_2 sample with excitation wavelength at 405 nm: (A) emission at 470 nm; (B) emission at 600 nm.

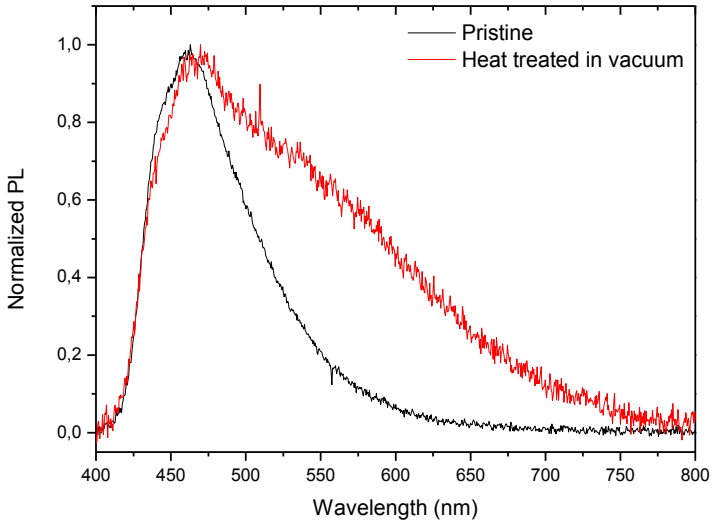

Figure 1.7: Effect of heat treatment in vacuum on steady time luminescence of TiO_2 sample with excitation wavelength at 405 nm. Black spectrum: pristine TiO_2. Red spectrum: TiO_2 after treatment in vacuum at 200 °C for 3 h.

To further understand the role of the surface defects of the anatase TiO_2 nanoparticle, we also performed PL measurements on commercial TiO_2 anatase powder whose surface was intentionally passivated in HNO_3 (TiO_2–HNO_3). The Raman spectrum of TiO_2–HNO_3 sample is reported in Figure 1.8. It shows

the typical anatase vibration modes at 154.5, 456, 519, and 617 cm^{-1} where the peak positions as well as the full width at half maximum are different with respect to the spectra of bulk TiO_2 due to phonon confinement effect [15].

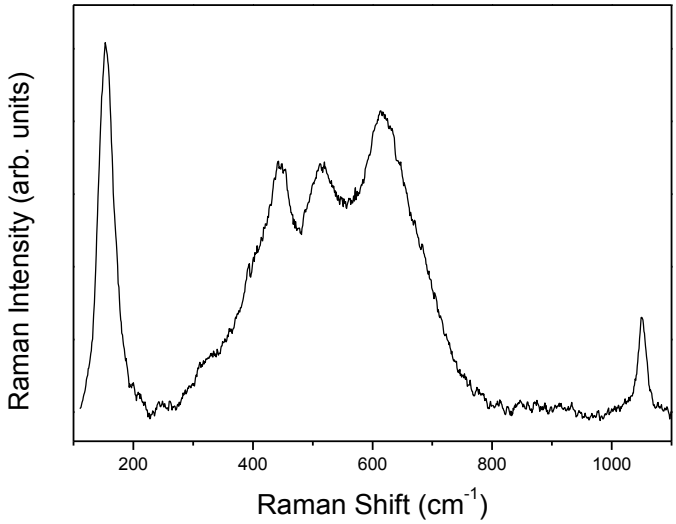

Figure 1.8: The Raman spectrum of TiO_2-HNO_3 sample.

In addition, there is a marked increase of background in the region 400-800 cm^{-1} drastically influencing the intensity ratios among the active modes and it is clearly detectable the band at 1050 cm^{-1} . The latter mode is characteristic of the νν(NO) stretching vibration of NO_3^- groups when bound at the surfaces of metal oxides [20]. On the other hand, the wide background suggests the presence of HNO_3 residuals, whose Raman modes are at 615 (bending) , 619 (torsion), 680 (bending) and 773 cm^{-1} (torsion) [21],[22]. It is widely accepted that NO_3^- groups on the TiO_2 surfaces are strongly bonded at the oxygen vacancies sites, where they replace the naturally formed OH^- group [23]–[25].

It is important to emphasize that in this class of samples no luminescence was detected by intragap excitation at 405 nm, revealing a role of the surface passivation at defects sites. Additionally, after the removal of nitric groups in vacuum at 80°C, testified by the disappearance of the mode at 1050 cm^{-1}, the luminescence emission is reactivated (fig.1.9).

The luminescence in TiO_2 nanocrystals was widely studied in the past but only in the last years the interest on this phenomenon is rising [26]–[29]. Although the presence of defects can be easily and efficiently proved by photoluminescence measurements, the assignment of the different bands is not a

trivial exercise. Recently, the PL emission at about 470 nm was associated with surface and/or interface defects in the form of vacant O sites (the $_5Ti^{3+}$ species) [28],[30], this assignment being in agreement with our results and, in particular, with the quenching of the PL band by NO_3^- groups at the surfaces.

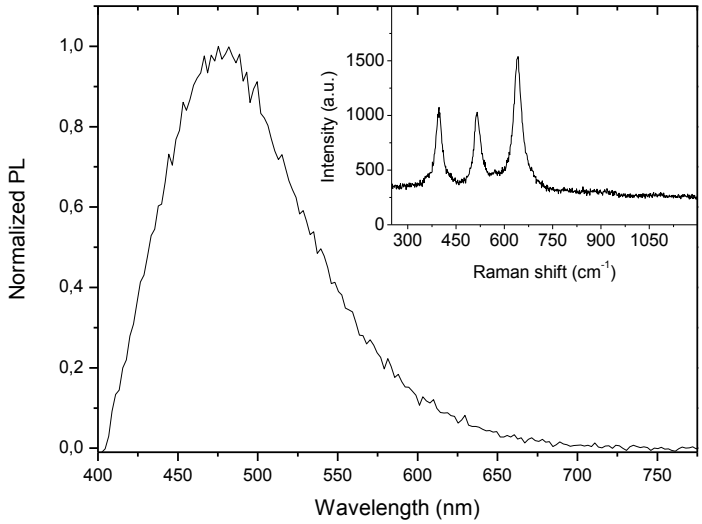

Figure 1.9: Steady time luminescence spectrum of TiO_2-HNO_3 sample, after treatment in vacuum at 80°C (3h) under excitation wavelength at 405 nm. Inset: particular of Raman spectrum among 250-1200 cm^{-1}.

The band at 600 nm was previously related to oxygen vacancies too. However, the increase of the ratio between the two bands after thermal treatment in vacuum suggests a role of the passivating group. Taking into account that the sample was kept in air after the thermal treatment, we reckon that the species at the surfaces are OH groups, bonded at the Ti^{3+} sites. This attribution is supported by the experimental results on H-treated sample of reference [28] and [30]. It was found that the hydroxyl group preferentially adsorb at the fivefold coordinated (Ti5c) sites and desorption/adsorption process can be activated and accelerated by visible light excitation. Hence, the stability of TiO_2 surface largely depends on both surface passivation and light excitation.

1.3 Phase Transformation in metal oxides nanomaterials

As previously stated, the phase stability of metal oxides nanosystems can be highly dependent on the nature of surfaces, whose contribution to the total energy grows with decreasing size of the system.

1.3.1 The case of TiO_2

As asserted, the photoactivity is larger for nanometer-sized systems containing different TiO_2 phases, probably due to the suppression of the electron-hole recombination determining an effective separation of charge carriers [32].

Within this framework, achieving a suitable control of the phase transition behavior of nanometer-sized TiO_2 materials would represent a significant progress on the way of their full exploitation in different areas of science and engineering [14]−[35]. In this regard, it must be noted that also the relative thermodynamic stability of rutile, brookite, and anatase is affected by size effects. In particular, anatase becomes the most stable phase as the size of coherent diffraction domains is smaller than 13−16 nm [36],[37], being the surface energies of rutile and anatase equal to about 1.91 and 1.32 J m^{-2}[37], respectively. Accordingly, the anatase-to-rutile phase transition in nanostructured systems can be induced by raising the temperature above 970 K [38]. Experimental findings suggest that the occurrence of such phase transition is related to the coalescence of neighboring anatase grains at high temperature[36]-[40]. In addition, the phase transition behavior is affected by the initial grain size, chemical surroundings, and impurities [36]-[40].

Along this line, it has been recently pointed out that the irradiation of nanometer-sized anatase particles is able to influence their stability provided that experiments are performed under suitable incident radiation power and oxygen partial pressure conditions [31]. More specifically, it has been shown that the intragap excitation of anatase particles in an oxygen-rich atmosphere promotes the surface adsorption of O_2 molecules, with a stabilizing effect on the existing oxygen vacancies at the particle surface. On the contrary, when irradiation is performed in vacuum, anatase is transformed into an amorphous TiO_2 phase. Such evidence clearly demonstrates that irradiation can significantly affect the relative stability of nanometer-sized TiO_2 structures. Focusing on the response of nanometer-sized anatase to irradiation under different powder density and atmosphere conditions, it can be shown that irradiation is able to induce an athermal anatase-to-rutile phase transition and that the mechanism of the phase transition is strictly connected with the chemistry of TiO_2 surfaces. This effect can throw new light on the intimate nature of the irradiation effects.

1.3.1.1 Experimental details

Samples. Experiments were performed on two sets of anatase powders described in previous paragraph.

Experiments. X-ray diffraction (XRD) methods were used to estimate the average size of coherent diffraction domains. A Rigaku D-Max diffractometer equipped with a Cu Kα radiation tube, and a graphite monochromator in the diffracted beam, was employed. The XRD patterns were analyzed by using the Rietveld method to quantify the average size and the average strain content of coherent diffraction domains [41]. The anatase powders synthesized by the sol-gel method exhibit an average crystallite size of about 10 nm, whereas for commercial ones the crystallite size is given between 5 and 8 nm (5% standard deviation). XRD estimates are in agreement with high resolution transmission electron microscopy (HRTEM) observations. These were performed by using a JEOL JEM- 2200FS microscope, equipped with a field-emission gun working at an accelerating voltage of 200 kV, a spherical aberration corrector (by CEOS GmbH) of objective lens allowing to reach a spatial resolution of 0.9 Å, and an in-column Omega filter. The samples were prepared by dropping dilute solutions of nanocrystals (NCs) onto carbon-coated ultrathin copper grids. Raman scattering measurements were carried out in backscattering geometry by using a triple spectrometer Jobin- Yvon Dilor integrated system and a liquid nitrogen cooled charge coupled-device detector; the spectral resolution was about 1 cm^{-1}. The measurements were performed at room temperature. The powder samples were irradiated in vacuum (5×10^{-5} Torr) or exposed to different gaseous atmospheres, namely air, oxygen, and argon. The same dispersion and detection system was employed to record the photoluminescence spectra obtained in the visible range. Unless otherwise indicated, the Raman spectra were acquired in the Stokes region. Laser irradiation experiments and Raman scattering measurements were carried out on 100 mg powder layers about 1 mm thick deposited on a 25 mm^2 sample holder. The powder samples were irradiated with visible light excitation beams of different power in the 1−10 mW range, focused through a 10X objective with 0.25 NA on a surface area of about 2500 μm^2. Since the excitation beam reaches a penetration depth of about 10 μm, even if it exhibits negligible absorption only a small fraction of powder is effectively irradiated. The powder samples were irradiated with different excitation laser beams in the visible range, including the 488.0 and 514.5 nm lines of an argon ion laser (Coherent,

Innova-90 C), the 632.0 nm line of a He−Ne laser (Spectra-Physics), and the 785 nm of a diode laser (B&WTek).

1.3.1.2 Results and Discussion

The effects of irradiation on nanometer-sized anatase particles can be pointed out by comparing Raman spectra collected at increasing times. A representative sequence of such spectra is shown in Figure 1.10. Data refer to the continuous irradiation of anatase at a wavelength of 488.0 nm under dynamic vacuum conditions, with a residual pressure about 5×10^{-5} Torr. The Raman spectra were collected in the continuous mode, with a sampling time of 1 s, no time interval between consecutive measurements, and a laser beam power of 5 mW. The measurements were performed within the spectral region between 300 and 700 cm^{-1}, where the highly intense Raman-active vibration modes of anatase and rutile allow the easiest identification of the crystal phase. It can be seen from Figure 1.10 that the Raman spectra of irradiated anatase change quickly with time. Initially, the system contains exclusively anatase, as proven by the position of the three peaks at 399, 519, and 639 cm^{-1}. After 1 s, no vibration mode can be identified in the Raman spectrum, which indicates the formation of an amorphous phase. This phase is also characterized by a large and intense photoluminescence (Fig. 1.11). After 2 s irradiation, two large bands at about 445 and 610 cm^{-1} appear in the Raman spectrum overlapped to a residual photoluminescence background. As the irradiation time increases, the two bands increasingly sharpen, whereas the photoluminescence totally quenches. The presence of two bands at 447 and at 612 cm^{-1} in the final Raman spectra clearly indicates the formation of rutile. The exposure of the powder sample to the laser beam for longer times does not result in further changes. The rutile phase formed in the irradiated region of the sample keeps stable also when exposed to air. In the sample regions not directly exposed to laser irradiation the powder keeps the initial anatase phase independently of the sample holder atmosphere. Experiments carried out with laser beams of different power indicate the existence of a light power threshold. In particular, the experimental findings suggest that a minimum power of about 1−2 mW is necessary to activate the anatase-to-rutile phase transition for chamber pressure of about 5×10^{-5} Torr. In addition, it appears that the light power does not affect the stability of the rutile phase, which keeps

its crystalline structure in vacuum even when the power of the 488.0 nm laser is increased up to 10 mW. In principle, the observed phase transition could be ascribed to irradiation-induced thermal effects and a similar scenario has been already discussed in the literature for nanometer- sized anatase particles irradiated in air with a high-power laser [42],[43].

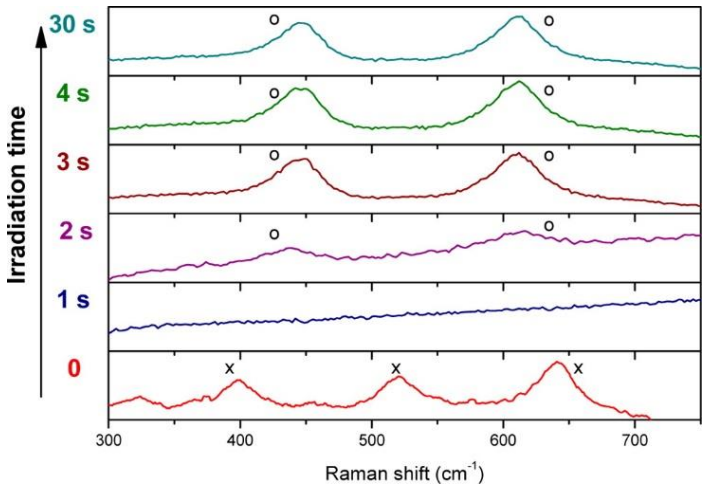

Figure 1.10: Time evolution of the Raman spectrum of TiO_2 anatase nanoparticles under continuous irradiation at 488.0 nm in vacuum conditions (5×10^{-5} Torr). The spectra were recorded at 5 mW of laser beam power. Zero time spectrum refer to the pristine sample conditions; data were recorded with a time step of 1 s. (×) refer to the anatase phase peaks; (○) refer to the rutile peaks.

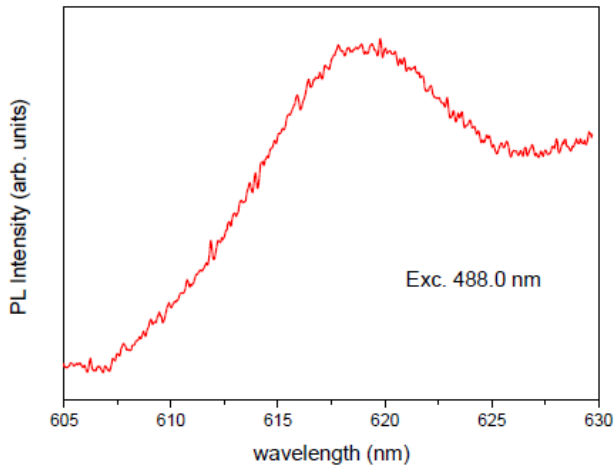

Figure 1.11: Photoluminescence band recorded during laser irradiation. The band is observed when an intermediate metastable disordered phase is formed and it is quenched as the anatase to rutile phase transition is completed.

With the aim of clarifying this issue, the effective temperature of the powder samples during irradiation was estimated by the ratio of the Stokes and anti-Stokes components of the Raman spectrum (fig. 1.12), according to the equation

$$\frac{I^{ST}}{I^{aST}} = \frac{(\tilde{\nu}_0 - \tilde{\nu})^4}{(\tilde{\nu}_0 + \tilde{\nu})^4} e^{\frac{hc\tilde{\nu}}{kT}} \tag{1.7}$$

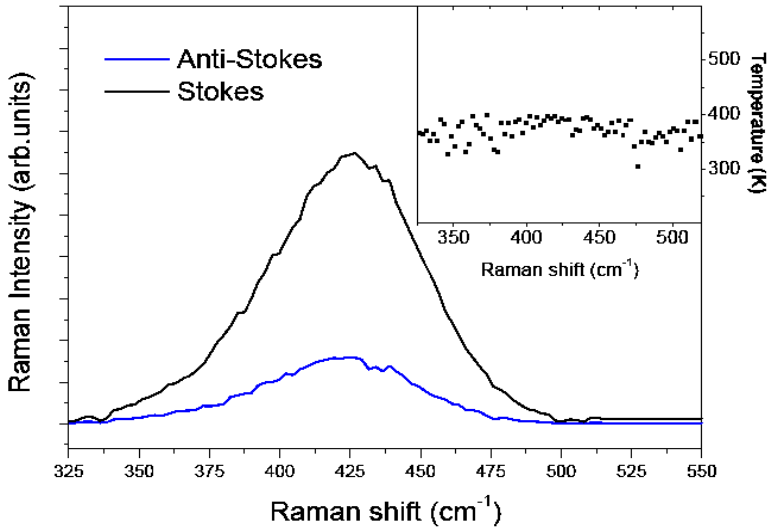

Figure 1.12: Stokes and Anti-Sokes Raman spectra in the 300-500 cm^{-1}. Inset: estimated sample temperature during laser irradiation.

More specifically, the B_{1g} mode of rutile at 445 cm^{-1} was monitored respectively in vacuum for laser beams with a power as high as 5 mW, i.e., roughly 3−5 times higher than the one needed to activate the observed anatase-to-rutile phase transition. The sample was irradiated in continuous mode for time intervals as long as 5 min, yielding an estimated temperature of 371 ± 5 K. Being this temperature well below the one required to activate the phase transition [36],[39], the experiments strongly suggest an athermal mechanism for the observed anatase-to-rutile phase transition.

Two crucial questions arise in connection with the experimental findings heretofore discussed. In the first place, what is the effect of the irradiation wavelength on the observed phase transition? Similarly, what is the effect of the atmosphere to which powders are exposed?

In order to explore the effects of the irradiation wavelength on the phase transition behavior, irradiation experiments at 514.5, 632.8, and 785.0 nm intrinsic excitation wavelengths were carried out. The irradiation of anatase powders with the 514.5 nm wavelength gives rise to the same experimental scenario already discussed for the laser irradiation at 488.0 nm. Conversely, irradiation in the red and near-infrared spectral regions is unable to induce the anatase-to-rutile phase transition (fig. 1.13).

Eventually, the role of the atmosphere to which anatase is exposed during irradiation was investigated by performing experiments under different conditions, namely in oxygen and argon ambient. In oxygen, irradiation is unable to activate any phase transition. Correspondingly, anatase keeps stable up to an excitation power of 10 mW, well above the power threshold required to induce the anatase-to-rutile phase transition at low pressure. Moreover, no photoluminescence background is detected (fig. 1.14).

The results of the Raman measurements performed in argon are shown in Figure 1.15. In this case, the system exhibits the same phase transition trend observed under vacuum conditions. However, the phase transition requires quite longer times to take place, reaching completion after 14 s.

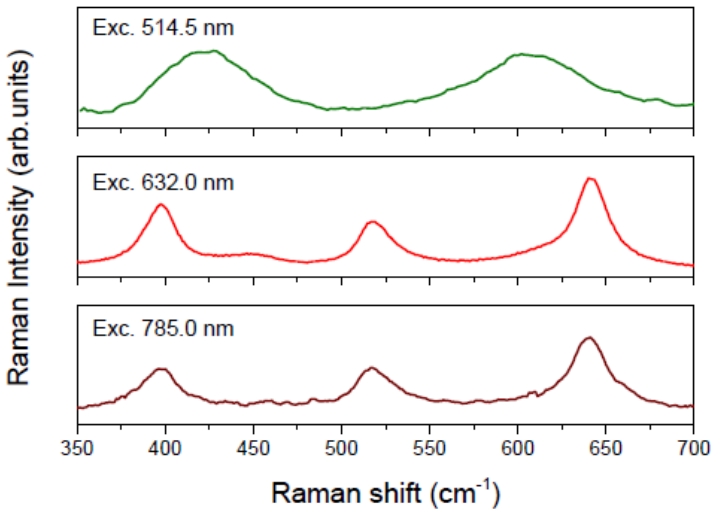

Figure 1.13: Raman spectra of TiO_2 anatase nanoparticles under irradiation at different wavelength in vacuum conditions (5×10^{-5} Torr).

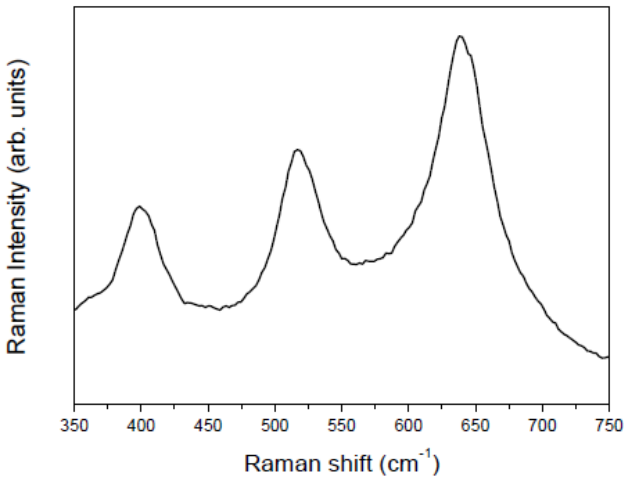

Figure 1.14:Raman spectrum of TiO_2 anatase nanoparticles under continuous irradiation at 488.0 nm in Oxygen atmosphere (excitation power density of 400 W cm^{-2}).

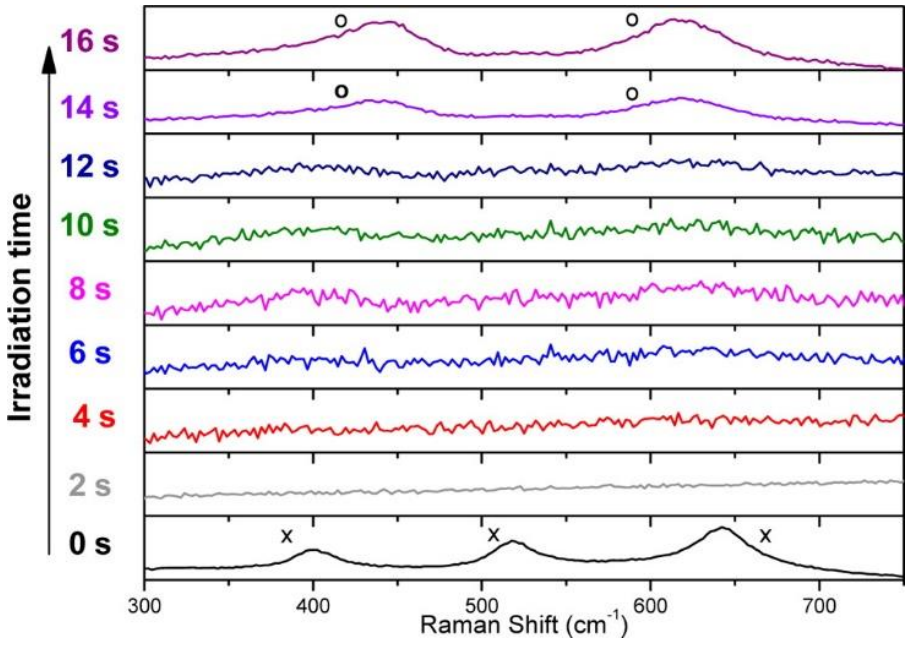

Figure 1.15: Time evolution of the Raman spectrum of TiO_2 anatase nanoparticles under continuous irradiation at 488.0 nm in an argon atmosphere. The spectra were recorded at 10 mW of laser beam power. Zero time spectrum refers to the pristine sample conditions; data were recorded with a time step of 2 s. Crosses refer to the anatase phase peaks; circles refer to the rutile peaks.

To further investigate the interaction among nanoparticles under the phase transformation process, attention was focused on the irradiation behavior of commercial anatase powders that have undergone surface passivation by treatment with a concentrated nitric acid aqueous solution.

Irradiation experiments point out that the surface-passivated anatase is more stable than anatase to irradiation effects. The Raman spectra in Figure 1.16 indicate that under vacuum conditions, the anatase-to-rutile phase transition is partially inhibited and/or takes place after higher laser density (up to 10 mW). In addition, it is worth to note that if the phase transformation is not achieved, the NO_3^- vibrational band at 1050 cm^{-1} is still detected, conversely it disappears once the transformation is observed. After the removal of HNO_3 with the previous described method (80 °C in vacuum) and the restoration of luminescence features, the de-passivized samples shows a quick anatase-to-rutile phase transformation in vacuum and argon atmosphere. This is a further strong indication that the surface of the anatase particles plays a fundamental role in the phase transition trend.

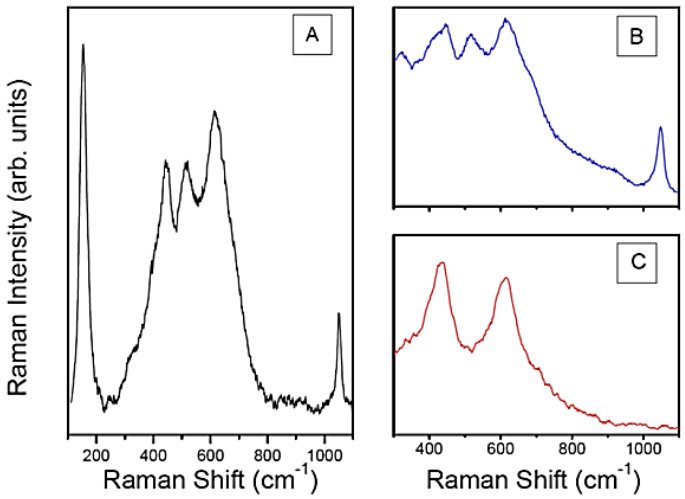

Figure 1.16: The Raman spectrum of TiO_2-HNO_3 sample. (B) Detail of vv(NO) vibrational mode of NO_3^- group at the surface. (C) Light induced phase transition in vacuum after NO_3^- groups removal.

Additional information on the anatase-to-rutile phase transition was gained by XRD and HRTEM analyses. In the former case, the XRD patterns of powder samples irradiated under dynamic vacuum conditions exhibit relatively weak peaks overlapping the intense anatase ones that can be ascribed to the presence of a rutile phase diluted in an anatase matrix (Fig. 1.17). In the light of the very small volume

of anatase effectively irradiated by the laser beams, the low intensity of the rutile XRD peaks can be exclusively related to the very small amount of rutile present in the sample compared with anatase. The Rietveld analysis of the XRD patterns indicates that the coherent diffraction domains of the starting anatase exhibit an average size of about 10 nm, whereas this quantity increases up to about 100 nm for the rutile phase formed by irradiation. Figure 1.18 displays a HRTEM image of representative untreated TiO_2 NCs of less than 10 nm in size. As expected, the NCs, showing elongated shapes, exhibit the lattice sets of anatase, and their size is in accordance with XRD analysis. A HRTEM image of the treated TiO_2 sample showing a small polycrystalline aggregate is reported in Figure 1.18B. Lattice fringes show d-spacing and spatial relationships of two different phases, namely anatase (JCPDS card 84-1286) and rutile (JCPDS card 82-0514); the bidimensional Fourier transform (2D_FT) pattern of the TiO_2 aggregate features contributions arising from different NCs, which were identified and discerned by angular and vector relationships among the spots of reciprocal lattice (inset of Figure 1.18C). The aggregate can subsequently be "broken down" into its nanocrystalline parts and reconstructed as an inverse Fourier transform, where multiple rutile and anatase NCs are identified by different false colors (Figure 1.18C). The presence of rutile in relatively large aggregates was also ascertained by side-aperture electron diffraction (SAED) analyses. A representative pattern is shown in Figure 1.19.

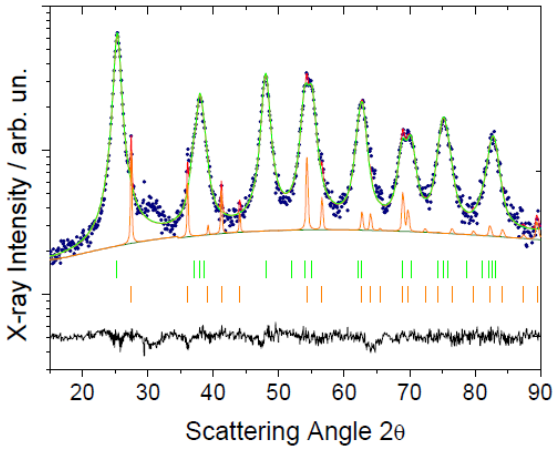

Figure 1.17: XRD diffraction pattern of treated nanoparticles. The sample was irradiated with at 488.0 nm under dynamic vacuum conditions and presents the peak of rutile as a secondary phase. The analysis was conducted also on the average dimension of the crystallites: the anatase particle dimension are estimated in 11 nm while the average dimension of crystallite in rutile phase increases up to 100 nm.

According to the experimental evidence previously discussed, the irradiation-induced anatase-to-rutile phase transition can be ascribed to chemical processes occurring at the surface of nanometer-sized anatase particles. It can be reasonably expected that the athermal mechanism underlying the phase transition relies upon the generation of surface defects due to optical excitation and their subsequent interaction with the chemical surroundings. In this respect, it is well known that irradiation can have quite different effects on nanometer-sized TiO_2 systems depending on the atmosphere surrounding the sample. For example, the irradiation of nanometer-sized anatase particles in air with a laser beam of high power results in a significant increase of their degree of crystalline order [44].

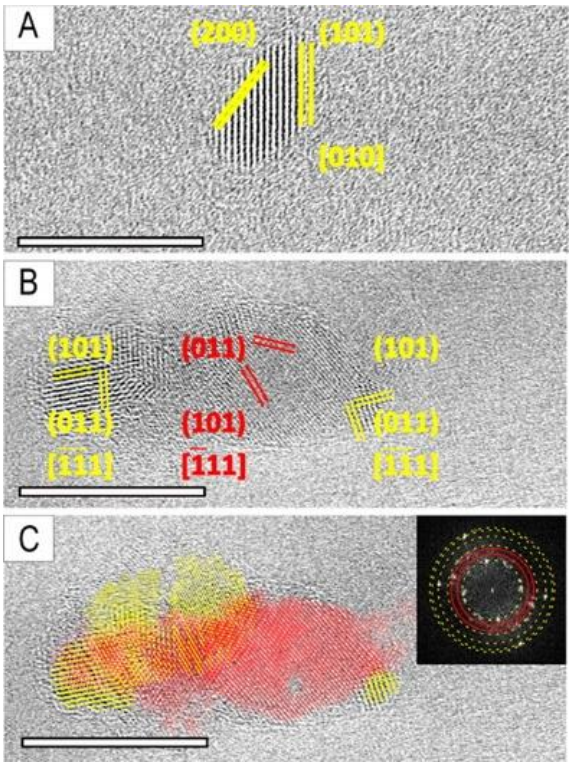

Figure 1.18: (A) HRTEM image of a TiO2 NC with anatase crystal structure observed along the [010] zone axis, exhibiting (101) and (200) lattice sets with measured d-spacings of 3.51 and 1.89 Å. (B) HRTEM of a TiO2 aggregate featuring NCs of rutile and anatase. The rutile NC, observed along the [−111] zone axis (center, in red), exhibits (101) and (011) lattice sets with measured d-spacings of 3.19 Å; anatase NCs, observed along the [−1−1−1] zone axis (left and right, in yellow), exhibit (101) and (011) lattice sets with measured dspacings of 3.51 Å. (C) Reconstruction via inverse fast Fourier transform (IFFT) of the NCs forming the aggregate of point (B): rutile and anatase NCs are depicted in red and in yellow, respectively. The inset features the FFT pattern of the aggregate. Red lines and yellow dotted lines indicate spots of rutile and anatase phase, respectively. All the data bars correspond to 10 nm.

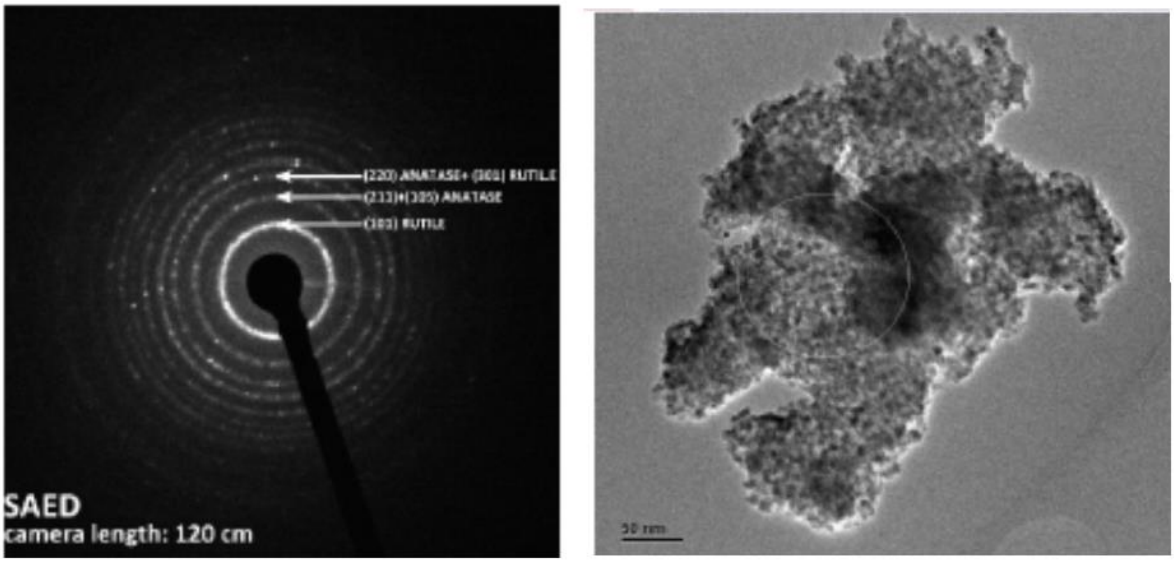

Figure 1.19: SAED pattern (left) and HRTEM image of treated TiO2 nanoparticles. The first circle of SAED corresponds to the diffraction peak (101) of rutile (JCPDS card 82-0514), with distance 2.5130 Å and intensity 458/1000; the second circle presents the unresolved anatase peaks (105) and (211) (JCPDS card 84-1286) with distances of 1.6981 Å and 1.6652 Å, and intensity 158/1000 and 155/1000, respectively. The third circle, correspond to both (unresolved): the peak (220) of the anatase phase (1.3372 Å distance, intensity 55/1000) with the (301) of rutile (1.3459 Å distance, intensity 137/1000).

Also, it was shown that the crystalline phase of anatase nanoparticles can be deteriorated down to an amorphous phase through irradiation at low power density laser beam under vacuum conditions [31].In both cases, the absorption and desorption of oxygen molecules on the surface of nanometer-sized TiO_2 systems are expected to play a fundamental role. When absorbed on the surface, the oxygen molecules are known to behave as efficient electron scavengers. They are able to collect electrons excited from the surface states of the semiconductor to the conduction band and partially compensate for the effects of oxygen vacancies [45]-[47]. As suggested by X-ray photoelectron spectroscopy studies [48],[49] these are responsible for the formation of Ti^{3+} and Ti^{4+} ions as a consequence of electron trapping effects[46]. The absorbed oxygen molecules are expected to stabilize the structure of the TiO_2 surface by bridging two neighboring Ti sites [45]. The desorption of the oxygen molecules absorbed at the TiO_2 surface has been connected with the recombination of the electrons trapped in the monovalent anionic oxygen

molecules with the holes in the photoexcited valence band[45],[50],[51]. Recently, it has been proposed that this photodesorption mechanism must also operate under intrinsic excitation conditions, i.e., when the holes involved in the recombination process underlying the desorption of oxygen molecules derive from charged F centers generated in correspondence of oxygen vacancies[31],[45]. It follows that the electronic excitation of nanometer-sized anatase particles is able to promote both the adsorption and the desorption of oxygen molecules at the particle surface. The relative balance between the two processes will depend on the experimental conditions[31],[52], as confirmed by the results reported in Figures 1.10-1.15. It can be easily inferred that irradiation in an oxygen-poor atmosphere, i.e., under dynamic vacuum conditions or in argon, will result in the excitation of the electrons in the conduction band. In turn, this will induce the desorption of oxygen molecules and a depletion of oxygen atoms at the surface of the nanometersized anatase particles. As the power of the laser beam increases, the number of excited electrons also increases, with a beneficial effect on the rate of the oxygen desorption. According to ref [31], the increasing of the excitation power on the TiO_2 anatase nanoparticles in an oxygen-poor atmosphere (that is, under dynamic vacuum conditions or in an argon-rich environment) generates a high electron density in the conduction band and a rapid depletion of oxygens at the nanoparticle's surface. In this scenario, we reckon that the irradiation-induced desorption of oxygen molecules leaves the particle's surface highly reactive. The enhanced chemical reactivity of these surfaces favors the mutual interactions of neighboring particles, which finally determine the formation of stable polycrystalline aggregates. For example, the chemical decomposition of peroxyl groups at the particle surface can permit to neighboring particles the formation of stable interparticle chemical bonds[53]-[55] The size increase of the coherent diffraction domains of rutile can be regarded as an indication of the above-mentioned aggregation mechanism in the starting anatase powder. Rutile nucleates as a consequence of the irradiation-induced desorption of oxygen molecules from the surface of anatase particles. Under pulsed laser ablation conditions, nanometersized anatase particles exhibit a tendency to coalesce at {112} surfaces, forming faulted and twinned bicrystals that can act as preferential nucleation sites for the rutile phase[56]. Molecular dynamics calculations employing suitable reactive force fields, as well as in situ TEM observations, pointed out that the first stage of the thermally induced anatase-to-rutile phase transition in nanometer-sized particles consists in the formation of chemical bonds between

amorphous and defective surfaces [57]-[59]. In a second stage, the rutile phase nucleates exactly at the twin boundaries generated by anatase {112} surfaces [58],[59]. The relative number of preferential nucleation sites for the anatase-to-rutile phase transition increases as the size of anatase particles decreases and as the population of oxygen vacancies at the particle surface increases.[60],[61]. Once nucleated, the rutile phase undergoes a fast growth, absorbing the neighboring anatase domains into a single coherent crystalline lattice [57],[61],[62]. The transformation of bulk anatase breaks out 7 of the 24 Ti−O bonds per unit cell leading to the cooperative displacement of both Ti and O atoms. The growth of the coherent rutile domain terminates at the anatase surfaces different from the {112} one or at the interface with another rutile domain[57],[61]. It is worth pointing out that in ref [31] the anatase-to-rutile phase transition was not observed, whereas only the degradation of the pristine anatase phase to an amorphous phase was reported. Those experiments were carried out at very low power density laser beam, fixing the excitation wavelength at 488 nm. The maximum power density delivered at the sample was 4 W/cm^2 (about 1/10th of the estimated power density threshold to achieve the anatase to rutile phase transition). In addition, the final irradiation was reached in steps of 0.5 W/cm^2 for prolonged time. In that condition, the rate of the formation of the surface defects being very slow, we retain that the lattice has the possibility for a partial rearrangement. On the contrary, in the present experimental conditions, where a larger power density was delivered at the sample, a high and fast increase of the concentration of surface defects can be reached (at an estimated power density threshold of 40 W/cm^2), leading to nanoparticles' surfaces very reactive which favor the mutual interactions between neighboring particle and the formation of stable polycrystalline aggregates. The experimental findings regarding the phase transition behavior of surface-passivated anatase particles are consistent with the above-mentioned mechanistic scenario. As far as the particle surface is functionalized by chemically bonded nitric groups, the phase transition is strongly inhibited. Only once the nitric groups are removed, irradiation is able to enhance the chemical reactivity of the surface. These results are also consistent with the experimental evidence regarding the behavior of nanometer-sized anatase particles with a thin shell La_2O_3 at the surface[62],[63].In this case, the direct contact between the anatase crystals in neighboring particles is prevented by the La_2O_3 shell[63]. Correspondingly, the anatase-to-rutile phase

transition is significantly hindered or even completely prevented[63]. A further support to the above-mentioned mechanism comes from the irradiation-induced phase transition behavior of carbon-rich anatase in air [64]. In this case, irradiation induces the formation of gaseous carbon monoxide and carbon dioxide molecules, determining the formation of a large number of oxygen vacancies at the particle surface[59]. This enables the occurrence of the anatase-to-rutile phase transition. On the contrary, irradiation is not able to increase the concentration of oxygen vacancies at the surface of carbon-free anatase particles, and the phase transition no longer occurs irrespective of the power used in irradiation experiments[64]. Being these evidences referred to experiments performed in air, the results are in agreement with the novel experimental findings obtained in the present work. The light has a crucial role as a sensitizer of surface agglomerations while the phase transition is connected to structural dynamics and to the role of anatase surface defects and twins. In this scenario the role of surface species or, in general, the defects density on the surface of the nanoparticles plays a key role in the anatase-to-rutile phase transition.

1.3.2 Preserving the crystal structure by core-shell architecture: the case of γ-Fe_2O_3

1.3.2.1 Introduction

Iron oxides are characterized by a wide variety of compounds, which differ by structural and magnetic properties. The continuing interest for this kind of materials is mainly due to the ability to take advantage of their diversity to find new important applications in several research field. Among iron oxides, γ-Fe_2O_3 has attracted a growing attention because its use as catalyst, pigment, gas sensitive material. Its potential applications also concern the realization of high density magnetic storage device and in vivo biological studies [65]-[69]. Moreover, an increasing number of potential applications of core–shell γ-Fe_2O_3 /SiO_2 nanostructures have been reported ranging from drugs delivery, catalyst to gas sensitive devices [70]-[72].

Maghemite (γ-Fe_2O_3) is the second most stable polymorph of iron oxide. Because of its structural similarity with maghemite, magnetite (Fe_3O_4) is frequently used as a precursor; both oxides have cubic in-verse spinel structure, differing in the number of vacancies and in the occupancy of tetrahedral and octahedral cations sites[65]. The degree of disorder of the iron vacancies determines the

crystal structure on maghemite, in particular cation vacancies are localized on octahedral sites and when they are randomly distributed, the space group of γ phase is Fd3m (cubic). This is the typical situation observed for very small nanoparticles. However, it has been found that some kinds of nanosized maghemite obtained from the oxidation of magnetite, with the final average dimensions of 240 nm x 30 nm, present the tetragonal space group $P4_12_12$ [73]. The latter corresponds to an ordered structure and it is also the most stable structure in the bulk and micro materials, as revealed by XRD and neutron scattering experiments and the recent theoretical work of Grau-Crespo *et al* [74].

Due to the structural relationship with γ-Fe_2O_3, γ -FeOOH (lepidocrocite), is also suggested as a possible precursor of maghemite and some other authors demonstrated that a poorly crystallized oxide, known as 2-line ferrihydrite, can be recognized as another precursor of nanostructured maghemite in Fe_2O_3-SiO_2 composites [75],[76].

It is known that nanomaterials can present different structural, electrical, optical and magnetic properties than bulk systems [77]. Due to new thermodynamic features, such as the increasing of surface/volume ratio and the high surface energy contribution, nanosized particles present sometimes unpredictable bhaviours. Maghemite is subjected to a phase transformation to α-Fe_2O_3, the most thermodynamic stable iron oxide. Heat treatments show that the transition can be reached between 500 and 800 K and it depends on synthesis methods and external pressure [78]. Maghemite is highly unstable under light irradiation and this makes its characterization difficult. Experimental techniques that require the use of focused visible light, such as Raman microscopy, can produce conflicting results depending on the intensity and the wavelength of probe radiation [79].

It was reported that the high instability under focused irradiation is due to an elevated optical absorption that can heat the sample up to the critical temperature. To validate this hypothesis Raman spectra recorded at different laser beam intensities were compared to Raman spectra taken on samples treated at different temperature, finding several similarities between them. In particular, it has been asserted that local temperature can be determined from position and bandwidth. Finally, X-ray diffraction analysis has demonstrated that the resulting hematite particles are bigger than the starting maghemite nanoparticles [80].

It has been shown how crystal phase transitions on nanoscaled systems are critically affected by size effects and related surface effects [81]. Moreover, experiments in atmospheres different from air and in high pressure conditions emphasized the role of defects and local lattice deformations in phase transformation processes, e.g. previously reported TiO_2 [82].

To achieve a suitable control of the crystal phase, it is necessary to improve the knowledge of the reasons behind the γ- to α-Fe_2O_3 phase transformation.

In this paragraph we present a comparative study of stability of bare γ-Fe_2O_3 nanoparticles and the same particles coated with a 4 nm thick silica shell, including some novel investigations about the effect of focalized laser irradiation on nanosized samples. We monitor the process of phase transformation as a function of density power (W/cm^2), which can be controlled either by changing laser power or by concentrating the same power on a smaller region using wavelengths corresponding to energies close to or below the energy gap. Furthermore we show how the vacuum conditions in the experimental chamber affect particle stability and how the presence of a silica shell increase the temperature necessary for the transformation. The results highlight the important role of particle surface and grain boundaries.

1.3.2.2 Experimental details

***Synthesis*.** Maghemite nanoparticles were synthesized according to the method reported by De Toro *et al* [83]. Summarizing, iron pentacarbonyl was thermally decomposed and subsequently oxidized with trimethylamine N-oxide at high temperature. A black precipitate was obtained with the addition of acetone after cooling the solution down to room temperature. The precipitate was washed with acetone and methanol, it was used as the starting product to prepare bare and coated nanoparticles. To obtain bare NPs, the particles were dis-persed in n-hexane, precipitated by adding acetone, treated under sonication for one hour and then recovered by precipitation and washed with acetone and n-hexane under sonication.

γ-Fe_2O_3/SiO_2 core/shell particles with a silica shell 4 nm thick were obtained by a general base-catalyzed sol-gel process combined with a microemulsion route (Igepal/Cyclohexane/water)[83]-[85].

Typically, a dispersion of γ-Fe_2O_3 in cyclohexane (3.0 mL, 2.75 mg/mL in cyclohexane) was added to polyoxyethylene (5) nonlylphenylether (5.0 g, Igepal CO-520, Mn = 441, Sigma-Aldrich) dissolved in cyclohexane (60 mL). Ammonium hydroxide (0.7 mL, 25% in water) was added forming a transparent brownish solution of reverse microemulsion. Then, 0.2 mL of TEOS (tetraethyl orthosilicate) was added and the reaction was left to continue for 16 h at room temperature [83].

The bare NPs were found to be single-crystals, 8 nm in diameter with a remarkable small size dispersion (2%). The size distribution of the core/shell particles is similarly narrow. Further details of the particle crystalline structure (using X-ray diffraction) as well as of the magnetic properties of the NPs arranged in a random-close-packed configuration are widely described in Refs [83] and [86].

Structural characterization. Raman scattering measurements were carried out in backscattering geometry using a triple spec-trometer Jobin-Yvon Dilor integrated system and an air liquid cooled Charge-Coupled Device detector. The spectral resolution of the system was < 2 cm^{-1}. All measurements were performed at room temperature and in air atmosphere. Every spectrum was acquired in the Stokes region.

The powder samples were irradiated with visible light beams on the limited range of 0.5 - 3 mW, fo-cused with a 10 X objective with 0.25 NA on a surface area of ~ 2500 μm^2, alternatively the laser spot was focalised with a 50 X objective with 0.75 NA on a surface of ~ 100 μm^2 in order to increase the laser power density on the sample. In the following, if not explicitly specified, data was recorded in the first of these configurations. The samples were irradiated with the line of the 632.8 nm of a He-Ne laser (Spectra-Physics). Powder samples were also exposed to laser irradiation in low vacuum (1 torr).

Additional tests up to 10 mW were carried out with the 488 nm of an argon ion laser (Coherent, In-nova-90 C) and with the 800 nm of a Ti:sapphire (Spectra-Physics). All the reported intensities are referred to laser power on samples. Raman spectra were recorded with an integration time between 100 and 200 s.

To estimate the temperature of the phase transition, bare nanoparticles were heated up to 400 °C, and then cooled to room temperature to verify their crystal phase, while the morphology and

structural evolution of the Fe_2O_3/SiO_2 core/shell systems were observed after heat treatments at 400, 1000 and 1200 °C by Raman technique, XRD diffraction measurements, TEM and HRTEM images. X-ray diffraction patterns were recorded on a Seifert X3000 diffractometer with a θ−θ Bragg−Brentano geometry with Cu Kα wavelength.

Finely ground samples were dispersed in n-octane in an ultrasonic bath. The suspension was then dropped on a copper grid covered with a carbon thin film for the observation. TEM images were obtained by means of a JEM 2010 UHR equipped with a Gatan Imaging Filter (GIF) with a 15 eV window and a 794 slow scan CCD camera.

TEM and XRD analysis where performed on the same portion of the samples treated at increasing temperatures (permanence time at each temperature: 30 minutes; rate:10°C/min).

1.3.2.3. Micro-Raman of Maghemite: role of laser power density

Cubic inverse spinel structure belongs to the space group O_h^7(Fd3m). Group theory predicts the following modes [87]

$$\Gamma = A_{1g} + E_g + 3T_{2g} + T_{1g} + 2A_{2u} + 2E_u + 5T_{1u} + 2T_{2u} \quad (1.8)$$

Bare maghemite powder exhibit four Raman-active modes, namely E_g at 359 cm^{-1}, T_{2g} at 500 cm^{-1} and the unresolved A_{1g} modes at 678 and 710 cm^{-1} (Figure 1.20). Furthermore, the Raman spectrum shows a broad complex structure with maximum at ~1400 cm^{-1} that depends on second order processes [88].

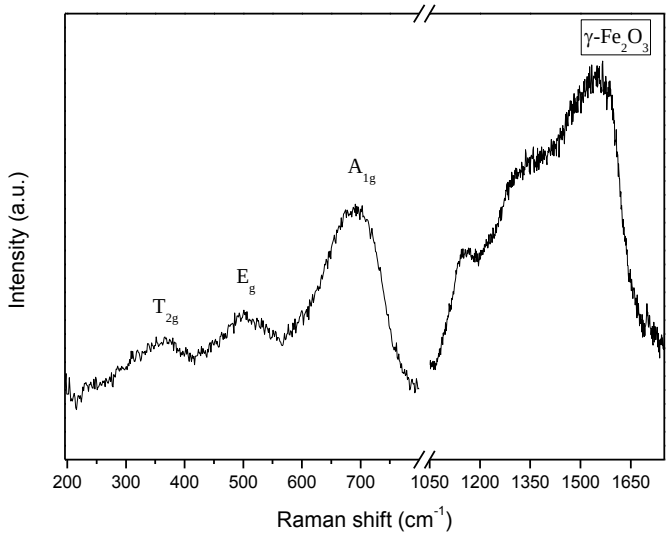

Figure 1.20: Raman spectrum of maghemite nanoparticles.

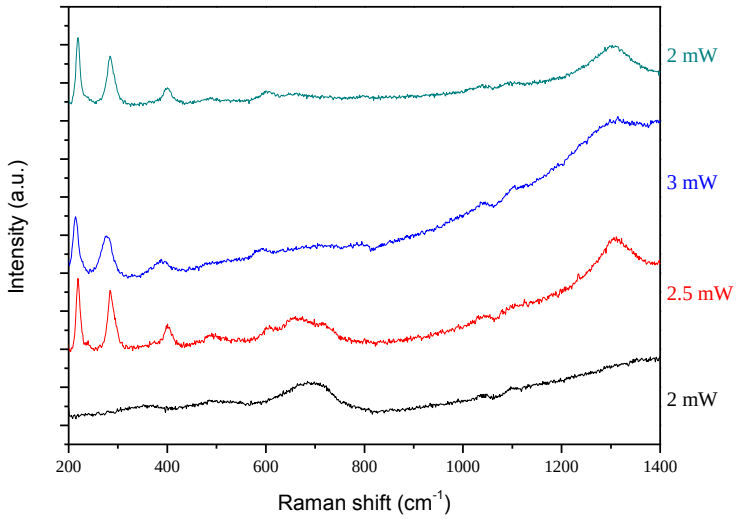

Figure 1.21: Raman spectrum evolution of maghemite as a function of laser intensity (the beam was focalized through OBJ 10X).

Figure 1.21 displays the Raman spectrum of maghemite as a function of laser power. Increasing the intensity of the laser beam up to 2.5 mW produces significant variations, namely the decrease of the A_{1g} mode of maghemite and the simultaneous appearance of new modes at 219, 285, 401, 489, 604, 656 cm^{-1} and at about 1310 cm^{-1}. The new modes are blue shifted and broadened by increasing the laser power up to 3 mW. Additionally, the baseline increases, smearing out the profile of the 1310 cm^{-1} mode. This behavior is correlated to intensity excitation and it appears to be reversible, as will be shown in the next section, even for higher laser power densities. Without changing the focalized point of the sample, reducing the intensity of the excitation beam back to 2 mW lowers the baseline and the modes appear well structured. All the modes listed above can be related to the hematite phase (α-Fe_2O_3). The modes at 219, 495 and 604 cm^{-1} can be attributed to E_g symmetric stretching the of Fe-O bonding, while the modes at 285 (from the contribution of two unresolved modes), 401 and 489 cm^{-1} correspond to A_{1g} symmetric bending of Fe-O bonding in α-Fe_2O_3. Corundum-like structure (D_{3d}^{6}) presents the following vibrational modes:

$$\Gamma = 2A_{1g} + 5E_g + 2A_{1u} + 2A_{2u} + 5E_g + 4E_u + 3A_{2g} \quad (1.9)$$

A_{1u} and A_{2g} are optically silent, while the symmetrical modes (g) are Raman active.

Additional bands (at 656 and at about 1310 cm^{-1}) are not ascribable to space group D_{3d} [6]. Raman spectroscopy studies of single crystal of hematite as a function of pressure correlate the mode at 656 cm^{-1} with the intense band at 1310 cm^{-1}. More precisely, the first is a Raman forbidden longitudinal optical mode (LO) and the latter is its overtone [89], [90] The other interpretation, widespread in the literature, assigns the most intense band to a characteristic two-magnon scattering originated from the interaction of magnons created on antiparallel close spin sites [79],[91] and the 656 cm^{-1} mode to a magnetite-like structure [92] .

γ-Fe_2O_3 nanopowders were irradiated through a 50 X objective (fig. 1.22). As expected, increasing laser power density facilitates the phase transition. Moreover, at 1.5 mW (about 10 times the power density threshold observed for the phase transition from maghemite to hematite) Raman spectrum is covered by a luminescence background. Figure 1.23 shows the photoluminescence excited at 632.8 nm with high laser power density on the sample. Luminescence excited at low energies in the visible range has already been observed in Fe_2O_3 nanoparticles and it can be attributed to an increase of Fe-O bonding and to the enhancement of magnetic coupling between Fe^{3+} ions [93].

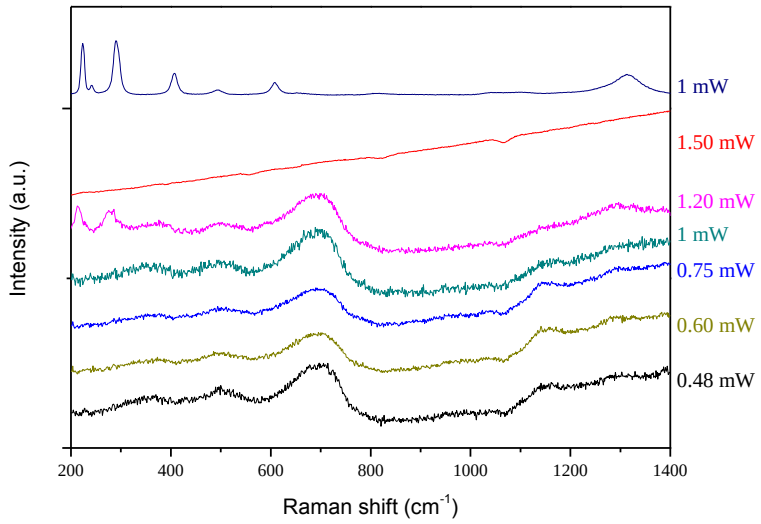

Figure 1.22: Raman spectrum evolution of maghemite as a function of laser power density (the beam was focalized through OBJ 50X).

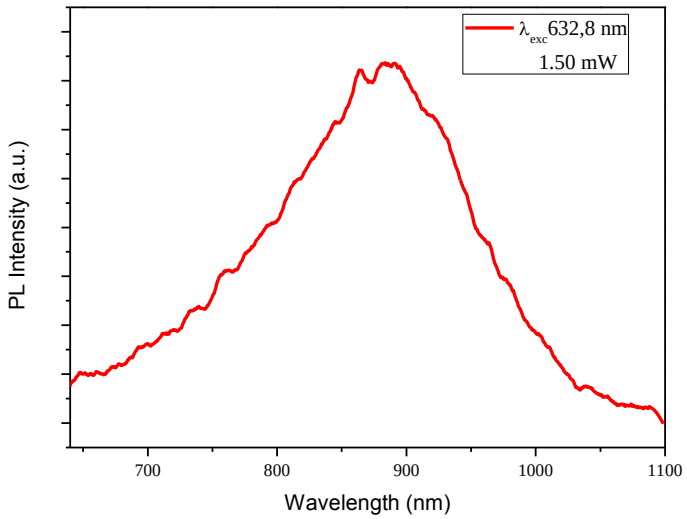

Figure 1.23: Photoluminescence excited at 632.8 nm.

It must be noticed that excitations with energy higher than the semiconductor gap (valuated around 2 eV) [67],[74] induce structural phase transition depending on radiation density power but no change has been revealed with intragap excitations, i.e. with wavelength at 800 nm, even with intensities much higher than those used at 488.0 nm and 632.8 nm (up to 300 mW).

Finally, the role of pressure was investigated in low vacuum conditions with a residual pressure of 1 torr. Raman measurements are shown in Figure 1.24 as a function of the applied laser power. Well below the threshold measured in room conditions, the maghemite vibration modes appear barely identifiable, which probably indicates the presence of an amorphous phase (0.6 mW). As the beam intensity increases to 0.8 mW, the A_{1g} and E_{1g} modes of the hematite phase appear at 226 cm^{-1} and at 293 cm^{-1}, as well as the E_{1g} mode at 410 cm^{-1}. At 1 mW the α phase modes become broader and the baseline increases due to the characteristic luminescence contribution. Finally, spectra acquired with higher intensities, not shown, are characterized by a luminescence background. These measurements testify how laser threshold for crystal phase transformation is drastically reduced in vacuum conditions compared to room conditions (from 2.5 mW down to 0.6-0.8 mW).

γ-Fe_2O_3/SiO_2 core/shell nanoparticles (silica shell: 4 nm) were studied under visible laser irradiation. In stark contrast to the bare maghemite nanoparticles, the cubic phase is preserved even for

the highest density power, applied by means of a highly focalized beam (using a 50X objective) and high intensity light (up to 20 mW).

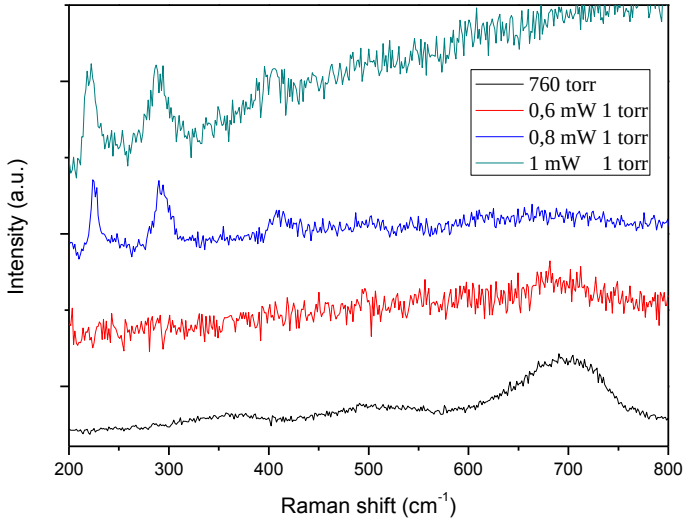

Figure 1.24: Irradiation effect on bare maghemite nanoparticles in vacuum (1 torr).

1.3.2.4 Thermal treatments

The Raman spectra reveals that bare nanoparticles start to transit from γ to α phase after thermal treatment at 400 °C (fig. 1.25). It can be observed the typical hematite overtone mode at 1300 cm^{-1} and the first appearance of the most intense first order E_{1g} modes at 284 cm^{-1} and 397 cm^{-1} demonstrating an uncompleted transition into the most stable phase. This is corroborated by the presence of the maghemite vibrational band at about 700 cm^{-1}, probably convoluted with 600 cm^{-1} hematite mode, that disappears at 450 °C, when the transition is completed. No phase change was revealed in the case of coated nanoparticles at 450 °C while the appearance of the hematite Raman spectrum can be obtained only after thermal treatment at 1200 °C.

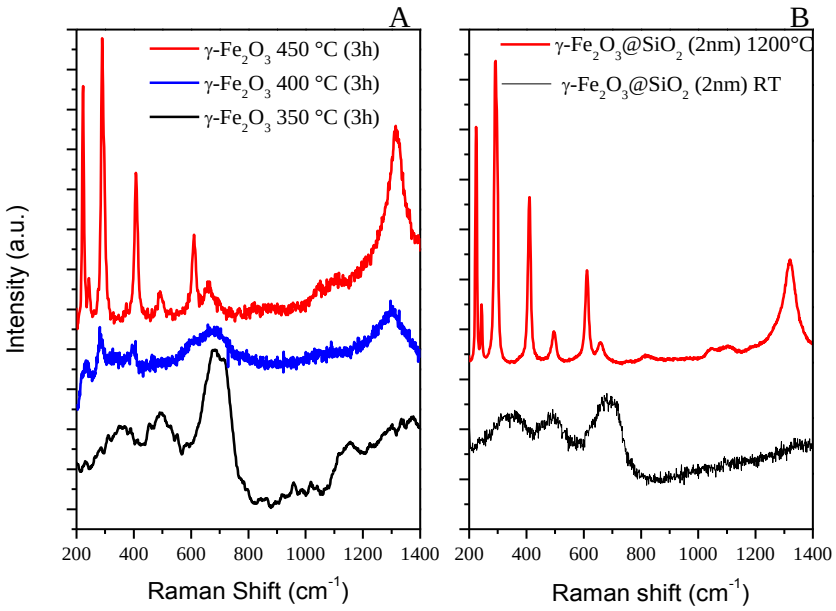

Figure 1.25: Annealing effects on bare maghemite nanoparticles (A) and in γ-Fe₂O₃/SiO₂ core/shell systems (B).

XRD diffraction analysis as well as HRTEM images confirm these results. Figure 1.26 reports the XRD pattern of the as-prepared and thermally treated bare and core-shell (CS4) samples. The as-prepared bare sample shows a sequence of broadened reflections assignable to the nanostructured cubic maghemite phase (PDF-Card 39-1346). By increasing the temperature up to 450°C the sample transforms completely into hematite phase and the crystal size increases, in agreement with Raman measurements. The further treatment at 1000°C induces, as expected, only a significant crystal growth of the hematite phase. The as-prepared core-shell sample shows, besides the broad peaks of the maghemite phase, an additional large band at about 23° ascribable to amorphous silica.

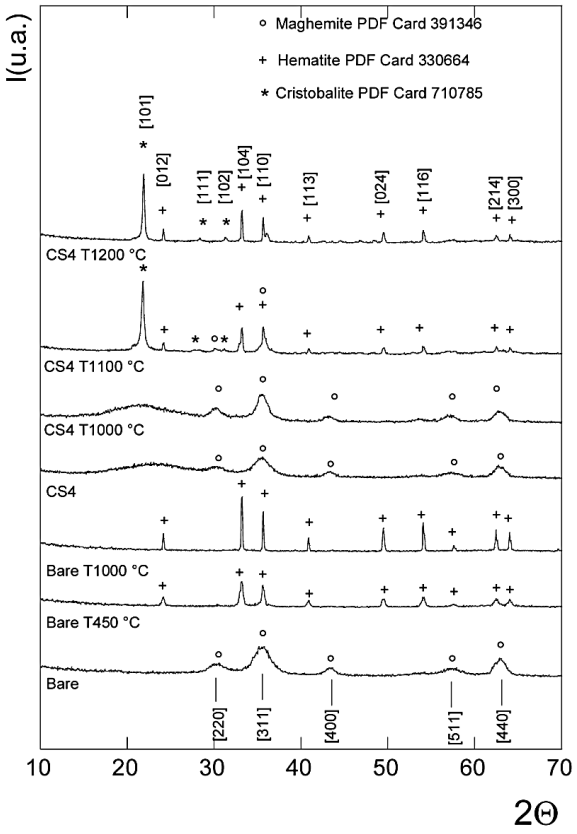

Figure 1.26: XRD patterns of the as-prepared and thermally treated bare and core/shell samples (CS4).

No evident modification is observable up to 900°C (not shown). At 1000°C maghemite phase is still stable, however, some variations in the XRD pattern can be evidenced: the band associated with the amorphous silica undergoes to a shift versus lower angles (about 21°) and the maghemite reflections become slightly narrower. The further increase of the temperature up to 1100°C leads to the silica crystallization into cristobalite phase while maghemite nanoparticles convert almost completely into hematite phase. Finally, at 1200°C the $\gamma-\alpha$ transition is completed.

In order to better understand the temperature effects in the core/shell nanoparticles systems, TEM and HRTEM images were taken before and after each heat treatment; Figure 1.27 reports the images at 1000 and 1200 °C compared to the as-prepared bare and core-shell samples. At 1000 °C amorphous silica undergoes to some modifications because of the partial collapse of the silica shell, anyhow silica continues to kept maghemite nanoparticles well separated from each other and as a consequence the maghemite phase retain its stability (see FFT). However, a careful analysis of the TEM

pictures seems to enlighten some changes in the shape and in the size also in the maghemite nanoparticles. This is probably due to the crystallization of the thin amorphous layer presents at the surface of the as prepared bare nanoparticles.

At higher temperature, the SiO_2 shell totally collapse in a unique matrix and crystallize in cristobalite (see figure 1.27). No isolated nanoparticles with 8 nm in size were detected, confirming their coalescence that induces the formation of big and well-crystallized nanoparticles with a size up to 50 nm. The FFT allow us to confirm the presence of the hematite phase, confirming XRD data.

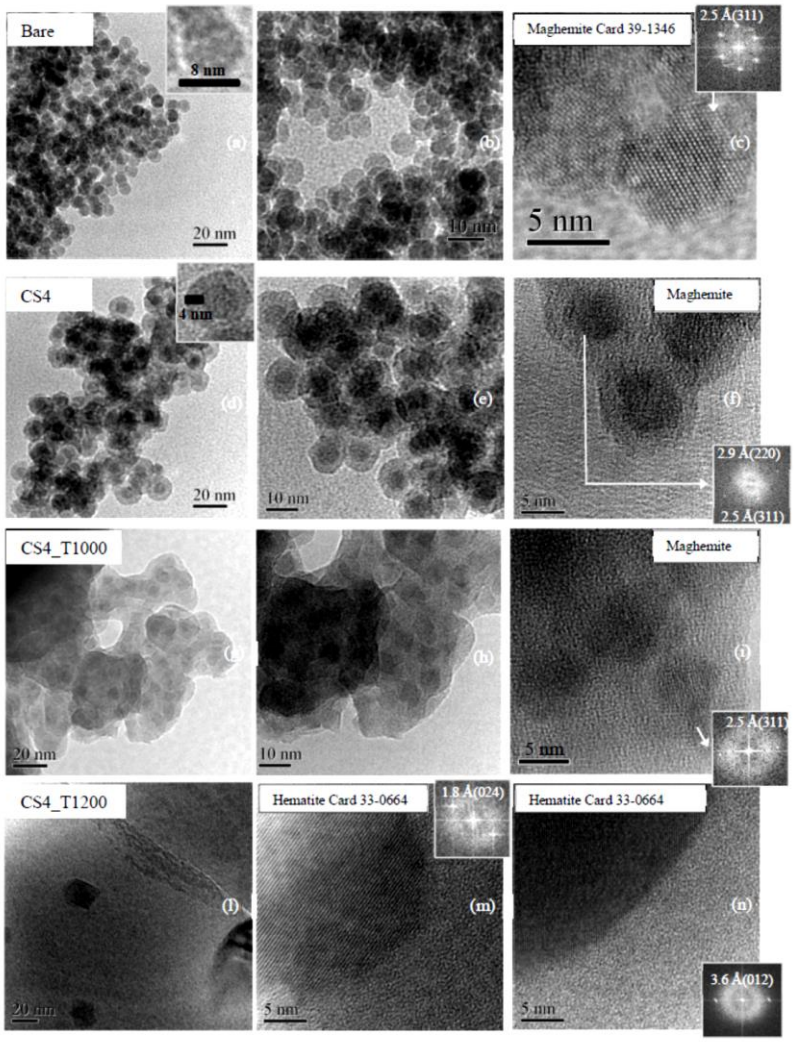

Figure 1.27: TEM and HRTEM images of the as-prepared bare (a,b,c) and CS4 core/shell samples (d,e,f), CS4 treated at 1000° C (g,h,i) and CS4 treated at 1200° C (l,m,n). FFT images have been reported as inset.

1.3.2.5 Discussion

Both hematite and maghemite have a wide absorption over almost the entire visible range and the optical response is principally due to Fe^{3+} ions. Absorption and diffuse reflectance measurements reveal that both hematite and maghemite present two wide bands at about 640 nm and 900 nm [94]. Ligand field theory associates these bands to $^6A_1(^6S) \rightarrow {}^4T_2(^4G)$ and $^6A_1(^6S) \rightarrow {}^4T_1(^4G)$ respectively, in which $^6A_1(^6S)$ corresponds to $(t_{2g}^{\alpha})^3(e_g^{\alpha})^2$ configuration of high-spin Fe^{3+} and $^4T_2(^4G)$, $^4T_1(^4G)$ belong to $(t_{2g}^{\alpha})^2(e_g^{\alpha})^2(t_{2g}^{\beta})^1$ first excited state configuration. Double excitons transitions $^6A_1 + {}^6A_1 \rightarrow {}^4T_1(^4G) + {}^4T_1(^4G)$ are well defined for hematite at 440-550 nm, while blue shifted and less intense at 480-500 nm for maghemite. Strong magnetic coupling Fe^{3+}- Fe^{3+} is responsible for hematite red colour, whereas weak coupling gives a typical dark brown colour to maghemite [94]. In this crystal structure, d-d transitions are indirect and the system mainly relaxes to ground state through non radiative decay, which is rendered more efficient by the frequent presence of traps associated to Fe^{3+} defects in Fe_2O_3 [95].

High excitation densities and non-radiative rates of decay may produce a high local increase of temperature, which can be estimated as follows. The intensity distribution of a laser beam with Gaussian profile is

$$I(\mathrm{r}) = I_0 \exp(-\frac{r^2}{w^2}) \tag{1.10}$$

Assuming that the radiation is absorbed by the first infinitesimal slice of material, the highest possible temperature rise (at the beam centre) is given by [96]

$$\Delta T_{max} = \frac{P}{2\sqrt{\pi} w \kappa} \ , \tag{1.11}$$

where P is the laser power on sample, w the beam waist and κ is the thermal conductivity of the material ($Wm^{-1} K^{-1}$).Since there is not available data for the thermal conductivity of maghemite we use the value reported in literature for hematite thin films[97], namely ≈ 0.37 $Wm^{-1} K^{-1}$. Inserting P = 3 mW, $w \approx 28$ μm (10 X focalization) in the above equations we obtain $\Delta T_{max} \approx 82$ K, a temperature rise clearly insufficient to induce a phase transformation. Moreover, Eq (2) is an overestimate for ΔT_{max}, as it neglects laser penetration depth (a function of λ_{exc}) and radiation losses due to reflection and scattering [98]. Furthermore, treating the samples already in the hematite phase with high density power irradiation

(one order of magnitude higher with respect to the laser power density threshold for the phase transition), a significant shift of the A_{1g} and $2E_g$ Raman modes is revealed (Figure 1.28). It is possible to correlate the Raman shift with the effective temperature of the samples; according to previous work, 10 the estimated temperature is lower than 400 °C for the maximum laser power density (i.e. about 1 order of magnitude greater than the threshold value for the phase transition). Even under this unfavourable conditions, the results of the above approximation allow to conclude that the phase transition from maghemite to hematite is not thermally driven.

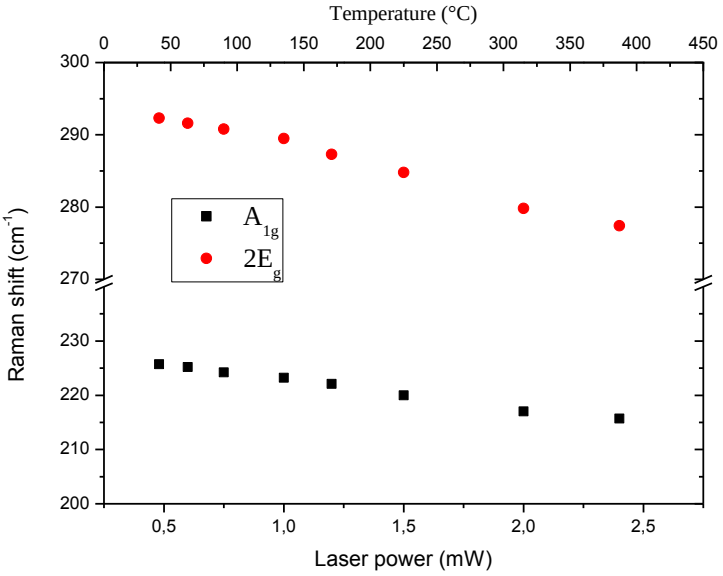

Figure 1.28: Wavenumbers maximum position of the A_{1g} and $2E_g$ lines of hematite as function of the laser power on the samples (focalized in 100μm^2)

The comparison of the results obtained for maghemite nanoparticles with and without a thin silica shell corroborate that the coalescence process is at the basis of the structural transition. Different works on iron oxides stability have offered experimental evidence for particle coalescence. In situ time resolved XRD measurements has been used to monitored the evolution of particle size, which shows an abrupt doubling of α-Fe_2O_3 particle size attributed to a germination-growth process [78].

It is also known that organic coatings (for example oleic acid) improve the stability of the maghemite phase under laser irradiation[99]. Furthermore, it has been shown that phase stability is highly dependent on the amount of oleic acid and probably on bonding typology, pointing out that bridging and bidentate linkages enhance particle stability. The transition is always accompanied by

coating degradation, suggesting the necessity of direct particles contact. Even with a silica shell as thin as 4 nm, maghemite nanoparticles show a great stability enhancement, preserving its γ phase over a wide range of laser power (as concluded by the absence of any changes in the Raman spectra). These nanoparticles are stable up to almost 1000 °C, with a full transition to the α phase at 1200 °C after the collapse of the silica shells.

In bulk materials, phase transitions are customarily studied in terms of temperature and pressure. At the nanoscale other factors need to be considered, as the system size and shape as well as possible surface/interface details. As the particle size is reduced, the surface properties become most important, as reflected by the drastic reduction (some hundreds of degrees) of the transition temperature [100].

Calculations in iron oxides of formation free energy and surface enthalpy show thermodynamic crossovers of the stability as a function of surface area and nature of ligands. The case of γ-Fe_2O_3 and α-Fe_2O_3 is exemplary: maghemite particles with anhydrous surface become stable (relative to hematite and water) at a specific surface area of about 75 $m^2 g^{-1}$, whereas surface-hydrated particles are stable beyond about 440 $m^2 g^{-1}$ [101].

A single nanoparticle can be thought as formed by two regions, a core with bulk material features and a surface characterized by unsaturated bonds, bonding angles and lengths much different from those of the core, and foreign chemical species. Particles with high surface enthalpy tend to reduce their high energy sites absorbing water and the resulting decrease of energy contributes to the mentioned variation in the thermodynamic crossover [101].

Optical and electrical properties of nanostructured semiconductors are often affected by the presence of intragap energy levels due to cationic or anionic surface vacancies [102],[103]. It is well known that the surface of metal oxide particles is highly defective. In particular, in iron oxides these defects are mainly oxygen vacancies and Fe^{2+} ions. The defective surfaces react with water and become partially covered with molecular H_2O and/or its dissociated species OH [104],[105]. The presence of water and hydroxyl species on surfaces surrounding the nanometer sized core has a significant influence on the mechanisms and kinetics of surface chemical reactions. In the case of high surface density and

direct contact between nanoparticles, the appearance of a network connecting the crystallites may be favoured by OH groups and water forming Fe-OH-Fe and Fe-O-Fe bridges between the hydrated shells [106],[107]. We argue that this hydrous iron oxides formed between the nanoparticles can be approximated with a rough formula xFe_2O_3,yH_2O, e. g. $5Fe_2O_3,9H_2O$ [108] or $Fe_5O_7(OH),4H_2O$ or $Fe_4O_5(OH)_2\ 3H_2O$ [109],[110] or simply $Fe(OH)_3$, depending on the O/OH ratio [111]. These contact points or necks between nanoparticles act as the germination nuclei for the hematite phase upon heating or illumination. In fact hematite is formed at the surface through the dehydration and internal rearrangement at the surfaces i.e. [111],[112]:

$$xFe_2O_3, yH_2O \rightarrow x(\alpha)Fe_2O_3 + yH_2O \quad (1.12)$$

and/or [113]

$$Fe(OH)_3 \rightarrow FeO(OH) \rightarrow \alpha\text{-}Fe_2O_3 \text{ (transformation)} \quad (1.13)$$

and then grows towards the nanoparticle core . If the heating effect is obvious on the dehydratation process, the illumination effect needs more discussion. Beyond a minor effective thermal contribution, the optical induced transformation is determined by the particle size and surface, which can promote or inhibit the coalescence process. This event is not rare in metal oxide semiconductors or metals. Banfield *et al*. [114] confirmed the mechanism of coalescence in anatase to rutile transformation by means of nucleation at anatase twin boundaries formed by oriented attachment. The parallelism between anatase/ γ-Fe_2O_3 (as metastable phase) and rutile/ α-Fe_2O_3 (stable phase) suggests a transition controlled by processes of the same kind. It has been discussed how surface defects and atmosphere may drastically influence the stability of a crystal phase under laser irradiation [82],[115]. Intragap laser irradiation experiments performed in reducing atmospheres point out that the phase transition can be promoted by the chemical bonds between highly reactive surfaces of neighbouring particles with the pristine crystalline structure. In our case, the reactivity of the surfaces is highly increased upon illumination. In fact, excitations higher than the bandgap of the iron oxide generate electrons in the conduction band and holes at the valence band mainly in the surface states of the nanoparticles [116]. According to references [117] and [118] the dehydration process upon illumination can be summarized as

$$H_2O_{ads} + h^+ \rightarrow OH^* + H^+ \quad (1.15)$$

$$4OH^* \rightarrow 2H_2O_2 \rightarrow 2H_2O + O_2 \quad (1.16)$$

where irradiation in low vacuum conditions increases the desorption of ligands at the surface providing a more reactive transformation process, leading a lower threshold light power density. On the contrary, highly stable coating, such as SiO_2 , prevents contact between nanoparticles and stabilize the surfaces even at extreme conditions of temperature. In this case the phase transformation from maghemite to hematite starts only after a complete collapse of the SiO_2 shell and the formation of Fe_2O_3 aggregates, which then originate the hematite phase observed in the structural characterization measurements.

The high temperature conditions favor the structural rearranging at the surfaces and the chemical bonding between nanoparticles [80].The formation of stable aggregates and the growth of the hematite phase is revealed by the coherent diffraction domains in the HRTEM measurements with average dimension much greater with respect to the starting maghemite core. These results underline the need of direct interparticle contact for the phase transition process to start.

1.4 Summary of Chapter 1

In this chapter, we investigated the phase transformation process between stable phases of metal oxides nanoparticles, pointing out the activation of such transformation by low intensity and intrinsic optical excitation, which promotes processes of chemical species desorption at the surfaces.

If the defects are not passivated, the chemical interaction between neighboring nanoparticles is possible, determining the formation of stable chemical bonds. Such regions are likely to represent the preferential sites for the nucleation of the new stable phase. Once nucleated, it undergoes a fast growth by coalescence, absorbing the neighboring domains into a larger coherent crystalline domain.

The realization of an inert and stable shell drastically increases the stability of nanoparticles (as in the case of maghemite), resulting in an inhibition of the phase transformation by light irradiation. The transformation is only observed by heat treatment at very high temperature (1100°C), almost 700 °C higher than that for γ-Fe_2O_3 bare nanoparticles. Moreover, we observed that the transformation is al-

ways accompanied by the shells collapse and the aggregation of Fe_2O_3 nanoparticles diffused inside the silica matrix.

The experimental findings reported in this section proved the high dependence of crystal stability on the surface states at nanoscale. The capability to control the surface and in particular the concentration of defects can significantly preserve the physical properties of oxides and in case the crystal phase for synthesis processes at high temperature.

1.5 References

[1] K. Tennakone, G. R. R. A. Kumara, I. R. M. Kottegoda, V. P. S. Perera, and P. S. R. S. Weerasundara, J. Photochem. Photobiol. A 117, 137 (1998).
[2] H. Long, A. Chen, G. Yang, Y. Li, and P. Lu, Thin Solid Films 517, 5601 (2009).
[3] N. Golego, S. A. Studenikin, and M. Cocivera, J. Electrochem. Soc. 147, 1592 (2000).
[4] K. Page, R. G. Palgrave, I. P. Parkin, M. Wilson, S. L. P. Savin, and A. V. Chadwick, J. Mater. Chem. 17, 95 (2007).
[5] Q. Li, S. Mahendra, D. Y. Lyon, L. Brunet, M. V. Liga, D. Li, and P. J. J. Alvarez, Water Res. 42, 4591 (2008).
[6] M. Wagemaker, W. J. H. Borghols, and F. M. J. Mulder, J. Phys. Chem. 129, 4323 (2007).
[7] D. Deng, M. G. Kim, L. Y. Lee, and J. Cho, Energy Environ. Sci. 2, 818 (2009).
[8] O. Carp, C. L. Huisman, and A. Reller, Prog. Solid State Chem. 32, 33 (2004).
[9] Y. Zhang, Z.-R. Tang, X. Fu, and Y.-J. Xu, ACS Nano 12, 7303 (2010).
[10] M.-Q. Zhang and Y.-J. Xu, Phys. Chem. Chem. Phys. 15, 19102 (2013).
[11] M. Ni, M. K. H. Leung, D. Y. C. Leung, and K. Sumathy, Renew. Sust. Energy Rev. 11, 401 (2007).
[12] M. Dürr, A. Schmid, M. Obermaier, S. Rosselli, A. Yasuda, and G. Nelles, Nature Mater. 4, 607 (2008).
[13] M. Bledowski, L. Wang, A. Ramakrishnan, O. V. Khavryuchenko, V. D. Khavryuchenko, P. C. Ricci, J. Strunk, T Cremer, C. Kolbeck, and R. Beranek, Phys. Chem. Chem. Phys. 13, 21511 (2011).
[14] T. Ohno; K. Tokieda; S. Higashida; M. Matsumura, Appl. Catal., 244, 383−391 (2003).
[15] M. Salis, P. C. Ricci, and A. Anedda, Raman Spectrosc. 40, 64 (2009).
[16] X. Wang, Z. Feng, J. Shi, G. Jia, S. Shen, J. Zhouab, C. Li, Phys. Chem. Chem. Phys., 12, 7083 (2010).
[17] P. C. Ricci, C. M. Carbonaro, L. Stagi, M. Salis, A. Casu, S.Enzo, and F. Delogu, J. Phys. Chem. C 117, 7850 (2013).
[18] N.-L. Wu, M.-S. Lee, Z.-J. Pon, and J.-Z. Hsu, J. Photochem. Photobiol. A, Chem. 163, 277 (2004).
[19] K. Suriye, R. Lobo-Lapidus, G. Yeagle, P. Praserthdam, R. D. Britt, and B. C. Gates, Chemistry 14(5), 1402–1414
[20] S. J. Huang, A. B. Walters, and M. A. Vannice, J. Catal. 192, 29 (2000).
[21] M. A. Kamboures, J. D. Raff, Y. Miller, L. F. Phillips, B. J. Finlayson-Pitts, R. B. Gerber Phys. Chem. Chem. Phys., 10, 6019 (2008).
[22] M. A. Kamboures, W. van der Veer, R. B. Gerberac, L. F. Phillips, Phys. Chem. Chem. Phys, 10, 4748 (2008).
[23] J. A. Rodriguez, T. Jirsak, G. Liu, J. Hrbek, J. Dvorak, and A. Maiti, J. Am. Chem. Soc. 123, 9597 (2001).
[24] W. Huang, P. Raghunath, and M. C. Lin, J. Comput. Chem. A 30, 321065 (2011).
[25] R. da Silva, L. G. C. Rego, J. A. Freire, J. Rodriguez, D. Laria, V. S. Batista, J. Phys. Chem. C 114, 19433 (2010).
[26] Y. Hyunjun, K. Myungjun, B. Changdeuck, L. Seonhee, K.Hyunchul, A. Tae Kyu, and S. Hyunjung, J. Phys. Chem. C 118, 9726 (2014).
[27] F. J. Knorr, C. C. Mercado, and J. L. McHale, J. Phys. Chem. C 112, 12786 (2008).
[28] J. Buha, Thin Solid Films 545, 234 (2013).
[29] X. Pan, M.-Q. Yang, X. Fu, N. Zhang, and Y.-J. Xu, Nanoscale 5, 3601 (2013).
[30] P. Madhu Kumar, S. Badrinarayanan, and M. Sastry, Thin Solid Films 358, 122 (2000).
[31] P.C. Ricci; A. Casu; M. Salis; R. Corpino; A. Anedda,J. Phys. Chem. C, 114, 14441 (2010).
[32] T. Ohno; K. Tokieda; S. Higashida; M. Matsumura Appl. Catal., 244, 383−391 (2003).
[33] E. Kraleva; M. L. Saladino; R. Matassa; E. Caponetti; S. Enzo;J. Struct. Chem., 52, 330−339 (2001).
[34] J.A. Wang; R. Limas-Ballesteros;T. Lopez; A. Moreno; R. Gomez; O. Novaro; X. Bokhimi, J. Phys. Chem. B, 105, 9692−9698 (2001).
[35] S. Ardizzone; C.L. Bianchi; G. Cappelletti; S. Gialanella; C. Pirola; V. Ragaini, J. Phys. Chem. C, 111, 13222−13231 (2007).
[36] H. Zhang; J.F. Banfield, J. Mater. Chem., 8, 2073−2076 (1998).
[37] H. Zhang, H.; J.F.Banfield, J. Phys. Chem. B, 104, 3481−3487 (2000).
[38] Y. Hwu; Y.D.Yao; N.F. Cheng; C.Y. Tung; H.M. Lin, Nanostruct. Mater. 9, 355−358 (1997).
[39] D.A.H. Hanaor; C.C. Sorrell, J. Mater. Sci., 46, 855−874 (2001).
[40] A.S. Barnard; L.A. Curtiss,Nano Lett., 5, 1261−1266 (2005).
[41] L. Lutterotti; R. Ceccato; R. Dal Maschio; E. Pagani, Mater. Sci. Forum , 278−281, 87−90 (1998).
[42] H.Y. Lee; W.L. Lan; T.Y. Tseng; D. Hsu; Y.M. Chang; J.G. Lin, Nanotechnology, 20, 315702 (2009).
[43] A.L.A. Parussulo; M.F.G. Huila; K. Araki; H.E. Toma, Langmuir, 27, 9094−9099 (2011).
[44] P.P. Lottici; D. Bersani; M. Braghini; A. Montenero, Raman J. Mater. Sci., 28, 177−183 (1993).
[45] K.J. Klabunde; J. Stark; O. Koper; C. Mohs; D.G. Park; S. Decker; Y. Jiang; I. Lagadic; D. Zhang, J. Phys. Chem., 100, 12142−12153 (1996).
[46] K. Komaguchi; T. Maruoka; H. Nakano; I. Imae; Y. Ooyama, J. Phys. Chem C., 114, 1240−1245 (2010).
[47] S. Q.Zhou; E. Cizmar; M.K. Potzger; M. Krause; G. Talut; M. Helm; J. Fassbender; S.A. Zvyagin; J.S. Wosnitza; H. Schmidt, Phys.Rev. B , 79, 113201−113205 (2009).
[48] J. Guillot;f. Fabreguette; L. Imhoff; O. Heintz; M.C. Marco de Lucas; M. Sacilotti; B. Domenichini; S. Bourgeois, Appl. Surf.Sci., 177, 268−271 (2001).
[49] R. Beranek; H. Kisch, Photochem.Photobiol., 7, 40−48 (2007).
[50] L.-B.Xiong; J.-L Li; B. Yang; Y.J. Yu, Nanomater., 831524−831537 (2012).
[51] A. Fujishima; T. N. Rao; D.A. Tryk, J. Photochem. Photobiol., C, 1, 1−21 (2000).
[52] M. Salis, M.; P.C. Ricci; A. Anedda, J.Non-Equilib. Thermodyn. 3(2) 27-33 (2012)
[53] R. Nakamura; Y.J. Nakato, Am.Chem. Soc., 126, 1290−1298 (2004).
[54] G. Mattioli; F. Filippone; A.A.Bonapasta, J. Am. Chem. Soc. 128, 13772−13780 (2006).
[55] M. Ulmann; N.R. De Tacconi; J. Augustynski, J. Phys. Chem., 90, 6523−6530 (1986).

[56] M.-H.Tsai; P. Shen; S.-Y.Chen,J. Appl. Phys., 100, 114313−114319 (2006).
[57] Y. Zhou; K.A. Fichthorn, J. Phys. Chem. C, 116,8314 (2012).
[58] R.L. Penn; J.F. Banfield, J. F. Am. Mineral., 84, 871(1999).
[59] J. Zhang; Q. Xu; M. Li; Z. Feng; C. Li , J. Phys. Chem. C , 113,1698 (2009).
[60] C. Rath; P. Mohanty; A.C. Pandey; N.C. Mishra, J. Phys. D: Appl. Phys., 42, 205101−205107 (2009).
[61] X. Li; X. Quan; C. Kutal, Scr. Mater. 2004, 50, 499−505 (2004).
[62] P.I. Gouma; P.K. Dutta; M. Mills, J. Nanostruct. Mater. 1999,11, 1231−1237 (1999).
[63] J. Zhang; M. Li; Z. Feng; J. Chen; C. Li,J. Phys. Chem. B, 110, 927−935 (2006).
[64] A. Chatterjee; S.-B. Wu; P.-W.Chou; M.S.Wong; C.-L. Cheng,J. Raman Spectrosc., 42, 1075 (2011).
[65] Cornell M.; Schwertmann U. The Iron Oxides: Structure, Properties, Reactions, Occurrences and Uses. VCH: Weinheim, Germany, (2003).
[66] E. Rezlescu; C. Doroftei; N. Rezlescu; P.D. Popa, Phys. Stat. Sol. A, 8, 1790–1793 (2008).
[67] J.K. Vassiliou; V. Mehrotra; M.W. Russell; E.P. Giannelis; R.D.McMichael;R.D. Shull; R.F. Ziolo, J. Appl. Phys., 73, 5109-5116 (1993).
[68] P. Gould, Nano Today, 1, 34-39 (2006).
[69] TK T. Nguyen CRC press: Boca Raton, USA, (2012).
[70] V. Maurice; T. Georgelin; J.M. Siaugue; V. Cabuil, J. Magn. Magn. Mater. 321, 1408-1413 (2009).
[71] N. Panda; H. Sahoo; S. Mohapatra, J. of Hazar. Mater. 185, 359-365 (2011).
[72] J. Zhang; A. Thurber; C. Hanna; A. Punnoose, Langmuir , 26, 5273-5278 (2010).
[73] Z. Somogyvari; E. Svab; G. Meszaros; K. Krezhov; I. Nedkov; I. Sajo, I.; V. Bouree. Appl. Phys. A: Mater. Sci. Process., 74 , S1077-S1079 (2002).
[74] R. Grau-Crespo; A.Y. Al-Baitai; I. Saadoune; N.H. De Leeuw J. Phys. Condens. Matter, 22 , 255401 (2010)
[75] C.Cannas; G.Concas; A.Falqui; A.Musinu; G.Spano; G. Piccaluga, J. of Non-Cryst. Solids. 286, 64 (2001).
[76] C.Cannas; A.Musinu;G.Navarra; G.Piccaluga Phys. Chem. Chem.Phys.,6, 3530 (2004).
[77] C.N.R.Rao; J.P.Thomas; G.U.Kulkarni Nanocrystals. Synthesis, properties and applications. Springer Berlin Heidelberg: Berlin, Germany (2007).
[78] T.Belin,N. Millot; N.Bovet; M. Gailhanou; J. Solid State Chem. 180, 2377 (2007).
[79] D. L. A. De Faria; S.Venaüncio Silva; M.T. de Oliveira J.Raman Spectrosc. 28, 873 (1997) .
[80] Y. El Mendili; J.Bardeau; N.Randrianantoandro; F.Grasset; J.Greneche, J. Phys. Chem. C 116, 23785 (2012).
[81] Z.Zhong; Y. Zhao; Y.Koltypin; A.Gedanken J. Mater. Chem., 8, 2167 (1998).
[82] P.C.Ricci;C.M.Carbonaro; L. Stagi; M. Salis; A. Casu; S.Enzo; F. Delogu, J. Phys. Chem. C, 117, 7850 (2013).
[83] J. A.,De Toro; P.S. Normile;S.S Lee; D. Salazar; J.L.Cheong; P.Muñiz; J..M Riveiro, M. Hillenkamp,M.; F.Tournus; A.Tamion, et al.. J. Phys. Chem. C, 117, 10213 (2013).
[84] C.Cannas, A.Musinu; A. Ardu; F.Orru, D.Peddis, M.Casu, R.Sanna, F.Angius,G. Diaz, G. Piccaluga Chem. Mater., 22, 3353(2010).
[85] M.A. Scorciapino; R. Sanna.;A. Ardu; F. Orrù ; M.Casu ;A. Musinu; C.Cannas, J. Coll. Int. Sci., 407, 67-73 (2013).
[86] J.A. De Toro.; S.S. Lee ;D. Salazar; J.L.Cheong; P.S. Normile; P.Muñiz; J.M.; Riveiro; M.Hillenkamp; F.Tournus;A. Tamion et al. Appl. Phys. Lett. 102, 183104 (2013).
[87] L.V. Gasparov;D.B. Tanner; D.B. Romero; H.Berger;G. Margaritondo;L. Forro´, Phys. Rev. B, 62, 7937(2000).
[88] P.Colomban; S.Cherifi ;G. Despert, J. Raman Spectrosc., 39, 881 (2008).
[89] M.J. Massey ; U. Baier; R. Merlin ; W.H. Weber. Phys. Rev. B, 41, 7822 (1990).
[90] I.V.Chernyshova; M.F.Hochella Jr; A.S.Madden, Phys. Chem. Chem. Phys. 9, 1736–1750 (2007).
[91] T.P. Martin; R.Merlin; D.R.Huffman;M. Cardona Solid State Commun., 22, 565-567 (1977).
[92] I.Chamritski;G. Burns, J. Phys. Chem. B, 109, 4965-4968 (2005).
[93] Y.Zhang;W. Liu;C. Wu; T. Gong;J. Wei;M. Ma; K.Wang, K.; M. Zhong; D. Wu. Mater. Res. Bull. , 43, 3490 (2008).
[94] D.M. Sherman ; T. David, Am. Mineral., 70, 1262 (1985)
[95] J.N. Cherepy; D.B. Liston; J.A. Lovejoy; H. Deng; J.Z. Zhang, J. Phys. Chem. B , 102, 770 (1998).
[96] M. Lax, J. Appl. Phys. , 48, (1977).
[97] S.S. Shinde; R.A. Bansode; C.H. Bhosale; K.Y. Rajpure J. Semicond., 32, 013001(2007).
[98] E. Liarokapis; E. Anastassakis, Phys. Rev. B, 30, 2270 (1984).
[99] M.A.G.Soler; G.B.Alcantara; F.Q.Soares; W.R. Viali;P.P.C Sartoratto, J.R.L. Fernandez, S.W.da Silva ; V.K.Garg; A.C. Oliveira;P.C. Morais Surf. Sci., 601, 3921 (2007).
[100] N. Satoh; T. Nakashima;K.Yamamoto, Sci. Rep., 3, 1-7 (2013).
[101] A. Navrotsky; L. Mazeina; J. Majzlan, Science ,319, 1635(2008).
[102] K. Iijima; M.Goto; S. Enomoto; H. Kunugita; K. Ema; M. Tsukamoto; N. Ichikawa; H. Sakama J. Luminesc., 128, 911 (2008).
[103] P. Kofstad; Nonstoichiometry, Diffusion and Electrical Conductivity of Binary Metal Oxides, Wiley Interscience: New York , (1972).
[104] P.A. Thiel; T.E. Madey, Surf. Sci. Rep. 7, 211 (1987).
[105] M.A.Henderson Surf. Sci. Rep., 46, 1 (2002).
[106] M. Nastasi;D. Parkin;H. Gleiter, Mechanical Properties and Deformation Behaviour of Materials Having Ultra-Fine Microstructures Springer:Berlin, Germany, (1993).
[107] S.Yamamoto; T. Kendelewicz; J.T.Newberg; G.Ketteler;D.E. Starr; E.R. Mysak; K.J. Andersson; H.Ogasawara; Bluhm; M.Salmeron; G.E.Brown Jr. et al. J. Phys. Chem. C 5, 2256 (2010).
[108] M. Loan; G.M. Parkinson; W.R. Richmond Am. Mineral.90, 258 (2005).
[109] S.Bakardjieva; V. Stengl;J. Subrt;E. Vecernikova Solid State Sci., 7, 367 (2005).
[110] U. Schwertmann; J. Friedl; H. Stanjek J. Colloid Interface Sci., 209, 215 (1999).

[111] U.Schwertmann; H. Stanjek ; H.H. Becher, Clay Miner., 39, 433 (2004).
[112] Y. Cudennec;A. Lecerf, J.Solid State Chem.179, 716 (2006).
[113] Y.Q.Liang; Z.D. Cui; S.L. Zhu; X.J. Yang; Electrochim. Acta , 55, 5245 (2010).
[114] H. Zhang; J.F. Banfield, J. Phys. Chem. B, 104, 3481 (2000).
[115] P.C. Ricci,; A. Casu; M. Salis, M.; R. Corpino.; A. Anedda. J. Phys. Chem. C, 114, 14441 (2010).
[116] D. Zhang; Y. Zhang; Y. Gao; Y. Han; C. Gao; Y. Ma; C. Cheng, K. Yu J. Appl. Phys., 111, 063718 (2012).
[117] S. Kakuta; A. Toshiyuki. J.Mater. Sci., 44, 2890 (2009).
[118] M.A. Gondal ; A. Hameed;, Z.H. Yamani; A.Suwaiyan A. Appl. Catal A, 268,159 (2004).

Chapter 2

Carbon Nitride Compounds

2.1 Graphitic Carbon Nitride

2.1.1 Introduction

Only in recent years, the materials based on C_3N_4 have acquired a growing interest. Progressively, C_3N_4 was employed in chemical and physical applications, especially in the processes of CO_2 capture or control of pollutants. Moreover, carbon nitride systems were proposed in water splitting and energy storage devices [1].

Since the work done by Liu and Cohen [2], the graphitic carbon nitride g-C_3N_4 has been recognized as an ultra-hard material. From that, researchers investigated the stability of carbon nitride compounds, underlining outstanding chemical and thermal stability [3].

g-C_3N_4 results insoluble in water, ethanol, toluene, diethyl ether and THF [3] and non-volatile up to 600 °C, completely decomposing only at 700 °C [4].

Several synthesis methods were employed in g-C_3N_4 production like PVD, CVD, solvothermal method, solid-state reaction and thermal nitridation [11]. In general, the synthesis requires nitrogen rich sources like dicyandiamide, urea, melamine. Among these, melamine (s-triazine based compound) undergoes a condensation with ammonia losses under thermal treatment [19]. Jürgens *et al.* [5] postulated the mechanism of melamine condensation. At a temperature slightly higher than 300 °C the further condensation with ammonia liberation provides the so-called Melem structure or the 2,5,8-Triamino-tri-s-triazine (heptazine) (fig 2.1b). Finally, the subsequent linking mechanism of heptazine units determines the Melon (fig. 2.1c).

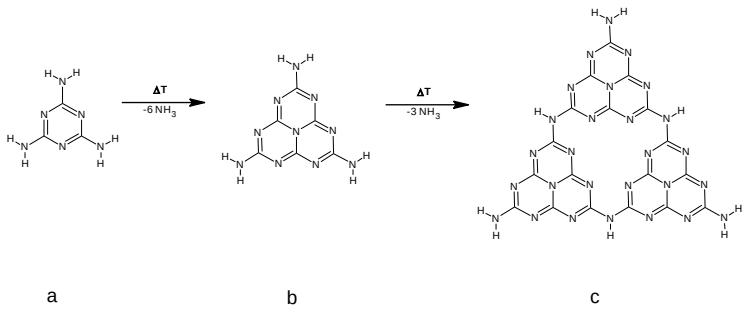

Figure 2.1: Proposed scheme of the melamine condensation.

2.1.2 The Structure of graphitic Carbon Nitride

Synthesis. A certain amount of melamine powders (Aldrich, 99 %) was put in an alumina crucible, placed in a quartz tube accommodated in tubular furnace and treated at the temperatures of 300°C (Me300), 400 °C (Me400) , 500 °C (PCN500) and 600 °C (PCN600), for 2h at the rate of 5°C/min under nitrogen flux (30 ml/min).

Despite the universally recognized mechanism of thermally synthesized g-C_3N_4, its structure is still debated. Resolving the structure represents a prominent problem for the correct prediction of physical and chemical properties.

Some of the intermediate products can be accurately studied by XRD patterns. They present well-defined diffraction peaks and this is the case for melamine condensation at the temperature near 300 °C and for the single-phase melem. XRD pattern of graphitic structure presents only two main peaks at $2\theta = 13.2$ ° and $2\theta = 27.3$ °. The mentioned reflexes are attributed to the periodic structural feature of the single sheets and to the graphite-like stacking, respectively [6].

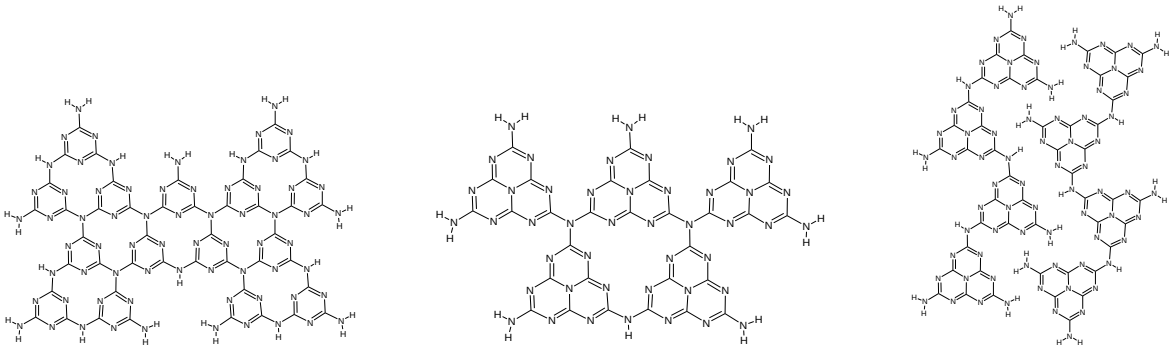

a **b** **c**

Figure 2.2: Proposed structures for the g-C_3N_4: a) structure based on triazine units; b) structure based on heptazine units; c) Liebig's melon.

Figure 2.3 reports the XRD patterns of the heat treated melamine at the temperature of 300, 400, 500 and 600 °C, acquired in the Bragg angles range $10° \leq 2\theta \leq 40°$. The sample annealed at 300 °C shows a sequence of reflections assignable to the crystalline phase melamine [7].

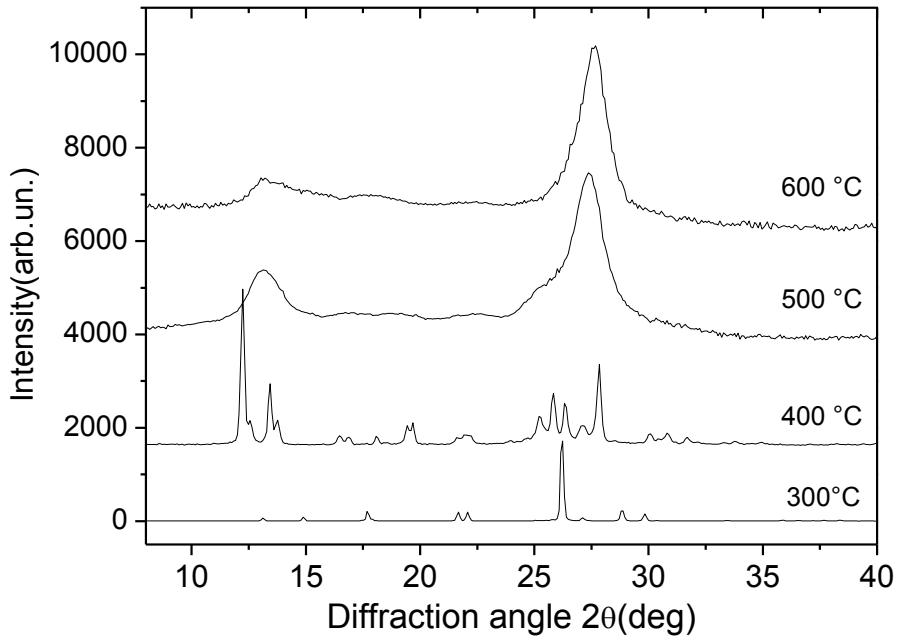

Figure 2.3: XRD pattern of heat-treated melamine at various temperature.

Melamine crystal has monoclinic structure with $P2_1/c$ (no.14) space group [8] and lattice parameter a = 7.27 Å, b = 7.48 Å, c = 10.57 Å, $\alpha = \beta = 90$ ° and $\gamma = 112.3$ °.

At 400 °C we observe a significant change in diffraction pattern. Based on the work of Jürgens *et al.* [5] we are able to attribute all the main peaks to the presence of a melem phase. Solid melem presents monoclinic unit cell, belonging to space group $P2_1/c$ (no.14), as well as melamine. During the thermal process, melamine releases $–NH_3$ determining the new heptazine structure. It follows that the structure at 400 °C is mainly constituted by $C_6N_7(NH_2)_3$ units interconnected by hydrogen bridges and a single units is formed by three anellated s-triazine rings and terminating by three N atoms in the positions 2, 5 and 8 of tri-s-triazine C_6N_7 block [5]. Melem unit cell is represented in Figure 2.4.

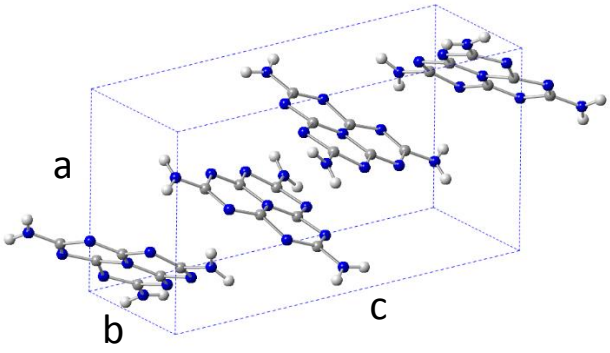

Figure 2.4: Unit cell of melem.

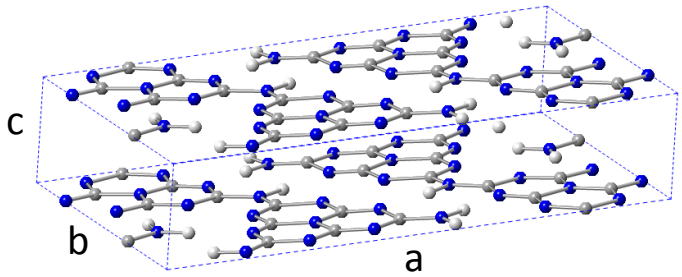

Figure 2.5: Liebig's melon unit cell.

Similarly to the case of trichloro-tri-s-triazine [11], the ring $C_6N_7(NH_2)_3$ is slightly distorted, composing two orientated layers alternating along *c*-axis with neighboring molecules forming an angle of about 40°. The interlayer distance is 327 pm very close to the graphite one (334 pm).

In our experimental conditions, the product obtained at 400 °C is not a single phase. As reported in figure 2.3, beside the two strong peaks at 2θ = 12.1 ° and 2θ = 13.3 ° originating from (100) and (002) reflections of melem phase, two other peaks at 2θ = 12.4° and 2θ = 13.6° are observed. Moreover, another well-defined peak at 2θ = 25.8 ° is not characteristic of a pure single phase.

To fully assign diffraction peaks and analyze the contribution of different phases, the XRD patterns were analysed by Rietveld refinement [9], employing the program Maud [10]. We used a trial-and-error approach reaching the best fit by considering two Melem phases, with different structural parameters.

Consequently, we present the fitting curve in Figure 2.6A and the best fit parameters, in good accordance with literature data [5], are shown in Table 2.1.

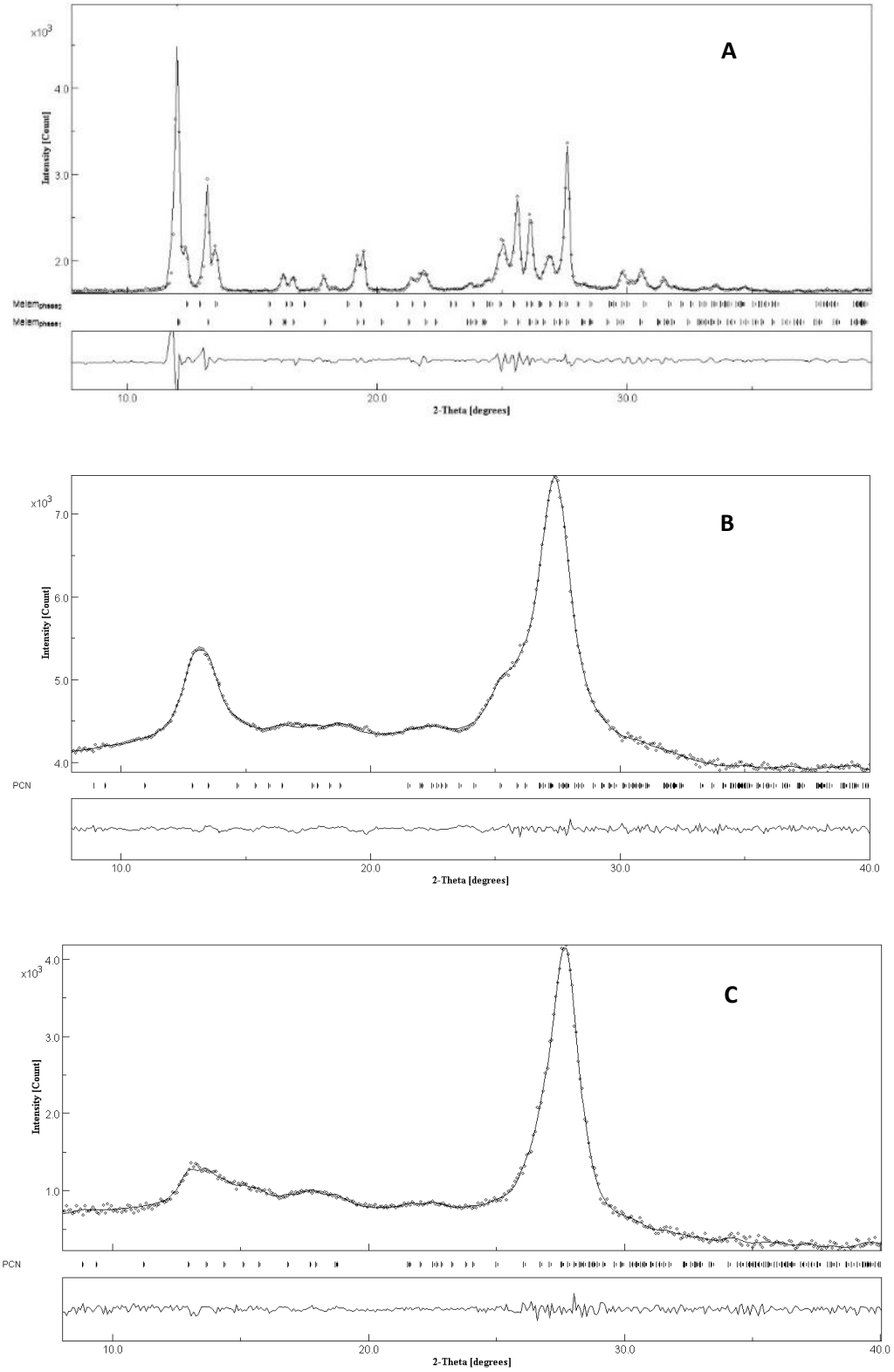

Figure 2.6: Rietveld refinement of carbon nitride structures obtained at temperature of 400 °C (A); 500 °C (B); 600°C (C).

Table 2.1: Structural parameter of melamine treated at 400 °C

Compound	Crystal system	Space group	Lattice parameters	w%
Melem	Monoclinic	$P2_1/c$	a = 7.4 Å, b = 8.8 Å, c = 13.6 Å; $\alpha = \beta$ = 90 ° , γ = 99.9 °	54.6
Melem	Monoclinic	$P2_1/c$	a = 7.2 Å, b = 8.5 Å, c = 13.7 Å; $\alpha = \beta$ = 90 °, γ = 107.4°	45.4

Table 2.2: Structural parameter of melamine treated at 500 °C

Compound	Crystal system	Space group	Lattice parameters	w%
PCN	Triclinic	$P1$	a = 16.2 Å, b = 12.1 Å, c = 3.4 Å; α = 89.9° , β = 99.0° , γ = 87.0°	100

Table 2.3: Structural parameter of melamine treated at 600 °C

Compound	Crystal system	Space group	Lattice parameters	w%
PCN	Triclinic	$P1$	a = 15.8 Å, b = 12.4 Å, c = 3.3 Å; α = 89.8° , β = 88.8° , γ = 86.6°	100

The XRD pattern at the higher temperatures results in wide reflections. The problem of solving structure can be addressed by using graphite as a reference model. Bulk graphite and nanosized graphite (like MWNT) present a characteristic diffraction peaks at around 27 ° originating from (002) plane of layered structure [5]. Taking into account the example of graphite, the main reflection of the sample at 500 °C and 600°C can understood by a graphite-like structure.

The best accord with experimental data of the sample at 500°C is obtained by considering a Liebig's melon structure (hereafter PCN, polymeric carbon nitride), suggested for the first time by Tybroski and co-workers [6] then confirmed by Fina et al [12]. After refinement, the structure presents cell parameters a =16.2 Å, b = 12.1 Å, c = 3.4 Å, α = 89.9°, β = 99.0°, γ = 87.0°. The main peaks are

located at 2θ (500°) = 27.3 ° and 2θ (600°) = 27.5 ° for the samples at 500 °C and 600 °C respectively, and they are attributed to (001) reflection. The corresponding interlayer distance are d_s (500°C) = 3.26 Å and d_s (600°C) = 3.24 Å, showing a reducing of the interlayer parameter as the annealing temperature increases. The reflection from (210) plane are measured at 2θ = 13.1° and 2θ = 13.3 ° related to the separation distance of heptazine chains.

The sample at 500°C shows three distinct peaks that can be correlated to the reflections of melem phase (sample at 400 °C). By the studying of the change of related parameters, we can individuate the general behavior of carbon nitride material as a function of temperature. After the realization of melamine polymer, the s-triazine units tend to condensate forming tri-s-triazine units. The heptazine framework at 400°C emerged from hydrogen bonds, is replaced with stronger –C(NH)C– covalent bonds between neighboring units at 500°C . Finally, the PCN single phase structure is obtained and its thermal treatment at 600 °C provides an approaching of polymers planes and a distortion of unit cell.

Algara-Siller and co-workers [13] proposed a triazine-based g-C_3N_4 structure (fig. 2.2a). The carbon nitride product was prepared starting with dicyandiamide monomer and creating a mixture of LiBr and KBr. The mixture was sealed in vacuum in a quarts tube and thermally treated at 600 °C. The final structure was studied by using TEM and scanning force microscopy [13]. In this context, we have to underlying the different growing procedures adopted, the use of eutectic mixture and annealing ambient conditions. The mentioned procedure tends to provide a graphitic structure as well, without the creation of heptazine units.

In order to demonstrate the presence of heptazine units in samples annealed at high temperature, an experimental corroborated by ab-initio calculations was performed and the results are discussed in the next section.

2.1.3 Vibrational and optical properties

As mentioned, the presence of few well-defined diffraction peaks in the XRD spectra of the samples annealed at temperature above 400 ° C makes hard the analysis of the their structures. This has motivated a heuristic approach in recent years, making the structure highly debated. The use of different characterization techniques allows in principle to improve the predictive process. In this regard, we are

presenting Raman and luminescence measurements to validate the assumptions made in the structural study on diffraction patterns**.**

2.2.3.1 Calculation details

All the calculations were carried out using Gaussian 09 code [20].

Raman spectra calculations for the optimized structures were performed in density functional theory (DFT) with the Becke's 3 parameters and the Lee–Yang–Parr's nonlocal correlation functional (B3LYP) [21],[22]. The basis sets for C, N, H were 6-31G (d,p). Analysis of frequencies confirms that optimized structures are at minimum of potential surface and no imaginary frequencies are obtained. Calculated frequencies were compared to experimental data after a scaling by a factor 0.98 due to the correction of the harmonic approximation. TD-DFT calculations in B3LYP functional approximation and 6-31G++(d,p) diffuse basis were used to predict absorption spectra.

2.2.3.2 Results

The samples prepared by thermal polycondensation of melamine were analysed by Raman scattering measurements in back scattering geometry with excitation wavelength at 1064 nm generated by Nd:YAG laser, to avoid luminescence contribution in the visible range. The system operates in Stokes region up to 2500 cm^{-1}. Accordingly, the experimental and theoretical data are investigated within this interval. Measurements were performed in air at room temperature with a spectrometer BWTEK i-Raman Ex with a spectral resolution of 9 cm^{-1}. All the spectra were collected with low power excitation (under 5 mW) concentrate in a spot of 1 mm^2.

Figure 2.7 reports the Raman spectra of thermal treatment of melamine at the temperature of 300, 400, 500 and 600 °C, acquired in the spectral interval among 150 and 1800 cm^{-1}.

The sample treated at 300 °C shows 8 well-defined Raman modes in the observation range, all attributable to vibrational modes of melamine. Some of them are resulting by a convolution of different contributions, unresolved in our experimental conditions. The spectrum is characterized by two intense modes at 675 cm^{-1} and 983 cm^{-1} ascribable to the ring breathing II mode and in-plane ring breathing I mode, respectively [23]. Figure 2.8 shows the displacement vectors of the two modes with A_1' symmetry.

Other contributions to light scattering, mainly originating by CN bending and NH_2 twisting, are summarized in table 2.4.

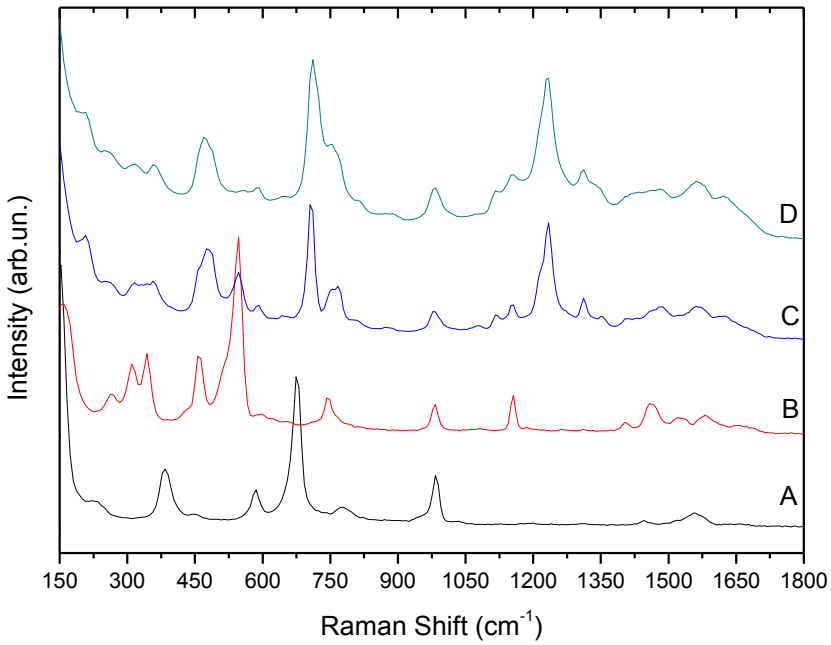

Figure 2.7: Raman spectra of melamine annealed at different temperature: A) T = 300 °C; B) T = 400 °C (melem); C) T = 500 °C (PCN); D) T = 600 °C (PCN).

Table 2.4: experimental and calculated data (cm^{-1}) of melamine annealed at T = 300 °C. β = bending mode; R= mode on ring atoms.

Experimental	Calculated	Assignment
233	210	β(HCNH)
386	330	β(HCNH)
583	527	β(NH)
	570	$\beta(CNC)^R$
675	668	Ring breathing mode II
782	724	$\beta(CN)^R$
982	968	Ring breathing mode I
-	1174	$\beta(CN)^R$
1444	1443	$\beta(NH)+\beta(CN)^R$
	1480	β(NH)
1556	1574	$\beta(NH)+\beta(CN)^R$
	1599	$\beta(NH)+\beta(CN)^R$
	1635	$\beta(NH)+\beta(CN)^R$

Table 2.5: experimental and calculated data (cm^{-1}) of melamine annealed at T = 400 °C. β = bending mode; R= mode on ring atoms.

Experimental	Calculated	Assignment
266	281	β(NH)
310	-	-
344	-	-
461	438	$\beta(NCNC)^{R}$
542	520	Ring breathing mode II (rbII)
591	574	$\beta(NH)+\beta(CN)^{R}$
	577	β(NH)
745	730	Ring breathing mode I (rbI)
979	981	$\nu(NCN)^{R}+\beta(NH)$
1157	1149	$\nu(NCN)^{R}+\beta(NH)$
-	1359	$\nu(CN)^{R}$
1405	1539	β(NH)
1467	1538	$\nu(NCN)^{R}+\beta(NH)$
1525	1603	β(NH)+ ν(CN)
1582	1634	β(NH)+ ν(CN)
1665	1656	$\beta(NH)+\beta(CN)^{R}$

Table 2.6: experimental and calculated data (cm^{-1}) of melamine annealed at T = 500 °C. β = bending mode; ν: stretching mode; R= mode on ring atoms; op = out of plane.

Experimental	Calculated	Assignment
205	200	ν(CN)
252	250	ν(CN)
315	334	ν(NH)

354	370	ν(NH)
476	474	Ring breathing mode II (rbII)
543	540	ν(NH)
590	584	$\beta(CNC)^{R} + \beta(NCNC)^{R}$
645	642	ν(CN)
707	695	$\beta(NCN)^{R} + \nu(CN)^{R}$
760	743	Ring breathing mode I (rbI)
806	781	ν(CN)
	800	ν(CN)
983	986	$\beta(NNNC)^{op}$
1078	1034	ν(CN)
	1068	ν(NH)
1117	1007	ν(CN)
1154	1149	ν(CN)
1232	1257	β(NCN)
	1264	β(NCN)
1312	1312	β(NCN)
1352	1354	β(CNCN)
	1365	β(NCN)
1406	1386	β(CNC)
1481	1500	ν(NH)
1565	1530	ν(NH)
1624	1611	β(HNCN)

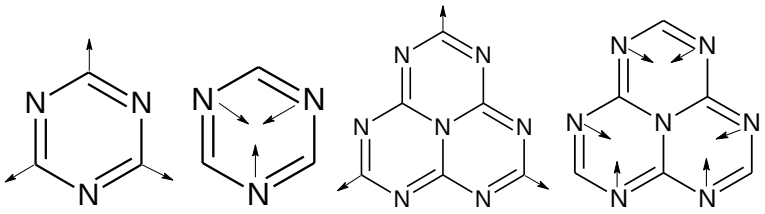

Figure 2.8: representation of characteristic ring modes of s-triazine and tri-s-triazine units.

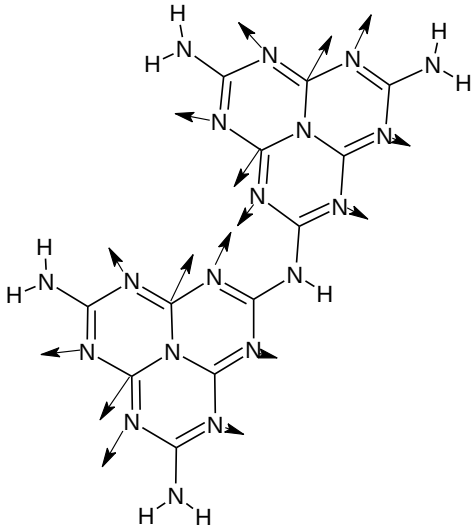

Figure 2.9: representation of displacement vectors of the mode at 707 cm^{-1}.

Raman spectrum of the sample treated at 400 °C can be understood by considering the vibrational response of the $C_6N_7(NH_2)_3$ heptazine unit [5]. At the formation of the molecule, the two ring breathing modes A_1' characteristic of triazine nucleus, are shifted at 542 cm^{-1} and 745 cm^{-1} because of the increase of reduced mass; furthermore the bending mode NCNC at 583 cm^{-1} in melamine results shifted at 461 cm^{-1}. Although most the experimental modes in the observed range are all attributable by modelling the single heptazine units, the frequencies at 310 cm^{-1} and 344 cm^{-1} are missing. Since their persistence in the sample at higher temperature, we assume that the polymerization process and the realization of bridging among neighbouring molecules originate the mentioned modes.

Despite of the modes in the interval between 300-350 cm^{-1}, the vibrational structure of melem is solved by considering the single heptazine units. This model is not sufficient for a correct description of vibrational features for the samples at higher temperature. Hence, a drastic approximated model of proposed melon was utilized. Figure 2.10 illustrates the molecular structure consisting of four heptazine units linked by amino groups used in the calculations.

Although the roughness of structure, the Raman modes are predicted with a good accuracy. As presented in Table 2.5, the rbI mode is at 760 cm^{-1} (745 cm^{-1} in melem) and rbII mode is at 476 cm^{-1} (542 cm^{-1} in melem). The vibration at 707 cm^{-1} is represented in Figure 2.9, originating from the break of symmetry arising from the strong linking between neighbouring heptazine units. The mode at 543 cm^{-1} is attributed to amino stretching NH, disappearing in PCN at 600 °C. Moreover, the vibrations at 315 and 354 cm^{-1} belong to NH stretching, confirming the hypothesis of a presence of small amount of heptazine units linked by amino groups at 400 °C.

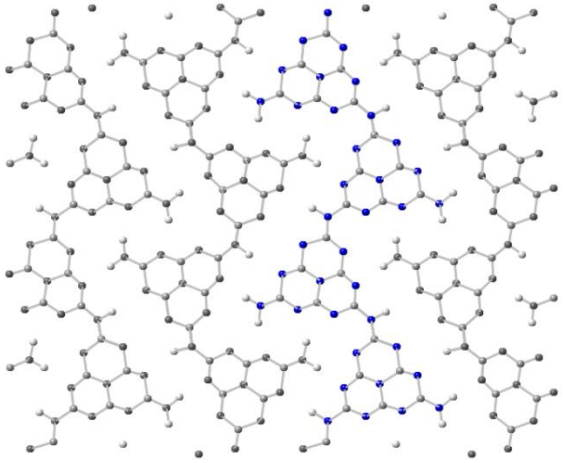

Figure 2.10: representation of PCN layer. The highlighted part report the chain model adopted for ab-initio calculations.

2.2.3.3 Optical properties

The condensation process determining the realization of carbon nitride crystals can arise from several CN precursors. Among them, melamine has been considered the most useful for production with yield greater than 70 % [24]. As showed by x-ray diffraction and Raman spectroscopy measurements, melamine condenses in melem after heat treatment at the temperature of 400 °C. A following increase of temperature at 500 °C, transforms the heptazine-based structure linked by hydrogen bonds into a g-C_3N_4. In this passage, we assist to a colour change from a white powder to a yellow one.

Experimental details. Photoluminescence excitation (PLE) and Steady state photoluminescence (SSPL) measurements were performed using the filtered light from a laser driven Xenon lamp (EQ-99-X) with a final bandwidth of about 1 nm.

Time-resolved photoluminescence (TRPL) measurements were performed by means of a streak camera (Hamamatsu C5680) coupled to grating spectrograph (Arc-Spectra-Pro 275i). Pulsed laser excitation source at λ_{exc} = 355 nm was provided by the third harmonic of Nd:YAG laser (Spectra Physics) with a pulse duration of 300ps and repletion rate of 1 KHz. The laser spot was focused on a 500 μm spot with a power of 0.2 mW. PL measurements were obtained in different time range: temporal resolution was 100 ps with a 20 ns time range and better than 40 ps in the range lower than 10 ns.

Quantum yield (QY) measurements were also performed with dedicated setup (Hamamatsu Quantaurus C11347-11).

Results and discussion.

PLE spectra were obtained by monitoring the maximum of PL emission. No changes in the emission response were observed along the excitation range explored. We identify a well-defined trend of PLE as a function of annealing temperature, that is, the structural transformation produces a redshift of excitation spectrum (fig. 2.11).

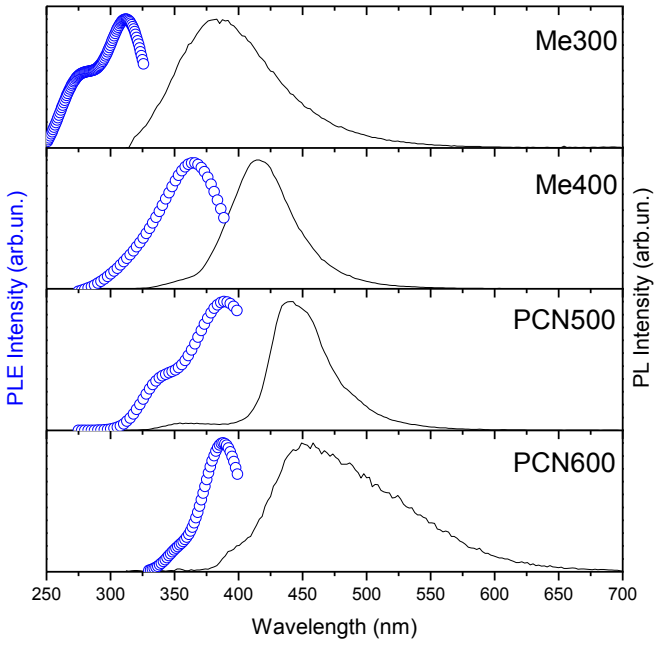

Figure 2.11: Photoluminescence Excitation (circles) and photoluminescence (solid line) spectra of Melamine treated at 300 °C (Me300), at 400 °C (Me400), 500°C (PCN500) and 600 °C (PCN600). PL spectra: Me300) λ_{em} =380 nm, λ_{exc}= 270 nm; Me400) λ_{em} =415 nm, λ_{exc} = 360 nm; PCN500) λ_{em} =440 nm, λ_{exc}= 380 nm; PCN600) λ_{em} =440 nm, λ_{exc}= 380 nm.

Figure 2.11 reports the normalized luminescence spectra of carbon nitride powders at different annealing temperatures with excitation at λ_{exc} = 250 nm. Connected to excitation spectra, PL spectra are all characterized by large emission bands with a progressive redshift of the emission maximum at the increase of temperature treatment. The sample Me300 seems to retain the feature of starting melamine powders with a redshift of maximum emission of about 20 nm, which can be assign to a formation of a polymer based on triazine units (see chap.3 for further details on melamine).

At the realization of melem (400 °C), the emission is peaked at λ_{em} = 415 nm and FWHM ≈ 400meV, (QY = 14 %).

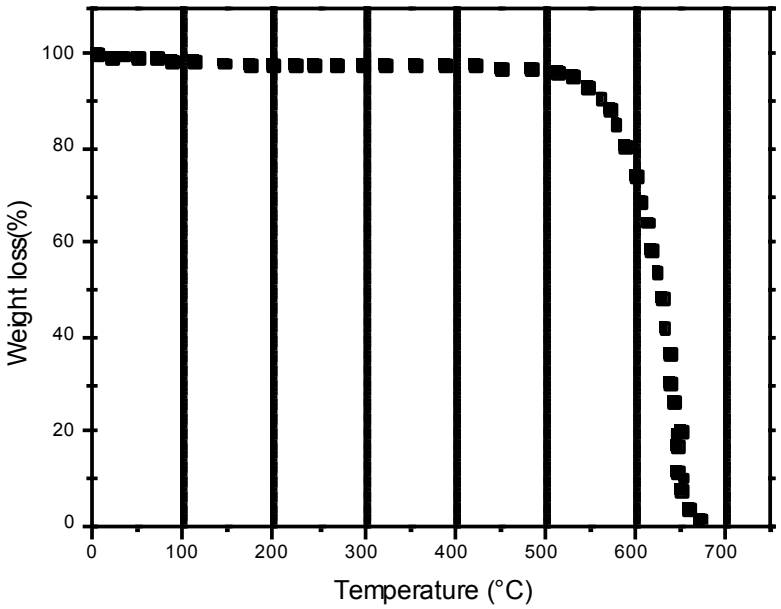

Figure 2.12: TGA graph of g-C_3N_4. Data from ref [1].

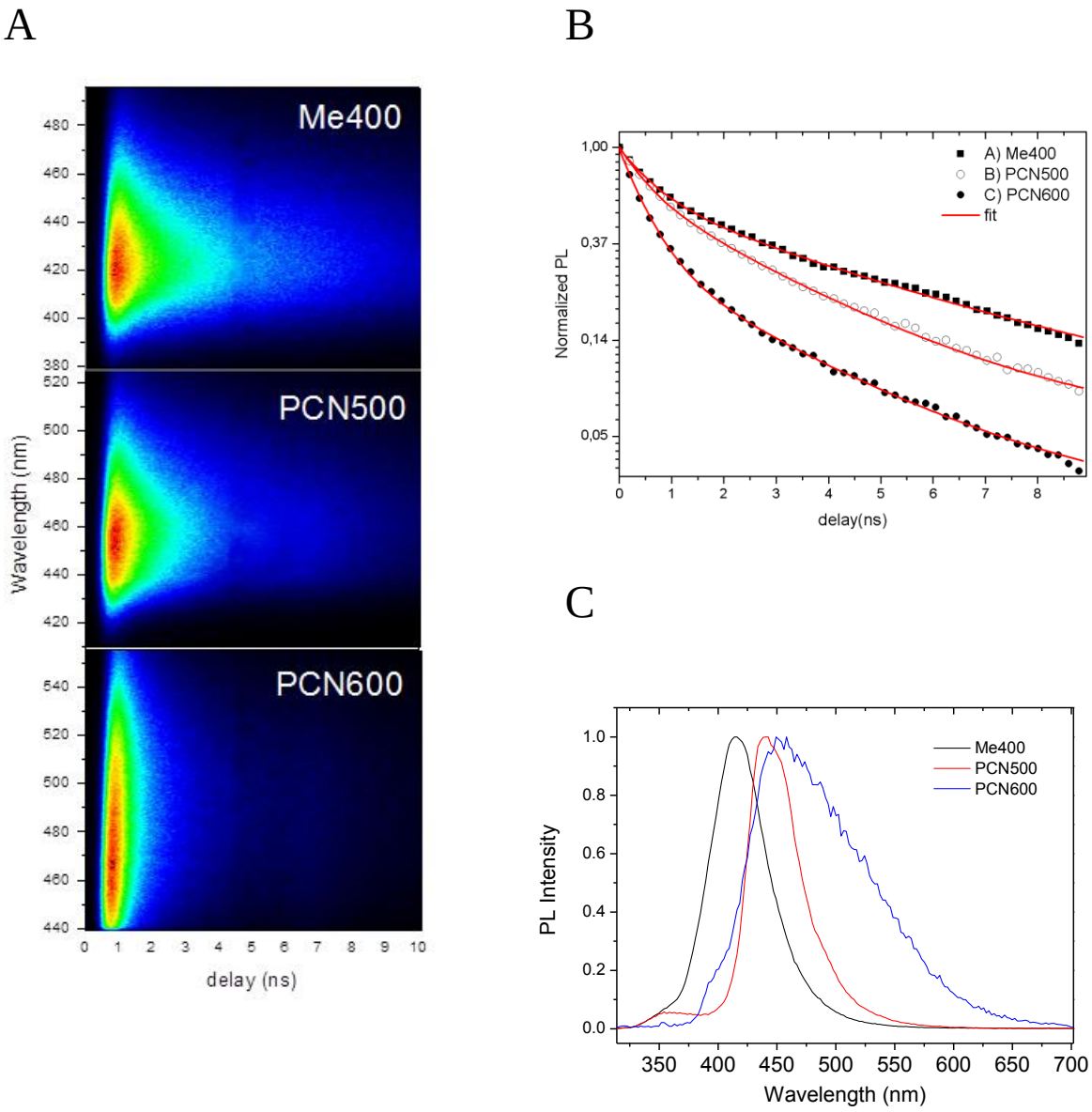

Figure 2.13: A) Spectrogram of time-resolved photoluminescence over 10 ns time range with 40 ps resolution from Me400, PCN500 and PCN600 samples. B) Time decay of PL measured in the 10 ns time range after the pulse laser. C) Normalized steady time luminescence of Carbon nitride samples.

Polyheptazine compounds (PCN) shows a maximum at λ_{em} = 440 nm (FWHM ≈ 310 meV) , with external QY = 8 % , significantly decreased in comparison to melem PL. At 600 °C, the polyheptazine powder seems not to suffer a further energy shift. On the contrary, we assist to an asymmetrical enlargement towards higher wavelengths (FWHM ≈ 600 meV). At the same time, luminescence efficiency decreases to a tenth of the polyheptazine QY.

Invoking the Thermogravimetric analysis (TGA) graph (fig. 2.12) and Raman spectra we can exclude heat-induced carbonation processes deteriorating the structure at 600 °C and we attribute the new optical features to the change of crystal parameter of melon structure.

Figure 2.13 reports the spectrograms from Me400, PCN500 and PCN600 carbon nitride samples excited at λ_{exc} = 355 nm. The spectral interval was about 116 nm and it was centered to different wavelengths, depending on the sample, in order to acquire the whole luminescence. The spectrograms reveal different temporal evolution of luminescence with a decrease of PL time decay as a function of synthesis temperature. The right side of Figure 2.13 contains the development of PL spectrally integrated on the interval of investigation. In the range of 10 ns, TRPL presents two components, one of them with sub-nanosecond decay.

Several model were proposed to interpret TRPL experimental data [16], without encouraging results. To date, only data on several tens of nanoseconds have been reported and we guess that most of the failure in fitting data could be ascribed to the investigation time range that cannot appreciate the faster recombinations phenomena.

Time resolved data can be well fitted by two exponentials law

$$I(t) = I_1 \exp\left(-\frac{t}{\tau_1}\right) + I_2 \exp\left(-\frac{t}{\tau_2}\right) \tag{2.16}$$

with

$$\frac{1}{\tau} = \frac{1}{\tau_r} + \frac{1}{\tau_{nr}} \tag{2.17}$$

where τ_r and τ_{nr} represent radiative and non-radiative lifetime contribution to the overall time decay τ. Table 2.7 summarises our best fit parameters with an accuracy of ± 0.04 ns.

Table 2.7: PL lifetimes of Me400, PCN500 and PCN600.

	τ_1 (ns)	τ_2 (ns)
Me400	0.74	4.90
PCN500	0.54	3.04
PCN600	0.49	3.04

Me400 shows a PL decay with a fast component $\tau_1 = 0.74$ ns and a low component $\tau_2 = 4.90$ ns. With the realization of PCN, the kinetic of luminescence turns out changed and the two the lifetime decrease. At 600 °C the structure does not undergo to a further phase transformation and τ_2 is not altered. On the other hand, τ_1 is reduced to 0.49 ns.

Figure 2.14 represents the PL spectral profile of the three samples as a function of time delay from the laser pulse and with different time integration windows. PL spectrum of Me400 results essentially unchanged as the function of time, with a small enlargement and redshift in the second time window (2-20 ns). This effect gets higher for PCN500, which presents a redshift of 5 nm and more important for PCN600, whose redshift is about 10 nm.

Two main channels of recombination are observed in carbon nitride samples, carrying to two PL decay lifetime. The sub-nanosecond lifetime τ_1 decreases with respect to annealing temperature, with the lowest value in PCN600. The slow component τ_2 presents similar trend and it shortens by approximately 2 ns, being $\tau_2 = 3.04$ ns for PCN samples. The recombination channels result sensitive to the formation of bonds between heptazine units by amino groups, i.e. in melem to PCN transformation, yielding to a higher probability of recombination. In contrast, the change of PCN lattice parameters with the increase of temperature, does not influence the slow component, unaltered in the two samples.

Although the PCN is based on the heptazine structure, whose vibrational and optical properties can be described following similar molecular system, it becomes difficult to arrive at a complete description of the polymeric system without considering the interaction between neighboring units. Among the complexity of the electronic excitations, we have to pay attention to the following way of light absorption by carbon nitride based polyatomic molecules [17]: absorption by nonbonding electrons, not involved in the formation of chemical bonds and belonging to a localized group of the molecule; absorption by bonding electrons, typically leading to the dissociation of the molecule; absorption by nonbonding but delocalized electrons spread over the entire molecule or a large part of it.

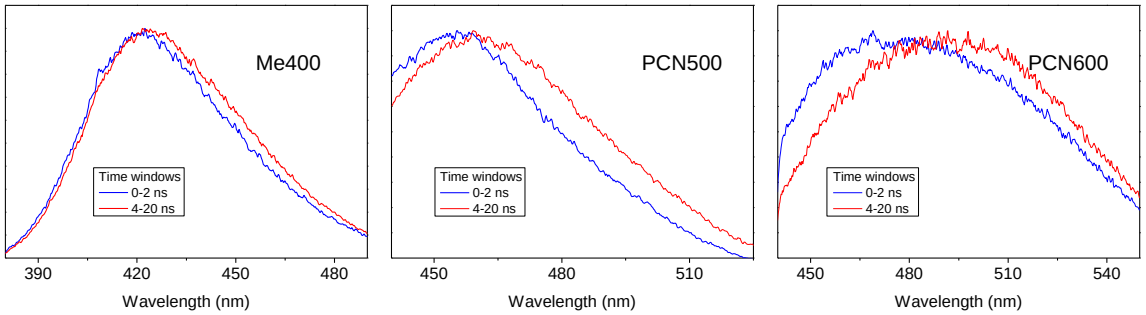

Figure 2.14: Photoluminescence spectra as a function of time delay with respect to the laser pulse for Me400, PCN500 and PCN600 samples: delay 0-2 ns time window (blue line), delay 2-20 ns (red line).

In carbon nitride system we identify three different states, namely sp^3 C-N σ band, sp^2 C-N π band and lone pair state of the bridge nitride atom [24].

In general, we observed a redshift of luminescence emission of carbon nitride samples at the increase of annealing temperature. The redshift of the luminescence of Me400 in comparison with the sample annealed at 300 °C, can be understood by the formation of the aromatic molecule larger than the s-triazine, which composes the melamine precursor powder and the condensate system at 300°C. Qualitatively speaking, the aromatic molecules can be modelled as a particle, i.e. the optical electron, in a linear box (the aromatic ring system) [25]. According to a simplest quantum model, the energy separation between highest occupied and lowest unoccupied orbitals reduces, as the box dimension becomes longer [26]. Hence, a shift of emission spectra toward the longer wavelengths is expected as the π system increases.

Serving as an example, naphthalene (two aromatic rings) emits with a luminescence picked at about 470 nm and anthracene, containing three rings, presents luminescence at 670 nm [[26].

The increase of annealing temperature affects the molecular structure of carbon nitride system. At 400 °C the change electronic levels distribution and the resulting redshift of PLE and PL features, is motivated by the increase of the π system. In this framework, we assert that the luminescent transitions in Me300 and Me400 are ascribable to molecular excitons that are generated and recombine at the monomers, which are linked by hydrogen bonds with very weak interactions.

At the formation of PCN, heptazine's units form stacked layers by amino groups links. The polymeric structure presents a new configuration of electronic levels and a redshift of the optical features is observed (fig. 2.11). Indeed, the simulated absorption characteristics tri-s-triazine reported in Figure 2.15 as a function of the number of units linked by amino groups clearly show that the larger is the number of tri-s-triazine units, the smaller is the S_0-S_1 absorption energy.

Summarizing, we pointed out the strict correlation between structural and optical properties in heptazine polymers obtained in different temperature regime. The experimental XRD data and Raman spectra were analyzed and corroborated by the means of computational models, providing deep insight in the morphological behavior of the polymers as a function of the growth conditions. As previously reported [16], due to the presence of amino groups, the character of the whole system is not aromatic, resulting in negligible overlapping of the molecular orbitals among heptazine units and, hence, in weak interaction among single monomers, as in the case of Me400.

Further increasing the annealing temperature the PCN structure is achieved and no more variation in the excitation and emission spectra were observed related to the planar interaction among heptazine units. Accordingly, the process at higher temperature reduces the distance between neighboring planes (XRD data, fig. 2.6 and Table 2.2), increasing the interaction between planes and consequently the non-radiative recombination on different sites. It results in a FWHM enlargement of about 300 meV and in a decrease of the faster time decay component τ_1 (Table 2.7).

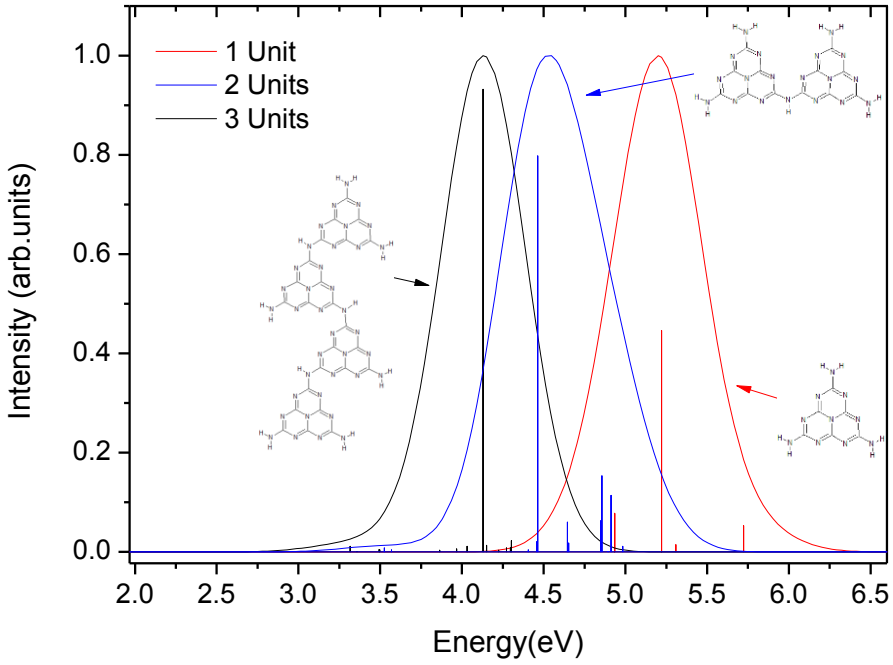

Figure 2.15: Calculated vertical excitation energies as a function of the tris-s-triazine units. The lines correspond to the unbroadened absorption energies. The spectra have been normalized and simulated with a Gaussian broadening with σ = 0.3 eV.

2.2 Triazine based compounds.

In the previous paragraph, we studied the structural and optical properties of carbon nitride materials. By the means of melamine as precursor, compounds with different excitation an emission features were obtained. In particular, we observed that melem structure, achieved at the temperature of 400 °C, represents a good blue emitter with the good quantum efficiency (~14%) and maximum PL emission at about 400 nm. Increasing the annealing temperature, we are able to tune the optical response, extending the luminescence in the green region of visible range. However, as observed the temperature induced process determines a lowering of the quantum yield. The effect of temperature process was the change of crystal parameters and the reducing of the distance between melon layers, making more likely non-radiative recombinations.

In this section, we present some results on substituted triazine systems.

1,3,5-triazine derivatives belong to a class of organic compounds with a large variety of potential applications. The current recognized fields of applications of heterocycles compounds as optical emitters involve molecular probes [27], organic light emitting diodes [28]and solar cells [29].

Here we report three compounds based on s-triazine core, with different terminating groups: cyanide (-CN), methyl ($-CH_3$) and methoxyl groups ($-OCH_3$).

2.2.1 Experimental details.

UV−Vis absorption measurements were carried out by means of a spectrophotometer Perkin-Elmer Lambda 15 (spectral bandwidth 2 nm) in the 250−700 nm range.

Steady state photoluminescence (SSPL) measurements were performed using the filtered light from a laser driven Xenon lamp (EQ-99-X) with a final bandwidth of about 1 nm.

Raman scattering measurements were performed in backscattering geometry at room temperature with a compact BWTEK i-Raman EX integrated system (spectral resolution of about 9 cm^{-1}) equipped with a microscopy system. The powders were irradiated with the 1064 nm line of a Nd:YAG laser.

Time-resolved photoluminescence (TRPL) measurements were performed by means of a streak camera (Hamamatsu C5680) coupled to grating spectrograph (Arc-Spectra-Pro 275i). Pulsed laser excitation source at λexc = 355 nm was provided by the third harmonic of Nd:YAG laser (Spectra Physics)with a pulse duration of 300ps and repletion rate of 1 KHz. The laser spot was focused on a 500 μm spot with a power of 0.2 mW. PL measurements were obtained in different time range: temporal resolution was 100 ps with a 20 ns time range and better than 40 ps in the range lower than 10 ns.

Synthesis:

4,4',4''-((1,3,5-triazine-2,4,6-triyl)tris(azanediyl))tribenzonitrile. CNTT

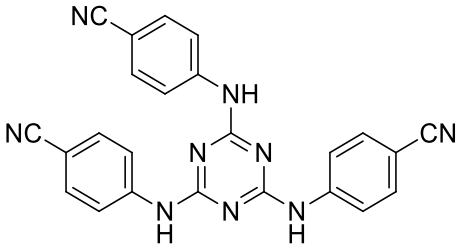

Cyanuric chloride (184 mg, 1 mmol) was dissolved in toluene (4 ml) and 4-aminobenzonitrile (354 mg, 3 mmol) was added, followed by a solution of NaOH (120 mg, 3 mmol) in water (1 ml). Reaction mixture was heated to reflux for 16h, and the resulted suspension was filtered and washed with water to give the product as a white solid, 296mg, 69%. m.p. >300°C.

N2,N4,N6-tri-p-tolyl-1,3,5-triazine-2,4,6-triamine. MeTT

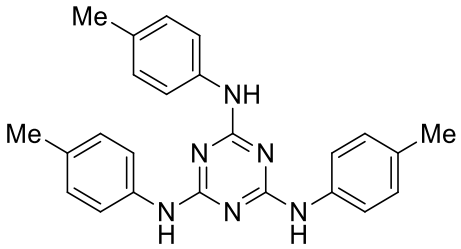

Method A; Cyanuric chloride (1 mmol, 184 mg) was dissolved in dioxane (20 ml), and p-toluidine (642 mg, 6 mmol) was added, followed by potassium carbonate (830 mg, 6 mmol). The reaction mixture was heated to reflux overnight, concentrated under reduced pressure and the residue was partitioned between water and ethyl acetate. The organic phase was washed with water and brine, dried over Na_2SO_4 and concentrated. The obtained off-white solid was suspended in hot ethanol (75ml) and filtered. The product precipitated from ethanol as a white solid, 114 mg, 29%. m.p. 238-240°C.

Method B; Following a method described by Sha4 Cyanogen chloride (3,33 mmol, 600 mg) was dissolved in a mixture of dioxane (15ml)and DMF (1,5 ml), and p-toluidine (1,07 g, 10 mmol) was added followed by NaHCO3. The reaction mixture was then refluxed under microwave heating, 300W, for 20 min. Solvent was concentrated under reduced pressure, the residue was suspended in water and filtered to give the product as a white solid, 1,27 g, 97%.

N2,N4,N6-tris(4-methoxyphenyl)-1,3,5-triazine-2,4,6-triamine. OMeTT

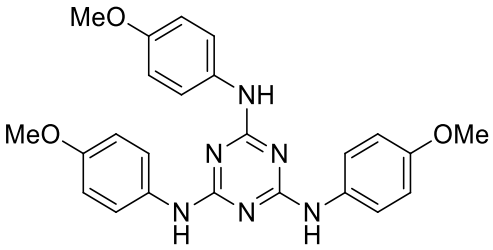

Cyanuric chloride (184 mg, 1 mmol) was dissolved in THF (10 ml). DIPEA (0.60 ml, 3.5 mmol) and a solution of p-anisidine (430 mg, 3.5 mmol) in THF (5 ml) were added and the reaction mixture was heated to reflux for 72h. The reaction mixture was concentrated on silica and column chromatography (40% EtOAc in hexane) gave the product as a palebrown solid, 100 mg, 22%. M.p. 212-214 °C.

2.2.3 Vibrational and optical properties

The vibrational properties of phenyl-s-triazine-2,4,6-triamine derivate have been studied by using DFT computational approach by the means of Gaussian09 package [20] with the procedure described in previous paragraph.

Moreover, a carefully attributions of Raman modes can be done by studying the characteristic vibration of molecular group, as cyanide, phenyl and methyl [30]. By considering the coordinations of the three compounds, we expected common features in vibrational response.

The problem of Raman attribution can be addressed by considering molecular system containing phenyl groups and their derivates [31]. As for several cyanoanilines molecules, 4-Aminobenzonitrile (4ABN) is well documented in literature[31], reporting both experimental and theoretical studies on vibrational modes [[32]-[35]]. Palafox an co-workers [31] reported a detailed analysis of Phenyl groups IR and Raman active modes. 4BN shows the strongest Raman modes at 1602 cm^{-1}. Our systems present the strongest Raman mode at 1615 cm^{-1} (CNTT), 1618 cm^{-1} (MeTT) and 1620 cm^{-1} (OMeTT), attributable to ν(CC) mode in the form of the characteristic phenyl quadrant ring stretching with a weak interaction with bending β(CH)[30] . Other intense modes are present in the region between 1100 cm^{-1} and 1460 cm^{-1}[31]. According to our calculations, we attribute the frequencies at about 1180 cm^{-1} to C-H bending with a negligible contribution of C-C stretching. This mode is proper of para-substitutes benzenes, hence it is substantially unaffected by substituent groups [30]. The remaining frequencies involve in-plane bending mode of C-H with the exception of the frequency at about 1320 cm^{-1}, generated by C-C sextant stretching. In the 800-950 range cm^{-1}, we observed the out-of-plane C-H bending, without motion of substituents, therefore substituent insensitive.

The vibration at about 780 cm^{-1} consists of an in-plane C-C quadrant bend, interacting with substituents. This justifies the shift at 826 cm^{-1} for OMeTT.

The characteristic bending mode of methyl group, observed in MeTT and OMeTT, are located among 1350-1500 cm^{-1}.

Cyanide ions typically present a characteristic stretching C≡N vibration in the region among 2000-2300 cm^{-1} and the mode at 2230 cm^{-1}, only in CNTT, is attributed to triple bond in CN terminal group.

At 986 cm^{-1} we identify the ring breathing mode I while the second s-triazine characteristic mode is not observed.

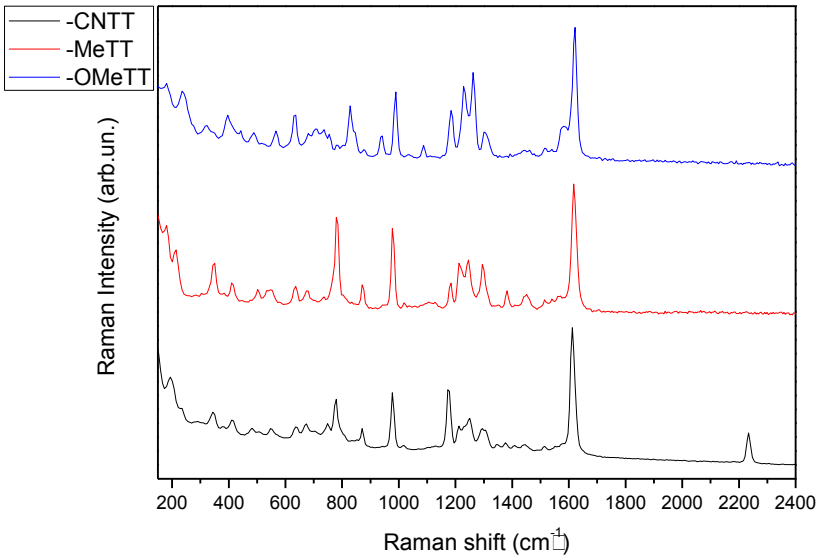

Figure 2.16 : Raman spectra of CNTT, MeTT and OMeTT.

Table 2.8: Experimental and Calculated Raman active modes (cm^{-1}) of CNTT, MeTT and OMeTT. β = bending mode; ν: stretching mode; op = out of plane.

CN		Me		OMe		Assignement
Exp	Calc	Exp	Calc	Exp	Calc	
2230	2345					CN stretch
1615	1626	1618	1626	1620	1637	Phenyl quadrant ring stretch
		1565	1578	1580	1578	β(NH)+ ν (CN)
1539	1565	1539	1564	-	1564	β(NH)
-	1533	1515	1531	1515	1542	ν (CC)
		1450	1489	1452	1479	$\beta(CH)^{twisting\ methyl}$
		1379	1390	-	1391	$\beta(CH)^{wagging\ methyl}$
1316	1260	1296	1253	1300	1277	ν (CC)
1248	1245	1243	1216	1262	1249	β(NH)+ β(CH)
1219	1222	1214	1210	1230	1211	β(CH)
1182	1177	1183	1185	1184	1185	β(CH)
				1088		
986	953	976	952	985	950	Ring breathing mode I
942	903	942	923	938	933	$\beta(CH)^{op}$
850	901	871	903	877	893	$\beta(CH)^{op}$
778	777	780	778	826	780	β(CC)
642	694	635	688	631	686	β(CC)+ β(CN)
550		549				
		501		488		
445				487		
443				443		
409	436	415		396	408	β(CC)
341		346	340	341		$\beta(CH)^{op}$
		210	215	240	246	β(CH)
179		176	187	176		β(CN)

2.2.3 Optical properties

In order to explore the optical properties of triazine-derivates, the compounds were dissolved in an appropriate solvent. CNTT resulted soluble in acetone or DMSO, while MeTT and OMeTT were soluble in ethanol or DMSO. The mixtures were studied in the range of 10^{-5} - 10^{-3} M, verifying the linear response of optical properties and excluding concentration induced quenching effects. Here we report the results on sample at 10^{-4} M. Moreover, we observed that the PL from triazine compounds were unaffected by the nature of solvent and corresponded to the luminescent emission of solid state.

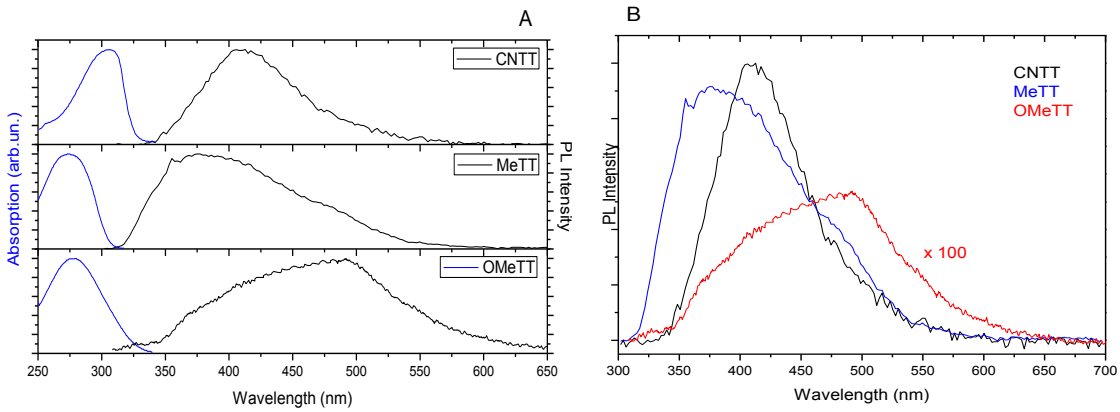

Figure 2.17: A) Optical Absorption and Photoluminescence spectra of triazine based compounds in solution. Concentration: 10^{-4} M. Solvent: DMSO. The PL were excited in continuous wavelength regime at the maximum of absorption: CNTT λ_{exc} = 300 nm; MeTT λ_{exc} = 274 nm; OMeTT λ_{exc} = 277 nm. B) Comparison of PL intensities.

Figure 2.17 shows the absorption spectra of triazine compounds in DMSO solution (10^{-4} M). MeTT and OMeTT present the maximum of absorption at 274 nm and 277 nm, respectively. In CNTT, the absorption band is peaked at 300 nm, showing a redshift of about 25 nm in comparison with methyl-terminated molecules. C≡N group presents localized and vacant π orbitals, tending to introduce a vacant orbital between the highest occupied and the lowest unoccupied π orbitals of the unsubstituted molecule, resulting in a smaller energy gap HOMO-LUMO with respect to the other two compounds. The functional group of CNTT derives from a 4ABN system, a benzene derivate substituted by the electron-donating NH_2 group and an electron-withdrawing CN group [36],[37]. Then, light absorption is expected to promote an electron transfer from a π orbital of aromatic ring to a vacant π orbital of CN group [25].

On the contrary, methoxy group in p-substituted benzene is considered a good electron-donor from lone pair to a vacant π orbital of the aromatic ring [26], while $–CH_3$ group presents neither donating nor accepting character form aromatic ring.

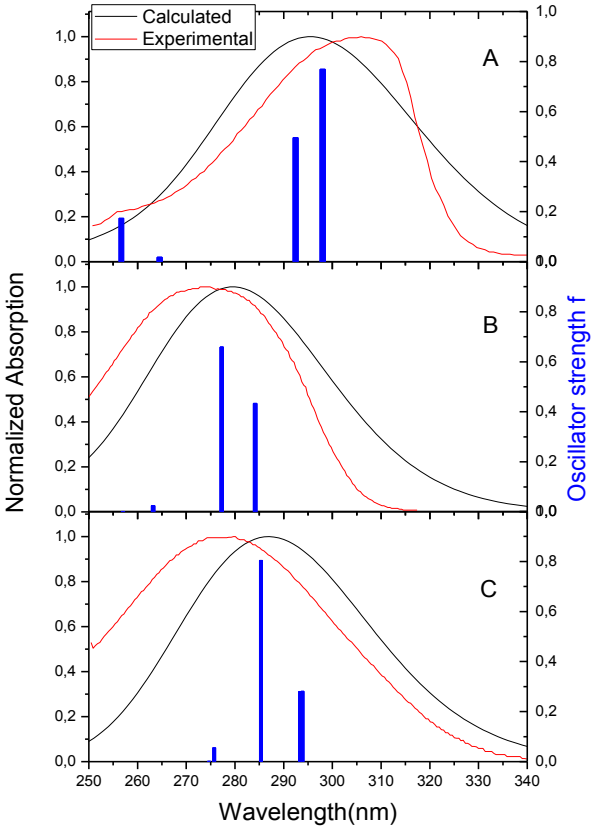

Figure 2.18: Calculated and experimental absorption spectra of A) CNTT, B) MeTT and C)OMeTT. Vertical lines corresponds to oscillator strengths f.

Figure 2.18 reports the calculated vertical excitation energies and the oscillator strengths for singlet states in comparison with the experimental data. For the sake of clarity, Gaussian convolutions of theoretical results are also reported. TD-DFT calculations reproduced correctly the trend of optical absorption depending on functional groups. It is important to evidence the lowest wavelength absorption ($\lambda_{(exp)}$ = 300 nm; $\lambda_{(calc)}$ = 295 nm) for CNTT, as well as the influence of methoxy and methyl groups between OMeTT ($\lambda_{(exp)}$= 280 nm; $\lambda_{(calc)}$ = 295 nm)and MeTT ($\lambda_{(exp)}$= 274 nm; $\lambda_{(calc)}$ = 287 nm) samples.

Interestingly, functional groups influence the time decay of photoluminescence, as rendered in Figure 2.19. The three compounds were excited at λ_{exc} = 355 nm with the modalities explained in the last section. The kinetic parameters are reported in Table 2.9. Time decays of PL were monitored in first

5 ns after the laser pulse. In this range, the profile of integrated PL of MeTT is fitted by a single exponential law and with resulting lifetime τ = 1.96 ns. CNTT and OMeTT PL decay present a double exponential character, with the faster lifetime of 0.44 ns and 0.29, respectively. The nature of the fast lifetime is ascribable to energy transfer effect from withdrawing and releasing groups among the s-triazine and the terminating –CN or OMe groups. While the transfer process is very efficient in the s-triazine – amino system, the optical efficiency in the s-triazine – methoxy system is lowered to fractions of percentage. This behavior is related to the different affinity between the terminating groups and the triazine core, where the s-triazine is a high electron donating systems, –CN represent a high withdrawing electron system while -OMe weak electron accepting[38].

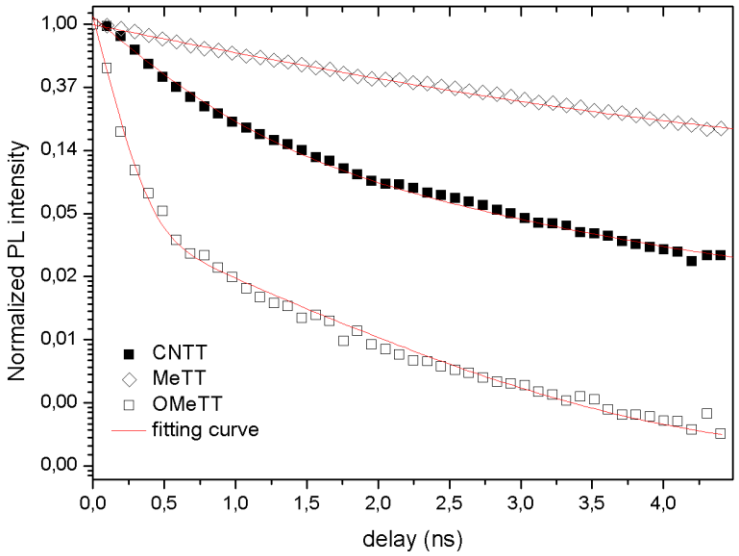

Figure 2.19: Time resolved PL of CNTT, MeTT and OMeTT

Table 2.9: lifetime of PL decay in CNTT, MeTT and OMeTT

Samples	Lifetimes (ns)	
	τ_1	τ_2
CNTT	0.44	1.66
MeTT	-	1.96
OMeTT	0.29	1.63

2.3 Tuning the optical properties of benzonitrile substituted triazine

Upon thermal treatment at 200 ° C in air, the methyl and methoxy terminating molecules (MeTT, OMeTT) turn into brownish and undergo significant changes in the emission spectrum with loss of efficiency, probably related to a carbonization process. On the contrary, the cyanide group (in CNTT sample) enhance the thermal molecule stability up.

A thermal treatment in air at 300 ° C transforms the molecule into a yellowish product, with new emission features.

Firstly, we investigated possible and significant changes in the molecular structure, that is thermal induced damages or transformations (change of phase). For this purpose, XRD pattern were obtained from the as-prepared 4, 4', 4''-((1,3,5-triazine-2,4,6-triyl)tris(azanediyl))tribenzonitrile (CNTT) and from treated sample at the temperature of 300 °C for 2h. The XRD pattern are reported in figure 2.20 and the observed peaks are summarized in table 2.10. XRD of the samples were recorded at room temperature in the range $8° \leq 2\theta \leq 80°$. Examining the figure 2.20, we observe several sharp reflections for both the samples. The main peaks revealed in CNTT are preserved or lightly shifted after the temperature treatment, indicating the retaining of the lattice structure. However, other weak reflections appear in CNTT_300, probably due to the presence of a new phase.

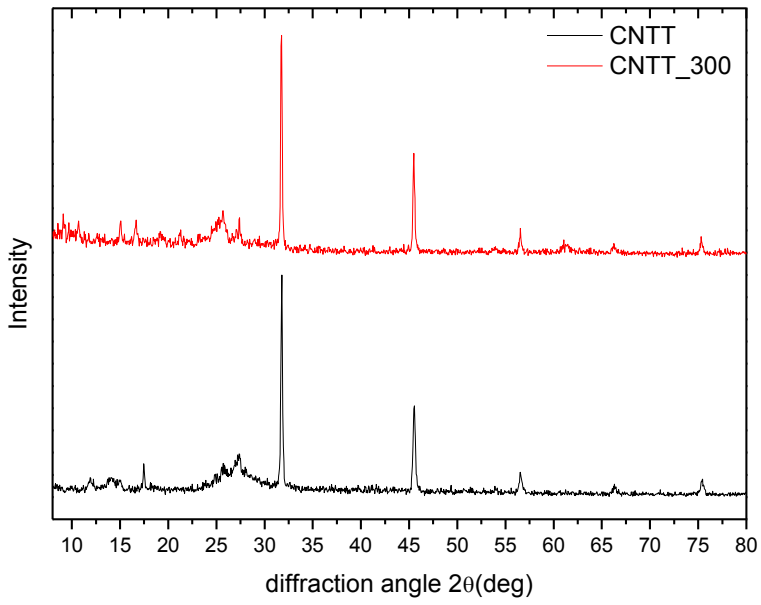

Figure 2.20: XRD pattern of CNTT and CNTT_300 samples.

As previously emphasized, Raman scattering is particularly sensitive to molecular building blocks. Raman measurements better clarify possible transformation in the CNTT triazine structure. The annealed product exhibits the same vibration modes of the as-prepared molecule with a background that we attribute to a residual luminescence under excitation at 1064 nm. In particular, we observe the ring breathing mode of triazine and the phenyl quadrant stretching at 981 cm^{-1} and 1610 cm^{-1}, respectively.

Table 2.10: XRD peaks of CNTT and CNTT_300 ($8° \leq 2\theta \leq 80°$).

CNTT 2θ (deg)	CNT_300 2θ (deg)
11.9	10.7
14.1	-
15.0	15.1
17.3	16.7
-	19.2
-	21.2
25.7	25.7
27.2	27.4
31.8	31.7
45.5	45.5
56.5	56.5
-	61.3
66.3	66.3
75.4	75.3

Furthermore, CNTT_300 shows the characteristic C≡N stretching mode at 2226 cm^{-1} and correspondently the distinctive modes of NH bending group and CC stretching at 1240 cm^{-1} and 1312 cm^{-1}. XRD and Raman spectroscopy measurements revealed that the molecular structure of CNTT results unchanged after heat treatment (fig.2.21).

Despite the similarity of the structures, unexpected, the annealed powder produces a wide and symmetrical emission extending in the visible interval with emission maximum at 530 nm (figure 2.22)

with respect the pristine CNTT compound. The absorption spectrum displays the new properties in comparison with the pristine powder. The latter showed the absorption maximum at 300 nm (fig.2.17A) and the corresponding emission was peaked at about 400 nm. After the annealing, CNTT excitation results red-shifted from 300 nm to 390-400 nm.

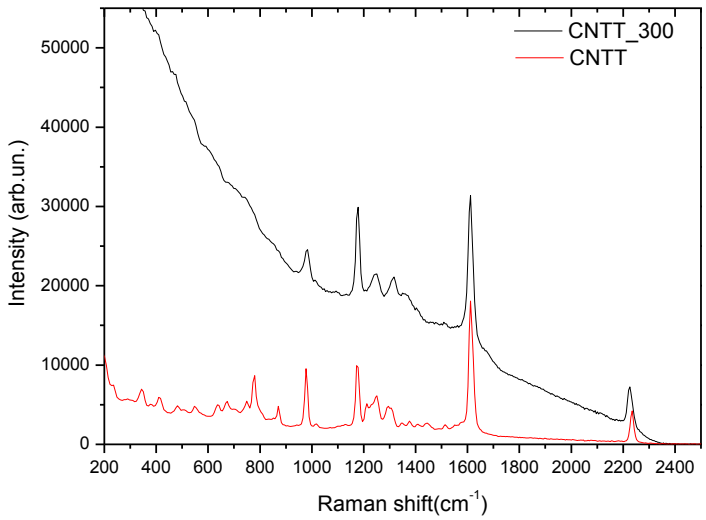

Figure 2.21: Raman spectrum of CNTT and CNTT_300 (treatment at 300°C).

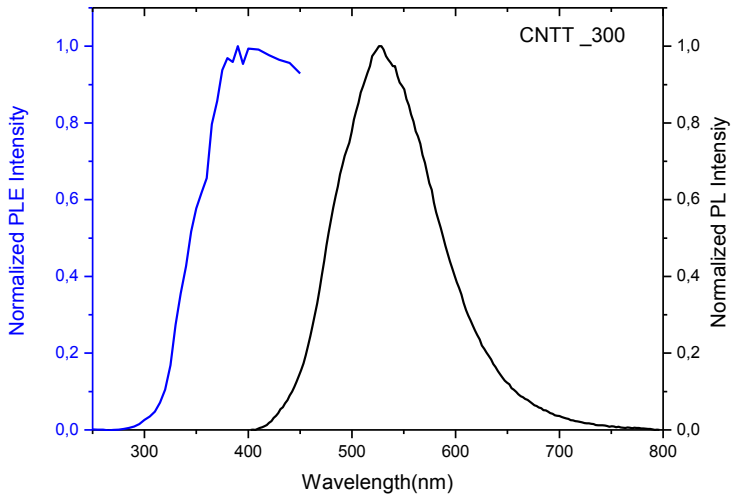

Figure 2.22: Excitation and Photoluminescence spectra of CNTT sample treated at 300 °C. PL were excited in continuous wavelength regime at the maximum of absorption: CNTT λ_{exc} = 300 nm; MeTT λ_{exc} = 274 nm; OMeTT λ_{exc} = 277 nm.

In order to gain deep information on the kinetics of the recombination, time resolved photoluminescence were performed in different ns time ranges.

Figure 2.23 shows the time resolved profile of PL of CNTT and CNTT_300 samples. No difference is revealed in the first 5 ns time window.

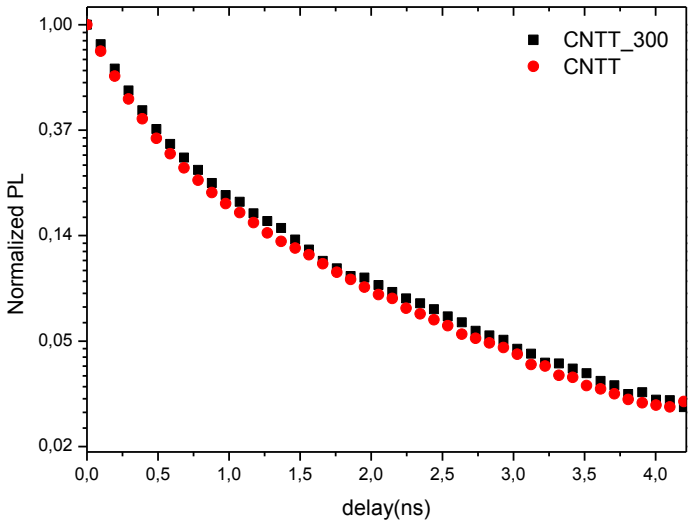

Figure 2.23: Time decay of PL measured in the 5 ns time range after the pulse laser (detector: streak camera).

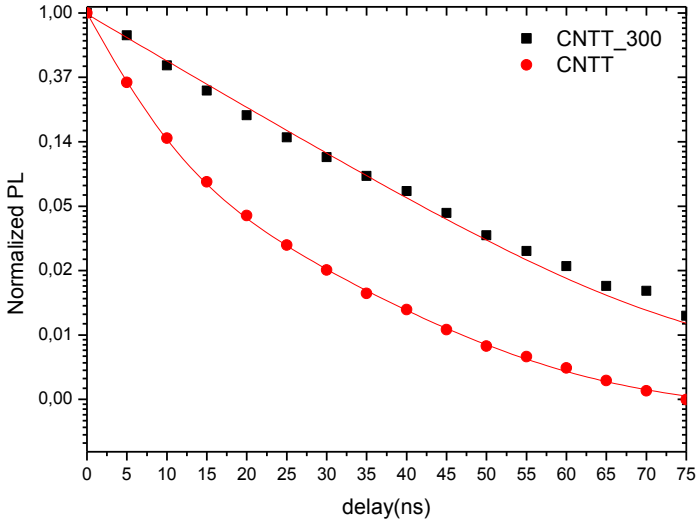

Figure 2.24: Time decay of PL measured in the 100 ns time range after pulse laser (detector: gatable CCD).

In order to better study the PL temporal evolution, the time interval of investigation has to be extended to higher delay time values. Since the time range measured by the adopted streak camera does not exceed

20 ns, we utilized a gatable intensified CCD (Princeton Instruments PIMAX), allowing to explore time delay up to 100 ns. The experimental data in figure 2.24 were fitted by two exponential functions, whose parameters are summarized in Table 2.11.

Table 2.11: Fitting parameters for normalized PL time decay.

Sample	τ_1 (ns)	τ_2 (ns)	I_1	I_2
CNTT	4.0	13.7	0.85	0.15
CNTT_300	4.0	13.7	0.02	0.98

It can clearly be inferred from Table 2.11 that both samples are characterized by two components with lifetimes τ_1 = 4.0 ns and τ_2 = 13.7 ns, but with different weights in decay profile. In particular, we underline that the longer component with amplitude I_2 in CNTT become the greatest in CNTT_300, contributing with and amplitude near the unit. The PL spectra were monitored at different time delays to individuate the origin of the two components.

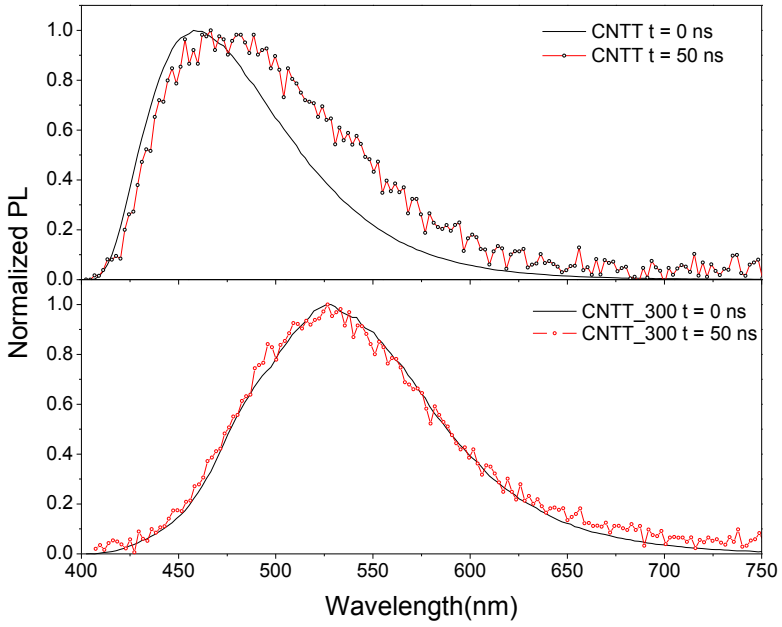

Figure 2.25: PL spectra acquired with a gate Δt = 5 ns. On top: CNTT PL at t = 0 ns (black line) and t = 50 ns (red line). On bottom: CNTT_300 PL at t = 0 ns (black line) and t = 50 ns (red line).

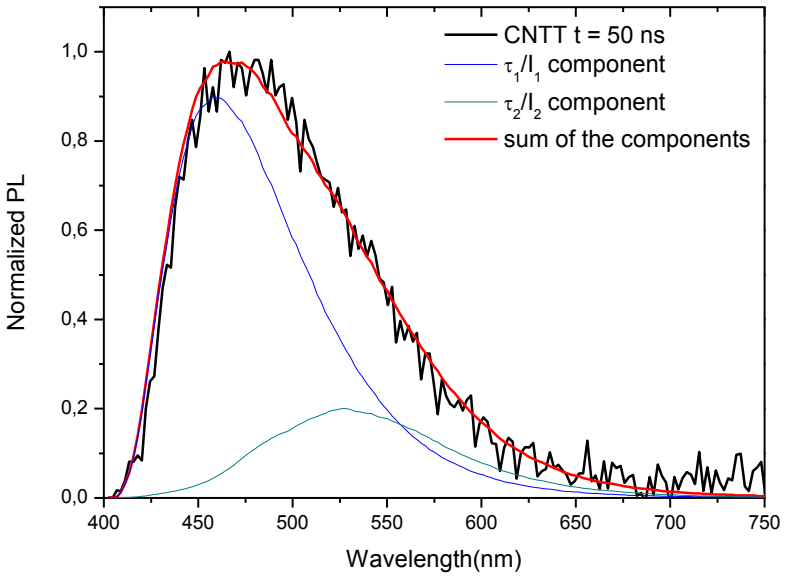

Figure 2.26: CNTT PL measured at t = 50 ns as sum of two components with lifetimes τ_1 and τ_2.

Figure 2.25 reports the PL spectra of CNTT and CNTT_300 at t = 0 ns and t = 50 ns after the laser pulse. CNTT shows an enlargement of about 30 nm after 50 ns with a maximum centered at λ_{em} = 475 nm. On the contrary, CNTT_300 maintains the PL profile unaltered in the whole range of investigation. The latter is in accord with almost single exponential description of PL time decay. As highlighted by Figure 2.26, CNTT photoluminescence can be recognized as the results of two components. The first one is peaked at λ_{em} = 460 nm and it corresponds to the PL recorded at time delay t = 0 ns in CNTT. The other components corresponds precisely to the emission of CNTT_300. The weights of the two emission are I_1 = 0.9 and I_2 = 0.1, very closed to the parameters reported in table 2.11.

In light of this, we can assert that the whole emission of CNTT involves two components with well-defined lifetimes and the heat treatment tends to enhance one contribution over the remaining one. To date, since the CNTT structure is a new molecular structure and, hence there are no data available on its structural and optical features, it is hard to find a strict correlation with the variation in the optical properties indiuced by thermal treatment. However, considering the preservation of the structure based on s-triazine core and –CN terminating group, we argue that, as previously discussed for the heptazine where is the larger linked units determines smaller S_0-S_1 absorption energy, the observed red shift is connected to an higher degree of linkage between the single CNTTT units upon thermal treatment. Among the evaluated triamino-s-triazine compounds, CNTT (with -CN termination) presents

outstanding thermal stability, up to 300 °C. The heat treatment promotes a significant tuning of optical properties, transforming the pristine powder with good UV absorption and emission in the blue region to a product with a symmetric emission centered in the green region displaying excitation spectrum in UV-blue interval. The optical redshift (PLE and PL) with the annealing temperature has been showed for heptazine systems at expense of the quantum yield. The introduction of cyanide functional group allow us to preserve the structural integrity of substituted triazine molecule and to overcome the tuning capacity without losing quantum efficiency.

2.4 Summary of Chapter 2

In this study, we pointed out the strict correlation between structural and optical properties in heptazine polymers. The experimental XRD data, Raman and optical properties spectra were analyzed and corroborated by the means of computational models, providing deep insight in the morphological behavior of the polymers as a function of the synthesis conditions.

As the synthesis temperature increases (from 300 °C to 600 °C in our experimental conditions) the three principal polymorphs of Carbon nitride (Melamine, Melem and PCN) were obtained. Through DFT calculations all the Raman modes of the three phases were assigned. Experimental data and calculation confirm that when passing from the lower temperature phases (Melamine and Melem, ob-tained at 300 °C and 400 °C respectively) to PCN structures (500 °C and above) a progressive redshift of the main optical features were observed. The PL redshift from Melem to Melamine is related to the triazines condensation and the formation of the larger aromatic units (s-triazine to heptazine). The in-creased interaction between tri-s-triazine units generates a further redshift in the PCN structure.

Further increasing of the annealing temperature does not produce significant variation on the maxi-mum of the excitation and emission spectra in sample with the PCN structures, but significant losses of quantum efficiency are revealed limiting the fluorescence tunability of tri-s-triazine polymer. A sys-tematic study of structural and optical properties of substituted-triazines showed the outstanding ther-mal stability of cyanide terminating compound. The latter displayed a symmetric emission centered in the green region with excitation spectrum in UV-blue interval, interesting characteristics for optoelectronic applications in the visible range.

2.5 References

[1] Bledowski, M.; Wang, L.; Ramakrishnan, A.; Khavryuchenko, O.V.; Khavryuchenko, V. D.; Ricci, P. C.; Strunk, J.; Cremer, T.; Kolbeck, C.; Beranek, R. , Phys. Chem. Chem. Phys, 13, 21511 (2011).
[2] A.Y. Liu, M.L. Cohen, Science, 245 841 (1989).
[3] E.G. Gillan, Chem. Mater. 12, 3906 (2000).
[4] J.H. Yang, X.T. Wu, X.F. Li, Y. Liu, M. Gao, X.Y. Liu, L.N. Kong, S.Y. Yang, Appl.Phys. A 105 161–166 (2011).
[5] B. Jürgens, E. Irran, J. Senker, P. Kroll, H. Müller, W. Schnick, J. Am. Chem. Soc.125 10288 (2003).
[6] T.Tyborski, C. Merchjann, S. Orthmann, F. Yang, M.-Ch Lux-Steiner, Th.Schedel-Niedrig J. Phys.: Condens. Matter 25,25, 395402. (2013).
[7] N. Kanagathara, N. Sivakumar, K. Gayathri, P. Krishnan, N. G. Renganathan, S. Gunasekaran, G. Anbalagan Proc Indian Natn Sci Acad 79 467 (2013).
[8] D. L. Yu , J. L. He , Z. Y. Liu , B. Xu D. C. Li , Y. J. Tian, J Mater Sci 43,689 (2008).
[9] H. M. Rietveld , Journal of Applied Crystallography 2, 65 (1969).
[10] Lutterotti, L.; Ceccato, R.; Dal Maschio, R.; Pagani, E. Mater. Sci. Forum, 278 (1998).
[11] Kroke, E.; Schwarz, M.; Horath-Bordon, E.; Kroll, P.; Noll, B.; Norman, A. D. New J. Chem., 26, 508, (2002).
[12] F.Fina, S. K. Callear, G. M. Carins, J.T.S. Irvine, Chem.Mater., 27, 2612, (2014).
[13] G. Algara-Siller, Nikolai Severin, Samantha Y. Chong, Torbjçrn Bjçrkman, R.G. Palgrave, A. Laybourn, M. Antonietti, Y. Z. Khimyak, A. V. Krasheninnikov, J. P. Rabe, U. Kaiser, A. I. Cooper,A. Thomas, M. J. Bojdys Angew. Chem. Int. Ed. 53, 7450 , (2014).
[14] J. Zhu, P. Xiao, H.Li, S.A.C. Carabineiro ACS Appl. Mater. Inter., 6, 16449 (2014).
[15] Z- Zhao, Y. Sun, F. Dong, Nanoscale., 7, 15 (2015).
[16] C.Merschjann, T. Tyborski, S. Orthmann, F. Yang, K. Schwarzburg, M. Lublow, M.-Ch Lux-Steiner,Th.Schedel-Niedrig, Phys. Rev. B,87, 205204 (2013).
[17] H. Haken, H.C. Wolf. Molecular Physics and Elements of Quantum Chemistry. Springer, (1995).
[18] Y. Zhang, Q. Pan, G. Chai, M. Liang, G. Dong, Q. Zhang, J. Qiu, Sci. Rep., 3, 1 (2002).
[19] G. Dong, Y. Zhang, Q. Pan, J. Qiu, J. Photochem. Photobio. C ,20, 33-35, (2014).
[20] Gaussian 09, Revision **D.01**, M. J. Frisch, G. W. Trucks, H. B. Schlegel, G. E. Scuseria, M. A. Robb, J. R. Cheeseman, G. Scalmani, V. Barone, B. Mennucci, G. A. Petersson, H. Nakatsuji, M. Caricato, X. Li, H. P. Hratchian, A. F. Izmaylov, J. Bloino, G. Zheng, J. L. Sonnenberg, M. Hada, M. Ehara, K. Toyota, R. Fukuda, J. Hasegawa, M. Ishida, T. Nakajima, Y. Honda, O. Kitao, H. Nakai, T. Vreven, J. A. Montgomery, Jr., J. E. Peralta, F. Ogliaro, M. Bearpark, J. J. Heyd, E. Brothers, K. N. Kudin, V. N. Staroverov, R. Kobayashi, J. Normand, K. Raghavachari, A. Rendell, J. C. Burant, S. S. Iyengar, J. Tomasi, M. Cossi, N. Rega, J. M. Millam, M. Klene, J. E. Knox, J. B. Cross, V. Bakken, C. Adamo, J. Jaramillo, R. Gomperts, R. E. Stratmann, O. Yazyev, A. J. Austin, R. Cammi, C. Pomelli, J. W. Ochterski, R. L. Martin, K. Morokuma, V. G. Zakrzewski, G. A. Voth, P. Salvador, J. J. Dannenberg, S. Dapprich, A. D. Daniels, Ö. Farkas, J. B. Foresman, J. V. Ortiz, J. Cioslowski, and D. J. Fox, Gaussian, Inc., Wallingford CT, (2009).
[21] A. D. Becke, J. Chem. Phys., 98, 5648, (1993).
[22] C. Lee, W. Yang and R. G. Parr, Phys. Rev. B: Condens. Matter Mater. Phys., 37, 785, (1988).
[23] M. Prabhaharan, A. R. Prabhaharan, S. Gunasekaran, and S. Srinivasan, Spectrochim. Acta Part A 123, 392 (2014).
[24] Y. Yuan, L. Zhang, J. Xing, M. I. B.Utama , X. Lu, K. Du, Y. Li, X. Hu, S. Wang, A. Genç, R. Dunin-Borkowski, J. Arbiold,Q. Xiong, Nanoscale, 7, 12343, (2015).
[25] A.R. Katritzky. Physical Methods in Heterocyclic Chemistry. Vol.6. Academic Press. (1974).
[26] J. N. Murrell, Theory of the Electronic Spectra of Organic Molecules. Methuen,London, (1963).
[27] M. Fox, Chem. Rev., 92,365-368 (1992).
[28] Balaganesan B, Wen S, Chen C, Tetrahedron Lett, 44,145-147 (2003).
[29] Yu G, Gao J, Hummelen J, Wudl F, Heeger A, Science, 270:1789-1791 (1995).
[30] N. B. Colthup, L. H. Daly. Introduction to Infrared and Raman Spectroscopy. Academic Press. (1975).
[31] M.Alcolea Palafox, V.K.Rastogi, J.K.Vats. J. Raman Spect,37,85-99, (2006).
[32] Nielsen OF, Christensen DH, Fajolles C. J. Mol. Liq.; 45,77, (1989).
[33] Prasad JP, Rai SB, Thakur SN. Chem. Phys. Lett.; 164: 629,(1989).
[34] Higgins J, Zhou XF, Liu RF. Spectrochim. Acta; 53A: 721 (1997).
[35] Sinha SP, Chatterjee CL. Indian J. Pure Appl. Phys.; 14, 41(1976).
[36] M. Miyazaki, T. Nakamura, M. Wohlgemuth R. Mitric´,O. Dopfer, M. Fujii. Phys. Chem. Chem. Phys., 29969-29977 (2015).
[37] O. Kwon, S. Barlow, S. A. Odom, L. Beverina, N. J. Thompson, E. Zojer, J. Bredas,S. R. Marder; J. Phys. Chem. A, 109, 9346-9352 (2005).
[38] D. P. M. Huang,J. Berthelin, J-M Bollag,W. B. McGil . Environmental Impacts of Soil Component Interactions. Vol 1 CRC, (1995).

Chapter 3

Carbon Nitride / Metal Oxides Hybrids

3.1 Rare Earth Energy Transfer Mechanism and Melamine-Y_2O_3:Tb^{3+} Nanohybrids

3.1.1 Introduction

In the ambit of application of Rare Earth doping ions in organic and inorganic matrix, the energy transfer processes occurring between optically active centres or between optically active centres and defects of the host, cover great importance since they can inhibit or enhance the luminescence properties of the material [1]. In general, an increase in concentration of RE ions does not produce a linear response in emission intensity and the material can undergo to a quenching of the luminescence above a critical concentration [1], when an efficient energy transfer among optical active centres, statistically closer with the increase of concentration, is established. However, another mechanism of energy transfer is determined in concentration quenching regime, namely the interaction between RE ions and defects of the host, in which part of the energy is transferred to lattice defects and impurities [1],[2].

The first part of the following section is dedicated to the study of energy transfer mechanism by the means of time-resolved photoluminescence technique, taking into account the exemplar case of Ce and Tb co-doped Y_2SiO_5. This host presents outstanding luminescent performances and the interaction between the two kind of active ions tends to assume a general behaviour, with no significant influence by the matrix.

In the second part of the following section, it is discussed the energy transfer mechanism in melamine – Y_2O_3: Tb^{3+} nanohybrids, in which the RE-doped inorganic matrix interaction with the organic molecule promotes an efficient luminescence enhancement.

3.1.2 Energy transfer mechanism among rare earth ions

In recent years, considerable efforts were dedicated to the research of luminescent nanoparticles for the development of new phosphors in LED and displays, such as plasma panels, field-emission displays, electroluminescent panels, and scintillator panels for X-ray radiography. In order to achieve devices

with high resolution, high brightness, and long operating time, researchers have extensively investigated various inorganic luminescent materials and, in this framework, rare earth (RE)-doped nanoscaled samples have attracted most of the studies [1]-[8].

Different crystal hosts were examined with excellent results, such as alkali earth orthophosphates,[9]aluminum garnet ($Y_3Al_5O_{12}$)[10] and Re-doped oxyorthosilicates (RE_2SiO_5), mainly doped with Eu^{3+}, Ce^{3+}, Sm^{3+}, and/or Tb^{3+}[11],[12]. Among the others, Tb and Ce co-doped yttrium oxyorthosilicates show interesting and promising properties related to the combined chemical-physical characteristics of the matrix and the emission properties of the doping element. In particular, Y_2SiO_5 (YSO) crystal presents high chemical and thermal stability and elevated mass absorption coefficient with high stopping power, and it is already applied as excellent host material for cathodoluminescent phosphors [13].

Recently, the tunability properties of Re emission in this host, which is due to different co-doping amount [4], suggested YSO nanoparticles as good candidate as phosphors in White LED (WLED) devices, especially in substitution of actual phosphors, taking advantage by the energy transfer process among rare earths (Ce – Tb – Eu)[4].

All of the applications where RE doping elements are present require a deep understanding of the properties on the interaction among dopant ions.

3.1.2.1 Experimental details

Samples containing different amounts of terbium (from 0.1 up to 10 % at.) with fixed cerium concentration (1% at.) were prepared through an aqueous sol–gel route. Yttrium nitrate hexahydrate ($Y(NO_3)_3 \cdot 6H_2O$, Aldrich, 99.9%), terbium nitrate pentahydrate ($Tb(NO_3)_3 \cdot 5H_2O$, Aldrich, 99.9%), cerium nitrate hexahydrate ($Ce(NO_3)_3 \cdot 6H_2O$, Aldrich 99.9%), tetraethoxysilane (TEOS, Aldrich, 98%) and absolute ethanol (Carlo Erba, 99.8%) were used as reactants for the preparation. To this end, aqueous solutions containing appropriate concentrations of yttrium and terbium nitrates were mixed with an ethanolic solution of TEOS and acidified with nitric acid (pH=1). The resulting transparent sols were stirred for 180 min at room temperature and then allowed to gel at 50 °C for three days. The prepared gels were successively powdered in an agate mortar and gradually thermally treated (4 °C min^{-1}) up to 1250 °C, leaving the samples at this final temperature for 4 h.

Photoluminescence (PL) measurements were performed with excitation provided by an optical parametric oscillator with a frequency doubler device (Spectra Physics MOPO), excited by the third harmonic of a pulsed Nd-YAG laser (Spectra Physics QuantaRay PRO-270), with a pulse width at half maximum of 10 ns and a 10 Hz repetition rate. PL measurements were performed in a 90° geometry by focusing the PL signal onto the entrance slit of a monochromator (ARC Spectra Pro 300i) with a spectral bandwidth of 2 nm. The PL signal was detected with a gatable intensified CCD (Princeton Instruments PI-MAX). Depending on PL bands under examination, different delays from excitation pulse and time gates were used. The temporal response of the detection system was measured.

The Raman spectra were detected in backscattering geometry by using the 633 nm line of a He/Ne ion laser. Raman spectra were performed in air at room temperature with a triple spectrometer Jobin-Yvon Dilor integrated system with a spectral resolution of about 1 cm^{-1}. Spectra were recorded in the Stokes region by a 1200 grooves/mm grating monochromator and a liquid N2-cooled CCD detector system (Sprectrum-one). The reported Tb and Ce concentrations are referred to as atomic percentages. X-ray powder diffraction patterns were performed by using a θ-θ diffractometer (Seifert X3000) with Bragg-Brentano geometry and Cu Kα radiation. The samples were grinded with agate mortar and the obtained fine powders were deposited over a silicon zero background sample holder.

3.1.2.2 Results and discussion

Mainly depending on the ionic radius of the rare earth element (RE^{3+}), RE_2SiO_5 compounds crystallize in two monoclinic polymorphs. When the RE ion ranges along the lanthanide series from La to Gd, the crystals belong to the $P2_1/c$ space group, called the X1 phase, while the crystal structure belongs to the C2/c space group (X2 phase) when RE ions range from Dy to Lu [1],[5]. The oxyorthosilicates of Tb, Ce and Y can crystallize in both the X1 and X2 phases, depending on the crystallization temperature: the former (X1) is the low temperature phase, whereas the X2 phase is the high temperature one. In particular, when Yttrium occupies the crystallographic sites of the main RE (YSO), the transition between the two phases takes place at about 1190 °C. Taking into account the final temperature of the synthesis (1250 °C), one should expect that Tb and Ce doping of YSO crystal could induce in the crystal lattice local distortions or phase transitions, even though Y^{3+} and Tb^{3+} have very close values of ionic radius (880 and 920 pm, respectively, in 7-fold coordinated sites)[14]. In this framework, a key factor

to achieve elevated doping concentration in stable and homogeneous crystals is to assess the concentration range where the doping elements (Tb and Ce) do not induce a variation of the space group. For this reason, we first checked the effective phase of the samples as a function of Tb concentration. Figure 3.1A reports the Raman spectra in the Tb concentration range: 0.1% and 10%.

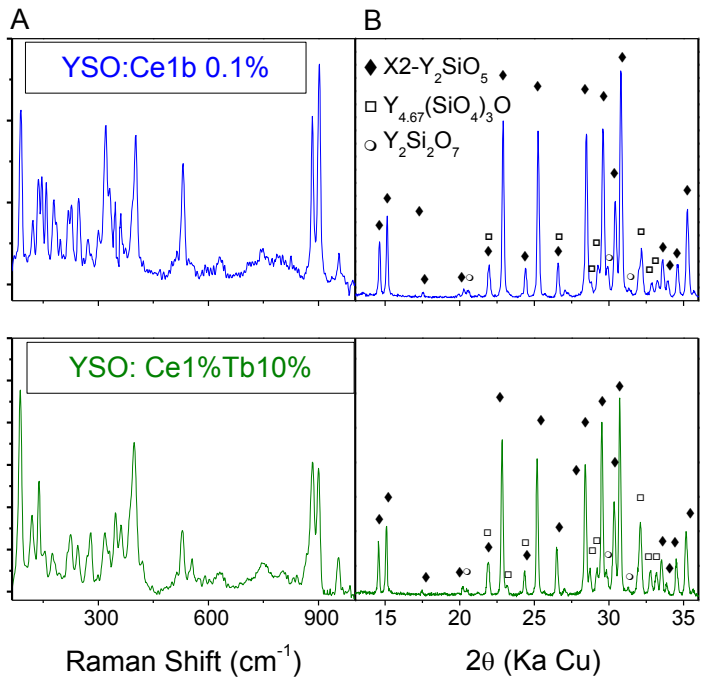

Figure 3.1: Raman spectra (A) and XRD (B) spectra for Tb:Ce:YSO samples: Tb concentration at 0.1% and 10% at., Ce concentration fixed at 1% at.

As shown in the Raman spectra, the presence of the bands at 880 cm^{-1} and 910 cm^{-1} indicates that the samples are grown in the X2 phase [15]. The crystal structure is confirmed by the XRD reported in Figure 3.1B. However, further peaks are observed (main peak at 2θ =32°) and can be ascribed to the highest reflections of an hexagonal phase of yttrium oxide silicate (apatite type) $Y_{4.67}(SiO_4)_3O$ (PDF Card No. 30-1457). A very small amount of yttrium disilicate α-$Y_2Si_2O_7$ (PDF Card No. 38-223) is also present. Although the presence of traces of impurity phases, the optical properties of the synthetized samples resemble the PL spectra of pure monocrystalline samples [15],[17].

The emission properties of Tb, Ce co-doped YSO samples were analysed as a function of the Tb doping concentration. Figure 3.2 reports the emission spectra under 250 nm excitation light, for the Tb doped samples concentration in the 0.1 to 10% range and fixed concentration of Ce (1% at.). PL

spectra show a structured emission in the 350-600 nm range whose relative intensity depends on the RE doping concentration.

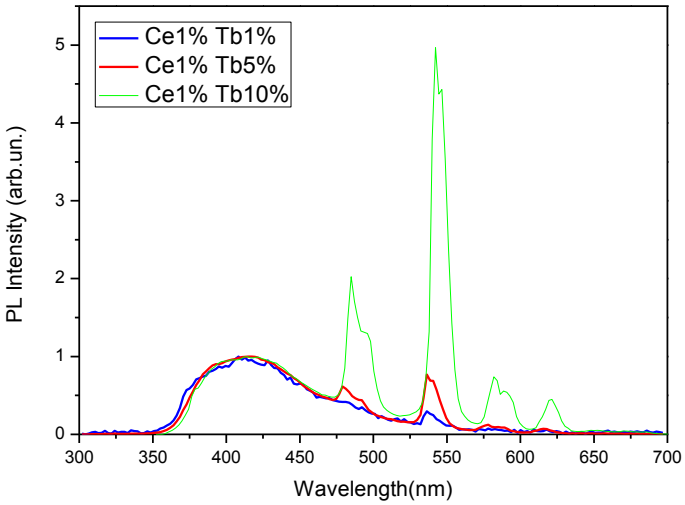

Figure 3.2: Emission spectra under 250 nm excitation light in Tb:Ce:YSO samples, Tb concentration between 0.1 and 10% at. range (1% at. Ce concentration).

The main peaks of the recorded emission spectrum are centered at 400 nm (a broad band due to Ce emission)[18][19] and at 475, 488, 499, 545, 585, 592, and 622 nm, narrower peaks due to Tb emission[20]. The Tb^{3+} luminescence is due to transitions from the crystal-field levels of two metastable multiplets, $^5D_3$ and $5D_4$, down to the crystal-field levels of the ^7F_J multiplets (with J = 3, 4, 5, 6). The $^5D_3$ and $^5D_4$ emissions are located in two distinct spectral regions, with a significant overlapping between the $^5D_3 \rightarrow {}^7F_2$ and $^5D_4 \rightarrow {}^7F_6$ transitions in the 450-500 spectral range [1],[5]. However, due to the high efficient cross relaxation process from $^5D_3$ to $^5D_4$ levels also at relatively low doping percentage, the transitions $^5D_3 \rightarrow {}^7F_J$ are very low in intensity, overlapped by the Cerium emission.

The emission spectra, normalized to the maximum of Ce emission, show a non-linear trend of the Tb emission intensity as a function of Tb concentration. This trend suggests the presence of energy transfer phenomena related to dopants ions: Tb-Tb interactions and Ce-Tb interactions. The former was already studied in sol–gel synthesized terbium doped Y_2SiO_5 phosphor particles with different Tb concentration (from 0.001% to 10%), where the luminescence profile changes from a blue to a green peaked

emission spectrum by increasing the dopant concentration because of the energy transfer among Tb centers[5]. The inter-centres' energy transfer mechanism is well accounted for by the Inokuti–Hirayama (IH) kinetic model which is based on a statistical average of inter-centres distance, dependent on decay channels of the donor luminescence. The distribution of the decay modes is explained by means of Forster–Dexter resonance theory that assumes a constant rate constant for the energy transfer by multi-polar interactions between donors and acceptors.

Two regimes of energy transfer among RE ions have been observed, dependent on the concentration of acceptor ion.

3.1.2.3 Ions interactions at low-middle concentrations of Tb (0.1%-10% at.)

Ions interaction can be investigated by time-resolved PL technique. In this context, we applied gated (see Appendix 1) technique, showing different spectral features according to the choice of experimental parameters (*gate* and *time delay*).

Figure 3.3 shows the luminescence spectrum of Tb ions, at different concentrations, collected with a pulse delay of 100 ns, once the emissions of Ce ions are already extinguished (Ce emissions are in the ns range). At the largest concentrations (5 and 10% of Tb ions) smaller delays were applied because of the shortening of Tb emissions decay time (see discussion below).

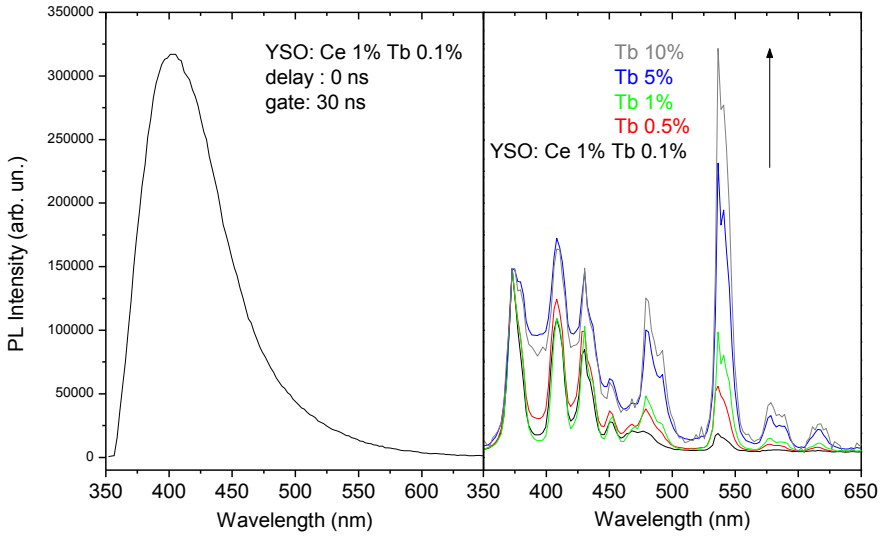

Figure 3.3: Luminescence spectrum of Ce, Tb : YSO samples, with different Tb concentrations. Left: Ce emission recorded with gate: 30 ns and delay : 0 ns. Right : Tb emission recorded with variable gate and delay: 100 ns.

According to the literature [5], the peaks shown at about 380, 416, 438, and 459 nm are related to the transitions from the Tb $^5D_3$ level. It is worth to point out that the recombinations from the $^5D_3$ levels are visible at high Tb concentrations thanks to the time windows of hundreds of microseconds. The energy scheme of the recombination at the Cerium and Terbium sites in the YSO matrix is reported in Figure 3.4 while the photoluminescence spectrum in steady time conditions in Tb:Ce:YSO and Tb:YSO samples are well documented in literature [4],[5].

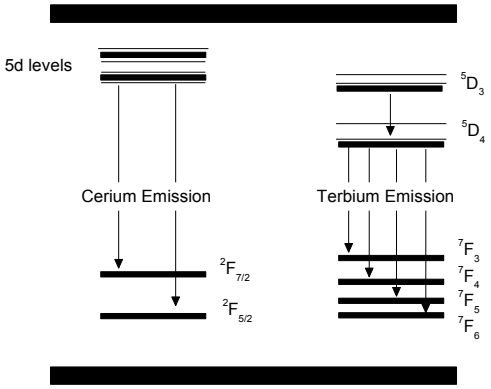

Figure 3.4: Energy levels scheme for Ce^{3+} and Tb^{3+}.

As expected, at the reported lowest Tb concentration (0.1% in Figure 3.3) the blue emissions are the most intense ones with respect to the green ones, in agreement with previous reports.

Figure 3.5 reports the decay time of the 375 nm emission of Tb ions as a function of the concentration.

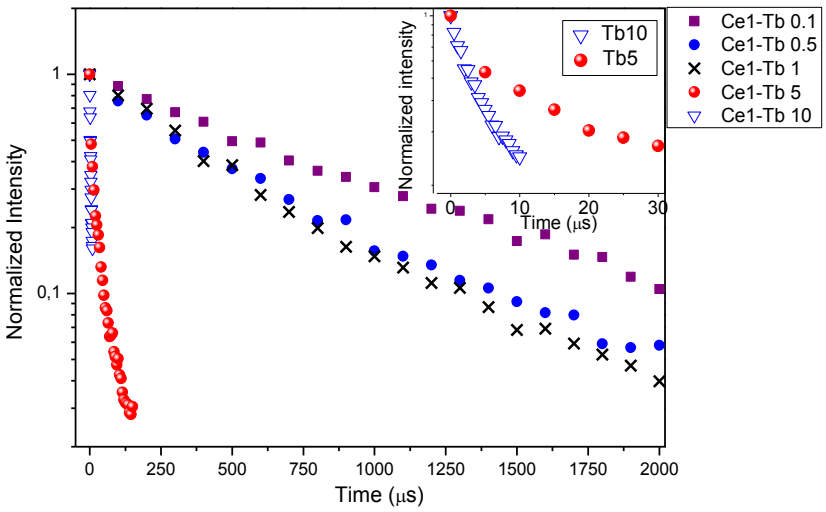

Figure 3.5: Decay time at 375 nm emission in Ce,Tb :YSO samples as a function of the Tb concentration.

The luminescence decay curve can be well fitted with a bi-exponential function by the use of the following equation

$$I(t) = A_1 \exp\left(-\frac{t}{\tau_1}\right) + A_2 \exp\left(-\frac{t}{\tau_2}\right) \quad (3.1)$$

where τ_1 and τ_2 are the decay times for the exponential components. Table 1 reports the results of the fit, with relative weight, τ_1 and τ_2 at different concentrations and decay time of Tb ions in YSO.

Table 3.1: Fit results of the λ_{em} = 375 nm Tb emission according to equation 3.1.

Sample	A_1	A_2	A_1/A_2	τ_1 (μs)	τ_2 (μs)
Ce1Tb 0.1	63290	42908	1,475016	1250	433
Ce1Tb 0.5	99234	273587	0,362715	1220	433
Ce1Tb 1	12224	85684	0,142664	1180	417
Ce1Tb 5	10444	135303	0.077189	1260	22
Ce1Tb10	891	37462	0.0237	1240	1.5

As evidenced in Table 3.1, the two decay times display different trends with respect to the case with no Ce ions: τ_1 decay time is slow and it is not dependent on Tb concentration, whereas τ_2 decay time is fast and depends on the concentration.

The two decays could be assigned to two different phenomena: the former, especially at low concentrations (< 1%), could be explained by hypothesizing that at least a part of Tb ions decays as "free" even in the presence of Cerium in the lattice. The latter depends on the presence of Ce ions and it suggests an energy transfer from Tb to Ce ions: indeed the decrease of the decay time as a function of Tb concentration is larger than the ones recorded in absence of Ce [5].

As the concentration of Tb ions increases (> 1%), this transfer mechanism should compete with the previously reported interactions among Tb ions[4],[7]. This hypothesis is indeed confirmed by the analysis of the weights associated to each decay time as a function of the concentration: at low concentration the τ_1 decay prevails, whereas at high concentration the larger relative contribution of τ_2 causes a faster overall decay.

As previously reported [1], the kinetic model can be obtained by solving the equation

$$\frac{dn_1(t)}{dt} = -\left[\gamma_1 + A_I + \frac{dF(t)}{dt}\right] n_1(t) \rightarrow n_1(t) = n_{10} \exp\left[-\left(\gamma_1 + A_I\right)t - F(t)\right] \quad (3.2)$$

where $n_1(t)$ is the concentration of excited centres in the D_3 level, γ_1 is the probability factor of radiative decay for a specific transition, A_I is the probability factor for the internal energy transfer.

F(t) is the time-dependent probability factor for the energy transfer which can be defined according to the following expression:

$$F(t) = \sqrt{\pi}\frac{c}{c_0}\sqrt{\gamma_1 t} = k\sqrt{t} \tag{3.3}$$

where c is the nominal concentration, c_0 is the Tb critical concentration at which the Tb inter-center transfer mechanism starts and γ_1 refers to the specific transition (in this case $\gamma_1 = 767\ s^{-1}$)[5],[7].

By using the HI model for dipole-dipole interactions[21] , it is possible to calculate the rate constant *k* and the c/c_0 ratio as reported in Table 3.2 at different Tb concentrations (Ce concentration 1% at). Data calculated in samples with no Ce ions are reported for comparison.

The fitting results refer to the experimental luminescence decays $^5D_3 \rightarrow {}^7F_J$ reported in Figure 3.6, where k was assumed as a concentration related free parameter according to the following equation:

$$\left[\ln\left(\frac{I}{I_0}\right) + (\gamma_1 + A_I)t\right]^2 = k^2 t \tag{3.4}$$

Table 3.2: *k* constant calculated at different Tb concentration.

Tb conc. (%) Ce 1%	0.1	0.5	1	5	10
k ($s^{-1/2}$)	14	32.24	36.9	149	364
c/c_0	0.285	0.65	0.752	3.036	7.429

Tb conc. (%)	0.2	1	10
k ($s^{-1/2}$)	7.9	38.3	364
c/c0	0.161	0.782	7.429

The calculated values show that at low Tb concentration the ratio c/c_0 is larger than the same term calculated in absence of Ce. This result implies that the presence of Ce reduces the Tb critical concentration c_0.

In order to verify this conclusion we analysed the decay time of Ce emissions as function of Tb concentration. Figure 3.7 reports the decay time of the 393 nm emission of Ce ions as a function of the Tb concentration, the luminescence decay curves being successfully fitted with a single exponential decay:

$$I(t) = A_1 exp\left(-\frac{t}{\tau_{Ce}}\right) \quad (5)$$

where I represents the luminescence intensity and A_1 is a constant; t is the time and τ_{Ce} is the decay time. Results are reported in the Table 3.3 and plotted in the inset of Figure 3.7. To the reported data we added in the plot the average decay time (see details below) estimated for the case of largest Tb concentration (25%). The transfer process from Ce to Tb (refer to the energy scheme in fig. 3.4) is testified by the decrease of the Ce lifetime with respect to the reference sample with no Tb atoms. The obtained data show that the energy transfer is retrieved down to the lowest concentrations investigated, being clearly evident above 1% Tb concentration, in good agreement with Zhang *et al* [4].

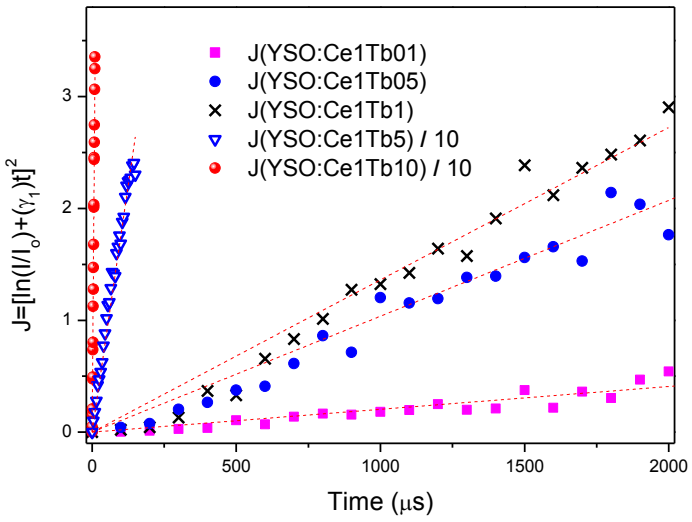

Figure 3.6: Decay Time at 375 nm emission in Ce,Tb:YSO samples as a function of the Tb concentration assuming the Inokuti-Hirayama model for dipole-dipole interactions.

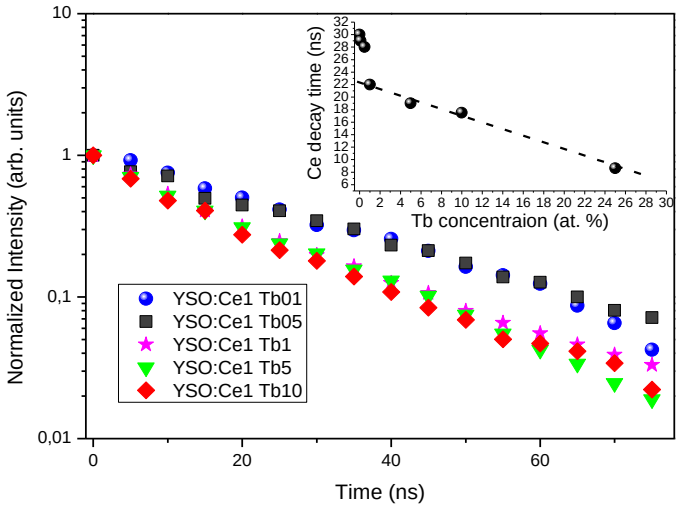

Figure 3.7: Decay time of the 393 nm emission from Ce ions as a function of the Tb concentration. Inset: Ce decay time at different Tb concentration (see Table 3.3).

Table 3.3: Decay time of the 393 nm emission from Ce ions as a function of the Tb concentration.

Sample	τ_{Ce} (ns)
Ce1	30
Ce 1 Tb 0.1	29
Ce 1 Tb 0.5	28
Ce 1 Tb 1.0	22
Ce 1 Tb 5.0	19
Ce 1 Tb 10.0	17.5

However, we should point out that the decrease of the decay time at the lowest Tb concentrations (0.1 and 0.5%) is almost negligible. If we consider the reduced critical concentration of Tb in presence of Ce and the almost constant decay time of the latter at the lowest Tb concentration, we can infer that in this range, i.e. below the Tb concentration of 1%, a reverse transfer mechanism is observed: the $^5D_3$ emitting Tb ions act as sensitizer for the Ce ones which in turn transfer to $^5D_4$ emitting Tb centers. The decay curves of Ce emission confirm the results reported above since in the low-middle Tb concentration there

is an energy transfer from Tb ions to Ce ones the Tb critical concentration is lower than in the samples without co-doping.

3.1.2.4 Ions interactions at middle - high concentrations of Tb (1%-25% at.)

To better understand the energy transfer process among the activator and sensitizer ions at middle-high concentration, when there is an overlapping among the wavefunctions related to each ion, the Forster-Dexter model could be used [22],[23]. In this case the activator is the Tb ions while Ce ions act as sensitizer for the emission at 545 nm from Tb. The energy transfer probability via multipolar interaction can be described by the following equation[4], [24]

$$P(R) \propto \frac{Q_A}{R^b \tau_D} \int \frac{f_D(E) F_A(E)}{E^C} dE \tag{3.6}$$

where *P* is the energy-transfer probability, τ_D the decay time of donor emission, Q_A the total absorption cross-section of acceptor, and R the distance between donor and acceptor; *b* and *c* are parameters depending on the type of energy transfer.

As indicated in the equation (3.6), the energy-transfer probability P is inversely proportional to decay time τ_D, showing that the luminescence lifetime of a sensitizer is reduced in the case of energy transfer because of the presence of additional decay channels. According to Dexter's energy-transfer formula of multipolar interaction, by using the Reisfeld approximation [6],[25],[26]the following relation can be obtained :

$$\frac{\tau_{S_0}}{\tau_S} \propto C^{\frac{a}{3}} \tag{3.7}$$

where C is the concentration of Tb^{3+}, and a = 3, 6, 8, or 10 for exchange interaction, dipole−dipole, dipole−quadrupole, or quadrupole−quadrupole interactions, respectively.

Plots of τ_0/τ versus $C^{a/3}$ based on the above equation are shown in Figure 3.8. According to Zhang *et al*[4] to estimate the ratio τ_0/τ , the average decay time τ^* has been calculated to account for the decay of the overall emission:

$$\tau^* = \frac{\int tI(t)dt}{\int I(t)dt} \tag{3.8}$$

As shown in the Figure 3.8, the best linear trend is observed when a is equal to 8, indicating that energy transfer from Ce^{3+} to Tb^{3+} took place via the dipole−quadrupole mechanism. This is indeed well confirmed by the estimation of the distance R between Ce and Tb ions,2 which is larger than 5 Å, indicating an electric multipole interaction, but for the 25% Tb concentration.

A final comment pertains the chosen Ce concentration: it is well known that at large Ce concentration both the substitutional sites of Y^{3+} are occupied by Ce ions and that two different emissions can be detected, at 400 (Ce1) and 450 (Ce2) nm [27]. However at the applied experimental excitation wavelength (250 nm) the Ce2 site is not excited, so that the recorded emission is ascribed to the Ce1. In addition we were interested in the energy transfer mechanism between Ce and Tb ions, and by estimating the average decay time (eq. 3.8) we accounted for the overall emission, no matter which is the emitting Ce site.

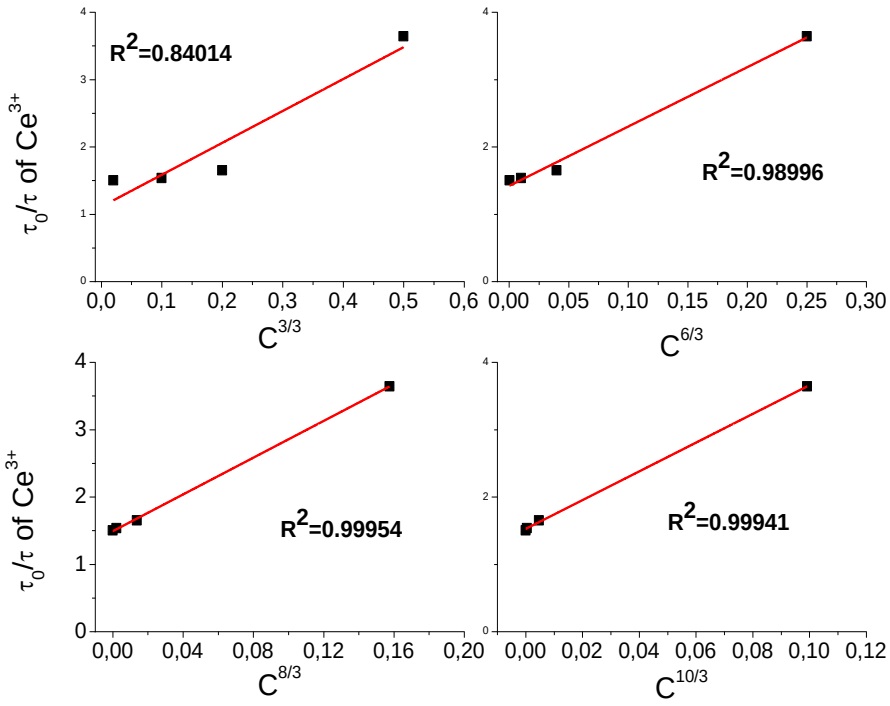

Figure 3.8: Dependence of the 393 nm Ce emission (τ_0 / τ) on $C^{a/3}$ (a=3, 6 8, 10) for different concentration of Tb ions.

3.1.3 Luminescence Enhancement by Energy Transfer in Melamine-Y_2O_3:Tb^{3+} Nanohybrids

Yttrium oxide (Y_2O_3) has attracted much attention for its potential applications as a chemically and thermally stable host matrix [28]. Among its remarkable properties, it presents a high melting point of 2450 °C, high density (5.03 g cm^{-3}) and good thermal conductivity (33 Wm^{-1} k^{-1})[29]. Furthermore, yttria based material can be adopted for photonic waveguide applications thanks to their high transmittance ranging from 280 nm to 8 μm and a refractive index of 2 [30].

Yttria energy gap of 5.5 eV favours a successful doping with several tripositive RE ions covering a wide range from blue to NIR. When doped with Eu^{3+}, it exhibits a red emission with a quantum yield of 92 % for a bulk system (particles of ~5 μm in size). The problem of quantum efficiency in RE doped Y_2O_3 at nanoscale has been addressed in several works, sometimes with controversial conclusions. In general, a reduction of QY is observed with decreasing size of nanoparticles depending on synthesis method and lowering of crystallinity[31],[33].

Tb^{3+} ions has been considered as good candidate to cover the green region instead of Er^{3+} and a codoping with Yb^{3+} is frequently evaluated for upconversion applications[34]. Moreover, it has been showed a good efficient codoping-free upconversion process when irradiated with femtosecond sources [35]. However, the reduced PL quantum efficiency and, mainly, the deep UV excitation spectrum has strongly inhibited its use in Y_2O_3 doped crystal.

At nanoscale RE ions in oxide matrix rarely present a high quantum yield because of the high rate of non-radiative recombinations, caused by the defects at surfaces and the presence of OH^- groups, mainly detrimental for IR emission [32]. Most recently it was proposed to apply the synthesis strategy adopted for organic-RE complex in the field of nanostructured systems with encouraging results[36]. This approach consists in improving the luminescence of Rare Eearth metals by organic ligands at the surfaces. This effect is known as “antenna effect” arising when light is strongly absorbed by organic ligand and much of the energy is then transferred to RE ions that emit efficiently[37]. Thanks to organic molecule, the obtained system can provide a good optical absorption even in region out of RE absorption resonance [38].

In paragraph, we synthesized $Y_2O_3:Tb^{3+}$ nanostructures by hydrothermal method. Yttrium Hydroxides precursors are firstly obtained and then a thermal treatment at high temperature yields the oxide nanocrystals. $Y_2O_3:Tb^{3+}$ were functionalised with 2,4,6-triamino-s-trazine (melamine) by thermal vapour method. Melamine ($C_3H_6N_6$) is known to have a strong absorption in UV region well matching with Tb^{3+} ions absorption in several inorganic matrix. It also presents elevate thermal stability resulting a good candidate for high temperature synthesis methods. $Y_2O_3:Tb^{3+}$ pristine nanostructures (YTb) and their melamine- $Y_2O_3:Tb^{3+}$ (MeYTb) counterparts were analysed by steady state (SSPL) and time resolved photoluminescence (TRPL) to investigate the effect of organic presence at the surfaces and the mechanism behind the origin of Tb^{3+} luminescence increase. The hybrid compound presents greatly enhanced luminescence for the green emission from Tb^{3+} ions with excitation spectrum shifted trough the lower energy suggesting its potential application as phosphor in solid state lighting devices.

3.1.3.1 Experimental details

All chemicals were purchased from Sigma-Aldrich and used without further purification. Y_2O_3 nanostructures (NS) were synthesized by surfactant tailored hydrothermal method. In a typical synthesis 1 g di $Y(NO_3)_3*6H_2O$ and 0,02 g of $Tb(NO_3)_3*5H_2O$ were dissolved in 10 ml of distilled water. Then, 0.5 ml of Diethanolamine (DEA) was added to the aqueous solution under vigorous stirring for 10 min. The solution was corrected at pH=10 by means of a 10 M NaOH solution. The colloidal solution was transferred in a 50 ml Teflon-lined autoclave and hydrothermally treated at 180°C for 24 h. After air quenching, the precipitate was washed with distilled water and dried at 60 °C in air for an hour. The hydroxide NS were calcinated at 600 °C for 3 h in air with a rate of 5°C/min.

$C_3H_6N_6$ coated Y_2O_3 NS were prepared by thermal vapour deposition route. A certain amount of Melamine powder was put in an alumina crucible and Yttria NS were deposited on a silicon substrate at a distance of about 10 cm, placed in a quartz tube accommodated in tubular furnace and treated at 500 °C for 2h with 5°C/min ramp under nitrogen flux (30 ml/min). Several samples with different melamine and $Y_2O_3:Tb^{3+}$ molar ratio (n_{Me} / n_{YTb}) were synthesized in order to show dependence of luminescence enhancement on the organic concentration.

The crystal structure of $Y_2O_3:Tb^{3+}$ samples was probed using X-ray diffraction patterns recorded by a Seifert X3000 diffractometer with a θ−θ Bragg−Brentano geometry with Cu-Kα wavelength. High resolution transmission electron microscopy (HRTEM) images were obtained by means of a JEM 2010 UHR equipped with a Gatan Imaging Filter (GIF) with a 15 eV window and a 794 slow scan CCD camera. The samples were dispersed in n-octane and submitted to an ultrasonic bath. Then, the suspensions were dropped on a copper grid covered with a carbon thin film for the observation.

In order to obtain information on the surface state of hybrid MeYTb samples Raman spectra were acquired. Raman scattering measurements were performed in backscattering geometry at room temperature with a compact BWTEK i-Raman EX integrated system (spectral resolution of about 9 cm^{-1}) equipped with a microscopy system. The powders were irradiated with the 1064 nm line of a Nd:YAG laser.

For SSPL and PLE measurements was used the filtered light from a laser driven Xenon lamp (EQ-99-X) with a final bandwidth of about 1 nm.

Time-resolved photoluminescence measurements (TRPL) were performed using an optical parametric oscillator with a frequency doubler device, pumped by the third harmonic (355 nm) of a pulsed Nd:YAG laser (Quanta-Ray Pro 730). The excitation pulse width at half-maximum was 8 ns with 10 Hz of repetition rate, and spectral bandwidth less than 0.3 cm^{-1}. The PL signal was dispersed by a spectrograph (ARC-SpectraPro 300i) with a spectral bandpass <2.5 nm and detected by a gateable intensified CCD (PI MAX Princeton Inst.).

3.1.3.2 Results and discussion

Figure 3.9 reports the representative XRD pattern of the hydrothermal synthesized samples, annealed at the temperature of 600 °C, acquired in the Bragg angles range $16° \leq 2\theta \leq 65°$. As prepared samples show a sequence of broadened reflections assignable to the nanostructured cubic bixbyite-like phase with peaks indexed by PDF-Card 83-0927. No other phases were detected and all diffraction peaks are attributed to *Ia-3* space group (No. 206) with no deviation caused by impurity elements from the pure phase. The related crystal parameters are shown in Table 3.4. It is worth to note the large value of the

strain parameter, determined by the relation $\varepsilon = \beta\cos\theta/4$, especially when compared with the ones previously reported on 40÷60 nm nanoparticles[39]. This result can be reasonably assigned to an increase of atomic displacements in correspondence of grain boundary, frequently observed in small oxide nanosystems or in particles with highly porous surfaces [40].

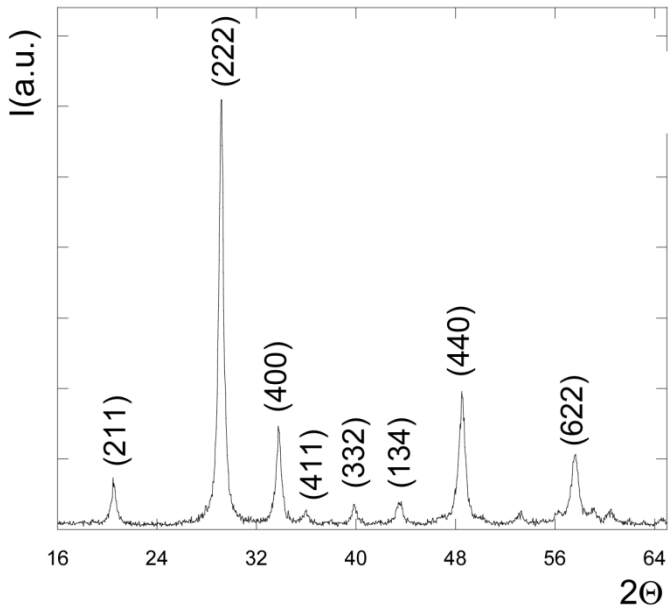

Figure 3.9 : XRD pattern for Y_2O_3:Tb^{3+} sample.

Table 3.4: Crystal Parameter of Y_2O_3:Tb nanostructures

Structural parameters	Calculated values
2θ	29.10
FWHM(deg)	0.45
Microstrain ε(10^{-3})	1.92
Lattice constant (Å)	10.62
Interplanar spacing (Å)	3.066

TEM and high resolution (HRTEM) images of the untreated Y_2O_3:Tb^{3+} sample are reported in Figure 10. As shown, the hydrothermal product consists of relatively dispersed elongated nanostructures with predominantly tubes features. The outer diameter was estimated of 100 nm and the length of about 1

μm. Beside a certain homogeneity in shape and dimension, the most relevant result concerns the porous characteristics in accordance with the hypothesis assumed for diffraction patterns.

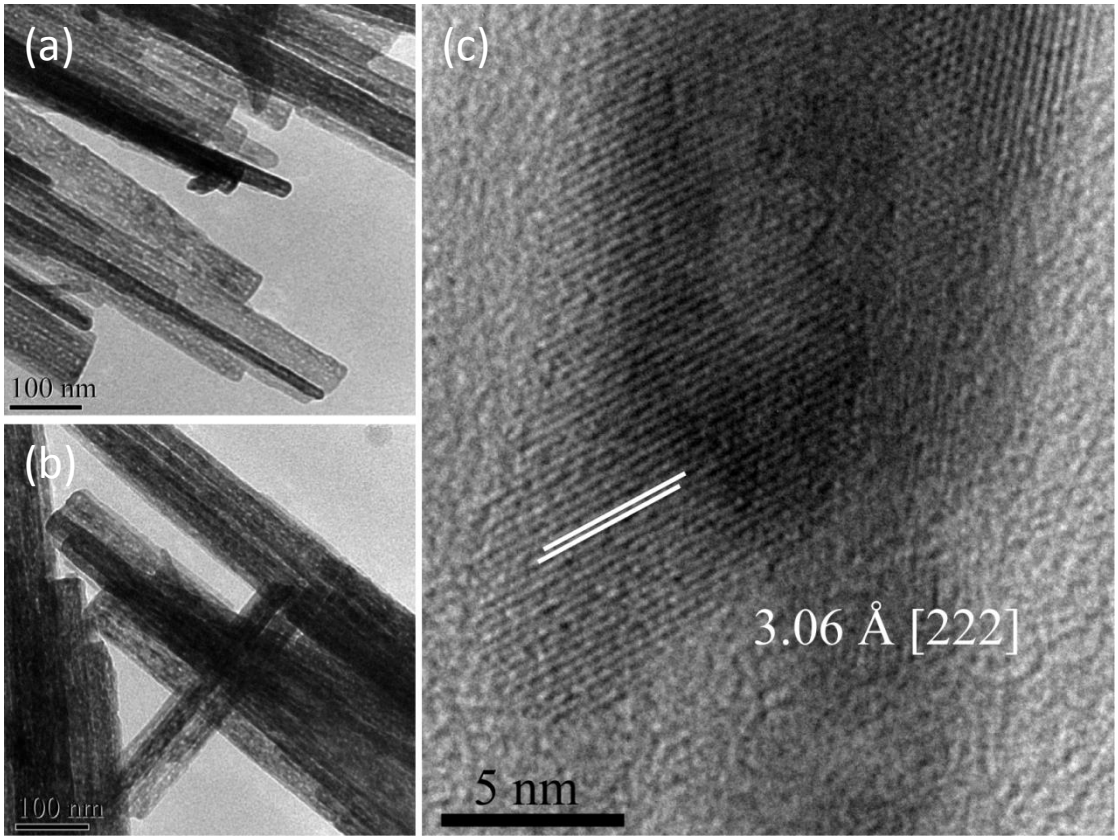

Figure 3.10 :TEM (a,b) and HRTEM (c) images of $Y_2O_3:Tb^{3+}$ nanostructures.

Below the temperature of 1000 °C Rare Earth sesquioxides crystallize in bixbyite-like cubic structure whose corresponding irreducible representation for the vibrational optical modes is

$$\Gamma_{opt} = 4A_g + 4E_g + 14F_g + 5A_{2u} + 5E_u + 16F_u \tag{3.9}$$

and therefore it accounts for 22 Raman (A_g, E_g, F_g) and 16 IR (F_u) active modes.

In a typical sesquioxides scattering spectrum we distinguish the frequencies region above 300 cm^{-1}, weakly influenced by Rare Earth ions and ascribable to oxygen motions and deformation of ReO_6 octahedra. O-Re-O and Y-O-Y bending mainly affect the lowest frequencies and Y-O stretching the higher ones[41].

Raman spectra of Y_2O_3:Tb^{3+} and melamine-Y_2O_3:Tb^{3+} samples are shown in Figure 3.11 and the respective assignments are summarized in Table 3.5.

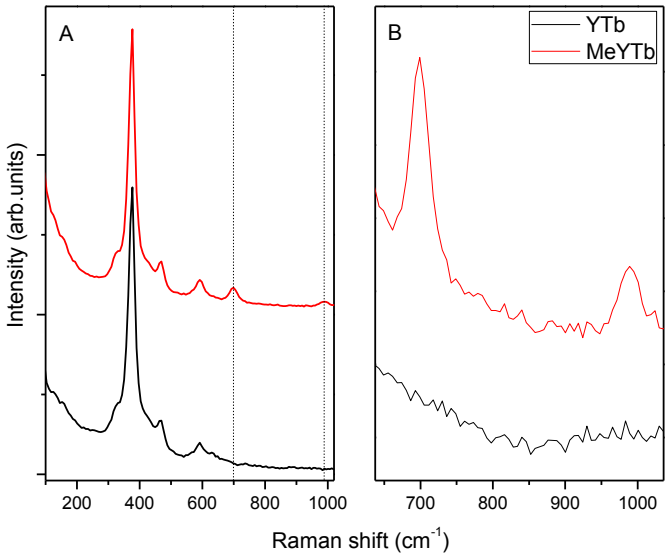

Figure 3.11: Raman spectra of Y_2O_3:Tb^{3+}. A) Extended Raman spectra. B) Particular of Raman spectra at 640-1036 cm^{-1} .

Table 3.5: Raman assignments (cm^{-1}) of YTb, MeYTb and Melamine samples

YTb	MeTb	Attribution	Melamine	Attribution
329		F_g+E_g	233	HNCN torsion
376		F_g	383	HNCN torsion
429		A_g	450	HNCN torsion
468		F_g	586	Out of plane CNC bending
592		F_g	675	Ring breathing II mode
	700	Ring breathing II mode	778	Out of plane NCN bending

990	Ring breathing I mode	983	Ring breathing I mode
		1443	CN stretching
		1556	CN stretching

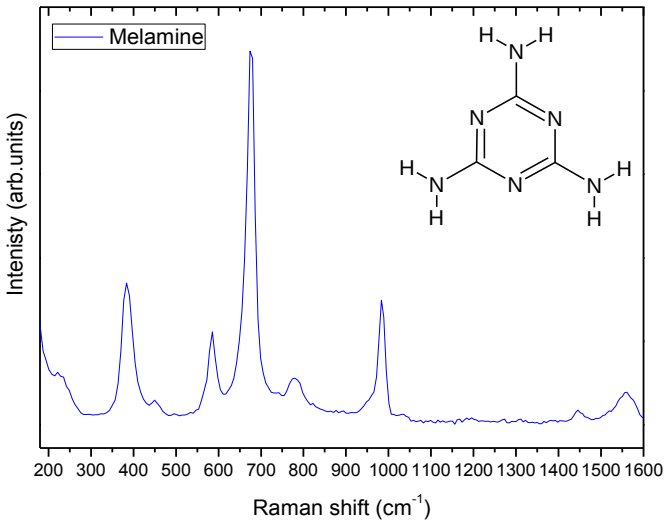

Figure 3.12: Raman spectrum of melamine.

Y_2O_3 nanotubes Raman spectrum is dominated by F_g mode at 376 cm^{-1} rising from Y^{3+}-O^{2-} vibration [42]. According to the most recent attributions, we identify the F_g modes at 468 and 592 cm^{-1} [43]. Furthermore, adjacent to the most intense contribution, we recognise two not completely resolved vibrations at 329 and 429 cm^{-1} attributed to F_g+E_g and A_g modes, respectively [43].

The organic functionalised sample presents new features at 700 and 990 cm^{-1} that could be attributed to the melamine (fig.3.11B). Taking into account the melamine Raman spectrum (Figure 3.12), two intense modes are individuated at 675 cm^{-1} and 983 cm^{-1}, originating from the ring breathing II mode and in-plane ring breathing I mode, respectively[44]. Raman modes at wavenumbers lower than 600 cm^{-1} typically belongs to N-H_2 (not observed in this work) and H-N-C-N stretching. The mode at 778 cm^{-1} and the peaks' couple at 1443 and 1556 cm^{-1} are due to out of plane N-C-N bending and C-N stretching, respectively[44] (see table 3.5 for the complete attribution).

D_{3h} symmetry based carbon-nitrogen compounds, including melamine and melem (2,4,6-triamino-tri-s-triazine), can present a marked N-donor behaviour; melamine, especially, can produce Cu

or Ag-based complex through the nitrogen atom of the aromatic ring. Conversely, it was proposed a strong interaction of melamine with gold surfaces through amino group in SERS experiments. The latter is motivated by a significant redshift of the mode at 675 cm^{-1} but not the one at 983 cm^{-1} [45].

Raman measurements on the hybrids melamine-yttria show a shift toward higher wave-numbers of about 25 cm^{-1} for the ring breathing II mode and only 7 cm^{-1} for the ring breathing I mode. In the light of this, we suggest chelation to the amine group's nitrogen atoms as the most likely mechanism, without significant involving of the ring N atoms.

Figure 3.13 shows the resulting excitation spectra (PLE) of melamine, Y_2O_3:Tb^{3+} and melamine-Y_2O_3:Tb^{3+} hybrid. Monitoring the characteristic emission of melamine powder in the UV region, the excitation spectrum reveals a structured broad band with a maximum at 312 nm (Figure 3.13A). At the present, we do not have knowledge of melamine excitation spectra at the solid state to compare with our results, but several works on the absorption of melamine in solution were already published [46][48]. According to Dewar and Paolini [46], the main absorption band of melamine in solution of water and ethanol is dominated by a singlet-singlet transition around 240 nm with a weak shoulder at 313 nm attributed to a singlet-triplet excitation. Most recently, fluorescence excitation spectra of melamine in water show the main excitation peak at 254 nm, with a weak contribution in the region between 260-320 nm[47]. Our starting powder present similar excitation features to the ones appearing in PLE measures on melamine powder after treatment at 300 °C showing a broad excitation band extending from 260 nm to 400 nm as a product of a condensation process[48].

Melamine luminescence exhibits an efficient emission picked at 356 nm and ~ 60 nm wide, with a long tail extending in the blue range, mainly originated by triplet-ground state recombination[47].

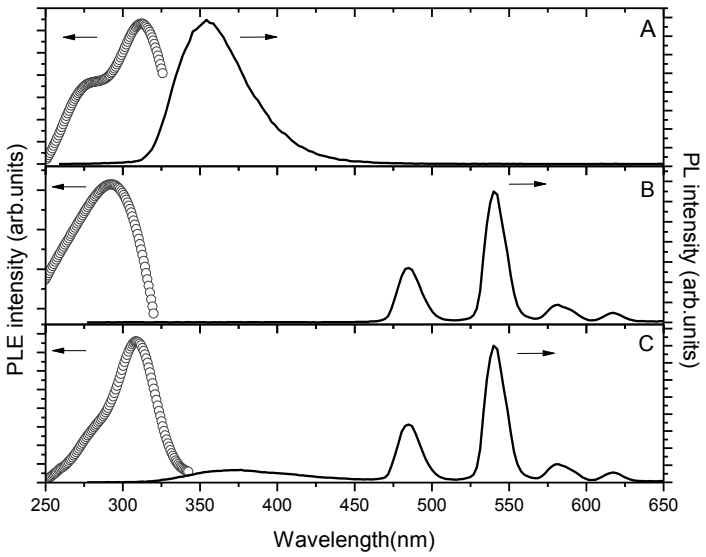

Figure 3.13: Photoluminescence Excitation (circles) and photoluminescence (solid line) spectra of Melamine (A, λ_{em} =360 nm, λ_{xc}= 270 nm), YTb (B, λ_{em}=542 nm, λ_{exc}= 290 nm) and MeYTb(C, λ_{em}=542 nm, λ_{exc}= 290 nm).

The main excitation channels of Terbium ions in yttrium oxide matrix are located at energies higher than 320 nm, optimally overlapping the excitation features of melamine molecule. PLE spectrum of Y_2O_3:Tb^{3+}, reported in Figure 13B, is acquired by monitoring the emission band centred at 542 nm. The continuum band picked at about 290 nm is ascribable to 4f-5d intraband transitions that are recognized to be largely dependent on crystalline environment or crystallite dimensions in nanoparticles systems[49]. The corresponding luminescence showing a group of four sharp bands is observed, namely 484 nm (J=6), 542nm (J=5), 583 nm(J=4) and 617 nm (J=3) in the region between 450 nm and 650 nm, all attributed to $^5D_4 \rightarrow F_J$ terbium ions radiative recombinations.

MeYTb hybrid (with molar ratio $n_{Me} / n_{YTb} = 2$) is characterized by a strong green luminescence displaying the characteristic bands of terbium ions combined with the emission of melamine (Figure 3.13C). The excitation spectrum of MeYTb recorded at the Tb emission (542 nm) presents the distinctive feature of melamine with an asymmetric broad band picked at about 310 nm, emblematic of a marked interaction between organic compound and lanthanide ion.

Focusing on melamine photoluminescence, a variation in the PL spectrum is observed. As shown in Figure 3.14, when melamine is adsorbed at yttria surfaces (sample MeYTb) the emission peak is red-shifted to 370 nm. This behaviour is in accordance with the one observed in Pr(III)-phenanthroline and RE(III)-melamine complex[50],[51]. Particularly in the latter, the energy related to $\pi \rightarrow \pi^*$ radiative transition can be significant affected by organic-metal coordination causing a redshift of about 12 nm from the intrinsic value [51].

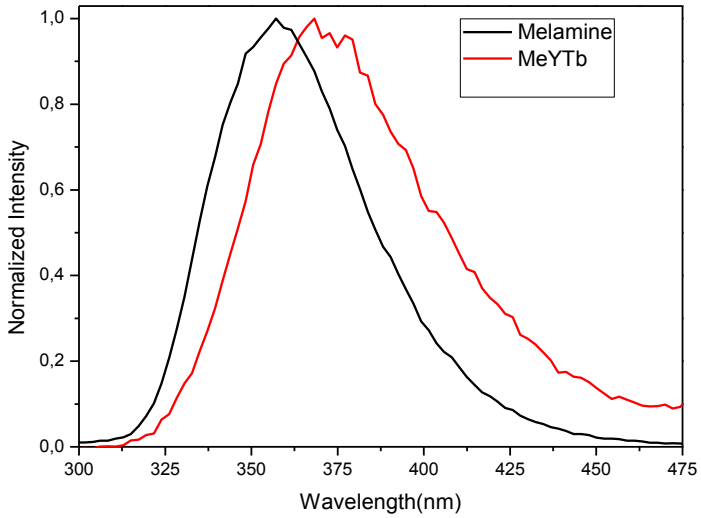

Figure 3.14: Melamine photoluminescence spectrum excited at 270 nm.

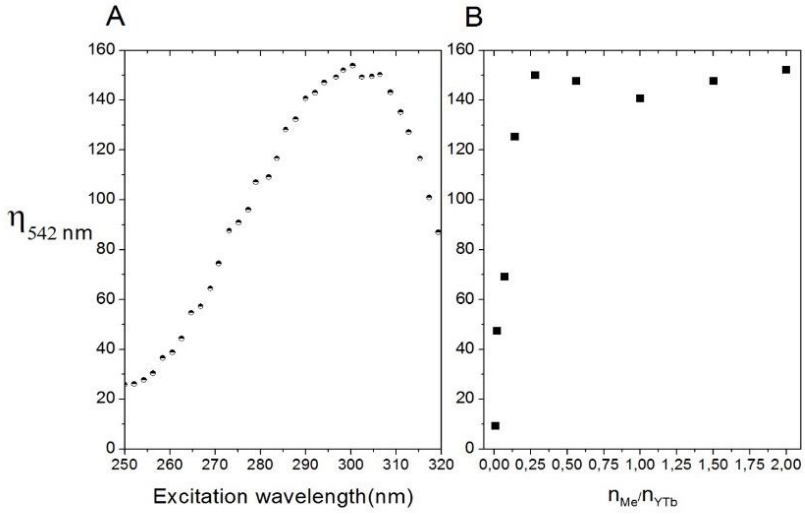

Figure 3.15 : A) η_{eff} parameter in the range 250-320 nm; (B) η_{eff} parameter as a function of molar ratio n_{Me} / n_{YTb}

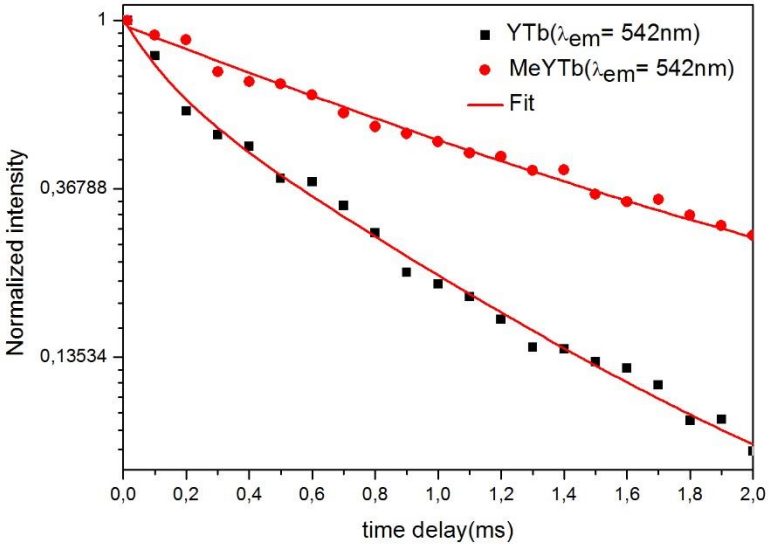

Figure 3.16 : Normalized luminescence decay at 542 nm of YTb (black dots) and MeYTb (red dots),λ_{exc}= 270 nm.

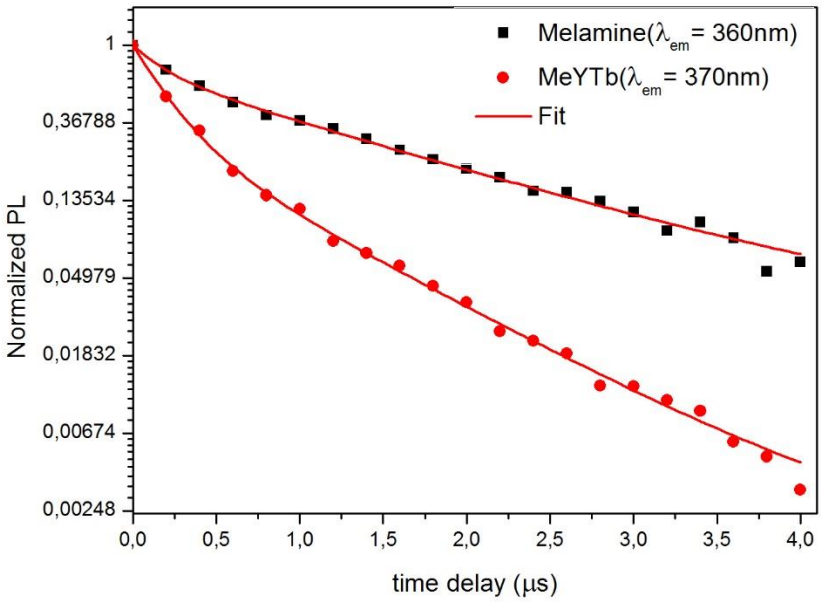

Figure 3.17 : Normalized luminescence decay of melamine (black dots) and melamine in MeYTb (red dots).

The shift toward lower energies of the melamine emission strongly represents an experimental evidence of the successful coordination among organic ligand and Rare Earth ions at the surfaces, in good agreement with hybrid Raman spectra characteristics.

In the composite organic-inorganic system the lanthanide emission is governed by the relation

$$I^*_{RE} = \eta(\lambda_{exc}) I_{RE} \tag{3.10}$$

in which we recognize the sensitization of Rare Earth (RE) ions by organic ligand in the form of intrinsic luminescence I_{RE} improvement. η is the increase factor and it will be dependent on excitation wavelength. In Figure 3.15A we report a representative sketch of η defined as the ratio I^*_{Tb}/I_{Tb} of the emission intensities at 542 nm ($^5D_4 \rightarrow F_5$). The factor η reaches the highest value with excitation wavelength of about 300 nm, where η~150. In the range between 250-320 nm we observe a luminescence improvement of one order of magnitude at least. η curve essentially follows the excitation spectrum of melamine with $\eta > 10^2$ for $\lambda_{exc} > 300$ nm where excitation spectrum is dominated by the organic feature. Figure 3.15B shows the progressive increase of η with the concentration of melamine. Above $n_{Me} / n_{YTb} = 0.3$ the maximum value of Tb luminescence is detected and it remains constant on a wide range.

Time resolved measurements in the scale of ms were performed in order to investigate possible effect of organic capping on Tb^{3+} ions radiative recombinations (Figure 3.16). For this purpose, the most intense band at 542 nm was monitored in the first 2 ms. As expected, $^5D_4 \rightarrow F_5$ of Tb^{3+} in Y_2O_3 presents a lifetime of several hundred μs. By an accurate comparison between the two samples, we observe a significantly difference in radiative decay. In general, Y_2O_3:Tb^{3+} photoluminescence presents two well-defined lifetimes and the decay profile follows a bi-exponential law[35]:

$$I(t) = I_1 exp\left(-\frac{t}{\tau_1}\right) + I_2 exp\left(-\frac{t}{\tau_2}\right) \tag{3.11}$$

with

$$\frac{1}{\tau} = \frac{1}{\tau_r} + \frac{1}{\tau_{nr}} \tag{3.12}$$

where τ_r and τ_{nr} represent radiative and non-radiative lifetime contribution to the overall time decay τ [35].

Pristine Y_2O_3:Tb^{3+} nanostructured luminescence can be fitted with two exponentials with lifetimes $\tau_1 = 0.13$ ms and $\tau_2 = 0.78$ ms (all expressed with an accuracy of 5%). Multiexponential trend of

terbium luminescence decay has been encountered in several works, especially in Gd_2O_3:Tb systems [52],[53]. The effect is always correlated to the energy dissipation by the presence of non-radiative recombination channels, mainly represented by other lanthanide ions whose levels can be populated by efficient interionic transfer and drastically increase with the doping concentration[54]. Moreover, structural defects and unsaturated bonds are always present at oxide surfaces whom tend to react with water and favour the formation of metal-hydroxides sites [55]. Hydroxyl group contribution became more important as the particles size decreases promoting non-radiative recombination paths, frequently observed in faster components during luminescence decays. The use of inorganic or organic shell can prevent this deleterious mechanism, separating the optical active core from OH-groups influence. Terbium ions deposited on porous anodic Al_2O_3 shows a strong luminescence quenching, related to non-radiative conversion in OH-groups vibration energies. It has been demonstrated that high temperature (>900°C) annealing process can decrease the amount of OH species at the surfaces achieving an improvement of terbium ions luminescence.

Defining the average time as [35]

$$\tau^* = \frac{I_1\tau_1^2+I_2\tau_2^2}{I_1\tau_1+I_2\tau_2} \tag{3.13}$$

and applying it to the luminescence decay in YTb sample, we obtain τ^*=0.73 ms. On the other hand, the photoluminescence decay of MeYTb nanostructures can be fitted with a single exponential with lifetime τ = 1.25 ms, resulting in an improvement (considered with respect to the average time of YTb) of about 70 %.

We argue that naturally hydrated surfaces undergo to hydroxyl groups desorption during the heat treatment at 500 °C under nitrogen flux. The resulting surfaces present high density of reactive centres involved in melamine adsorption. Melamine molecules tend to heal unsaturated bonds when deposited at high temperature on the yttria surface, influencing the dynamic of lanthanide ions recombinations. In this scenario, non-radiative contribution lessened, and so the τ_{nr}, causing the increase of terbium lifetime emission. Dorman et al. observed similar behaviour on $Y_2O_3:Er^{3+}$ nanoparticles passivated by an inert shell with an optimal size of about 8 nm. The nanoparticles display enhanced luminescence and a longer luminescence lifetime with an improvement of 53% [56].

To clarify the mechanism of energy transfer in melamine-Rare Earth complex is necessary to investigate the time evolution of the organic molecule luminescence. In Figure 3.17 we monitored the integrated luminescence of melamine in powders and coordinated to yttria nanostructures. As previously reported, the decay profile of melamine fluorescence exhibits two lifetimes, a fast component of 200 ns and the other with a lifetime of 1.5 μs, highly dependent on chemical environment. Accordingly, the interaction among adsorbed melamine and surfaces' ions induce the lowering of the slowest lifetime down to 860 ns (Table 3.6).

The main effect originating from the obtained hybrid melamine-Y_2O_3:Tb^{3+} nanostructure is an increase of doping ions luminescence efficiency. The reduced energy gap between melamine transition (resonant absorption condition) and Ln^{3+} levels, promotes an efficient energy transfer corresponding to a gain of about one order of magnitude. In agreement with the most accepted mechanism, the organic donor, excited in the range between 250-320 nm, undergoes to a first singlet state transition and relaxes to a triplet state through intersystem crossing. Then part of energy is transferred to D_4 levels of terbium ion which recombines with intense luminescence.

Table 3.6: Optical emitters Lifetimes.

Emitter	YTb	MeYTb	Melamine
	τ_1 / τ_2 (ms)	τ_1 / τ_2 (ms)	τ_1 / τ_2 (μs)
Tb^{3+}(λ_{em}=542 nm)	0.13 / 0.78	1.25	-
Melamine	-	$2.0x10^{-4}$ / $8.6x10^{-4}$	0.2 / 1.5

3.2 Carbon nitride/ TiO_2 based hybrids

In the last section, we have seen that the realization of a hybrid system can provide significant benefits to the optical response of oxide material. The new features of the phosphor was explained by the presence of two effects, an efficient organic to lanthanide energy transfer and the decreasing of quenching effect due to surface defects. In this context, it is important to realize the synthesis process, occurred at high temperature, preventing the saturation of defects with OH species.

There is a considerable amount of literature on organic-inorganic materials [57]-[60] with the purposes of obtaining systems with uncommon characteristics. In most cases, the synthesis of hybrid materials was addressed by the use sol-gel methods, forming dispersed inorganic materials in solvents by the means of metal-oxo polymers [60]-[62]. After the choice of compatible solvents and reactants, the hybrid is then obtained by mixing organic and inorganic components. Two classes of hybrids can be individuated. Class I hybrids present the two components linked through weak bonds (van der Walls, hydrogen bonds), which led to an effective doping of sol-gel matrix by organic molecules. At the root of the treatment, the inorganic precursor is mixed with the dye and the catalysts in a solvent with the adding of water to induce the polycondensation process or the xerogel is alternatively simply added to dye [60]. In both ways, a homogenous trapping of the organic molecules into the inorganic matrix can be achieved.

The second category of hybrids causes inorganic and organic to link by strong covalent bonds. The link between inorganic and organic parts could be a metal to carbon M-C bond where M is typically silicon, tin or lead, while M-O-C bonds is the most likely when M is a transition metal [60].

This section focuses on the realization of some TiO_2 hybrids with different techniques and on the description of organic-inorganic interaction by spectroscopy methods.

The first composite material involved Atomic Layer Deposition (ALD) technique as inorganic coating route. ALD synthesis was realized at Gent University. At the best of our knowledge, the obtained hybrid represented the first example of successfully organic/inorganic core/shell creation, through ALD metal oxide coating.

ALD procedure was performed at low temperature and under low vacuum conditions. In this method organic chemical characteristics and oxide precursors was the most critical parameters. The organic system needs to be highly stable in temperature and in vacuum, with terminating groups useful to the correct inorganic precursor bonding.

In light of this, we present our best results on N2,N4,N6-tri-p-tolyl-1,3,5-triazine-2,4,6-triamine (MeTT) system (chap.2). MeTT powders have been subjected to ALD treatment by Tetrakis(dimethylamino)titanium (TDMAT), precursor of Ti with methyl functional groups.

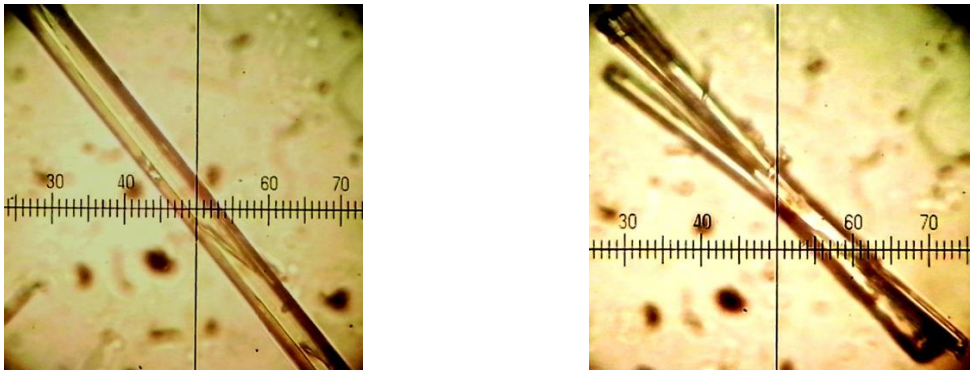

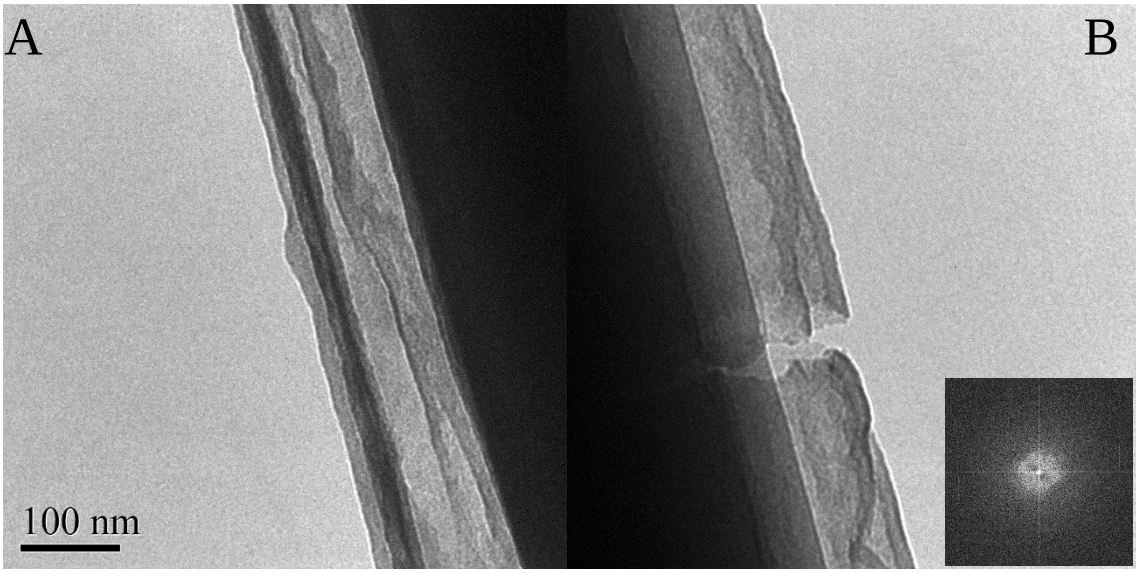

Figure 3.18: On top: back illuminated optical images of MeTT (left) and MeTT-TiO_2 (right). On bottom: Transmission Electron Microscopy images of core-shell MeTT-TiO_2 hybrids. A) Longitudinal profile of single titanium dioxide coated microwire. B) Particular of shell crack. Inset: FFT pattern of microwire.

Figure 3.18 shows the optical microscopy image of the as-prepared MeTT sample, which presented a well-defined morphology. The wires exhibited lengths in the order of several micrometres and diameter of several hundred nanometres.

After ALD treatment, MeTT-TiO_2 did not reveal change at optical microscope and it motivated an investigation by TEM. As reported in Figure 3.18, the microwires presented a shell of amorphous TiO_2 of about 100 nm in size (see FTT pattern in inset).

Figure 3.19A features the spectral emission of MeTT-TiO_2 samples in comparison with the pristine ones.

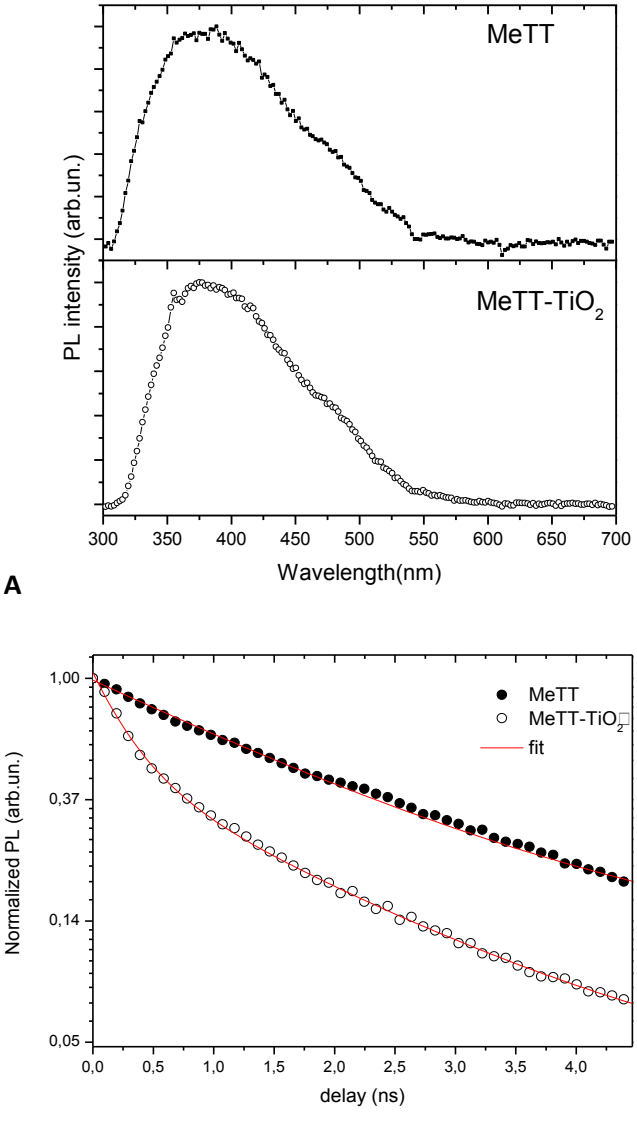

Figure 3.19: A) Steady state emission spectrum excited at λ_{exc} = 270 nm B) Time decay of PL measured in the 5 ns time range after the pulse laser (λ_{exc} = 355 nm).

As expected, we did not revealed significant change in the spectral emission, demonstrating that the amorphous oxide does not affect the emission of organic part of the hybrids.

With the aim to investigate organic-inorganic interaction, time-resolved measurements were performed. The modalities and the experimental setup has been described in chapter 2. Briefly, a pico-second-laser with wavelength emission at 355 nm and pulse width of 300 ps was employed to study the visible emission of hybrids in the first 10 ns after the laser excitation. The results are reported in figure 3.19B. MeTT luminescence decay present a single exponential nature with lifetime $\tau = 1.96$ ns. When enclosed in a metal oxide shell, the decay profile turns into two exponential law, with lifetimes of $\tau_1 = 0.30$ ns and $\tau_2 = 1.79$ ns.

This results suggest a strong interaction between the organic core and the inert shell, where the photoexcited carrier in the core are pumped in the outer inorganic layer [63],[65]. However, the unchanged spectral shape between the hybrid system and the pristine organic compounds as well almost preserved optical efficiency, confirm the hybrid system as god candidate for photonic applications.

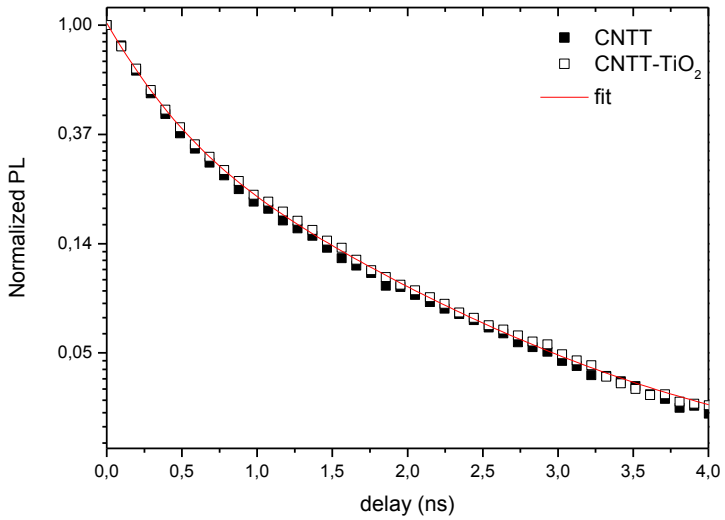

Figure 3.20: PL time decay of CNTT and CNTT- TiO_2 samples measured in the 5 ns time range after the pulse laser (λ_{exc} = 355 nm).

CNTT powders were subjected to ALD treatment, using the same growth parameters of MeTT-TiO_2. No difference was found between pristine CNTT samples and CNTT-TiO_2 core-shell systems. Our

findings would seem to suggest the lack of interaction between organic and inorganic parts, probably related to the absence of chemical bonds. We believe that the TiO_2 precursor TDMAT does not effectively interact with the molecule's functional groups, preventing the correct realization of hydroxides layer for the subsequent thickening of the shell. Research into solving this problem is currently in progress.

It has been suggested the realization of metal oxides-carbon nitride hybrids as photoanodes for photocatalysis appications [63]-[66]. In their seminal papers, researchers tried to overcome the obstacles intrinsically related to the use of metal oxide for photoelectrochemical water splitting. Among the requirements for photocatalysis purposes, the material needs to be an efficient light absorber with photoelectrochemical and surface catalytic properties [63]. Unfortunately, not all the mentioned features are present at the same time and smart expedient are necessary. For example, TiO_2 has great surface tailored catalytic performances but energy band-gap (3.2 eV) too high to absorbed efficiently visible radiation. Fe_2O_3 shows low bandgap (~2.1 eV) but the potential of its conduction band edge is not sufficiently negative to promote proton reduction without the application of additional electric bias [63].

Recently, the visible light photoactivity on PCN-TiO_2 composite materials were deeply studied [63],[65],[67], but the kinetic of organic to inorganic interaction is not yet been tackled. For this reason, we propose time resolved measurement of hybrid system, performed in the range of 20 ns.

Hybrid materials were prepared according to the methods described in ref. [63]. A certain amount of melamine powders (Aldrich, 99 %) was put in an alumina crucible , placed in a quartz tube accommodated in tubular furnace and treated at the temperature of 500 °C for 2h at the rate of 5°C/min under nitrogen flux (30 ml/min). The annealed powders were impregnated with a solution of titanium tetraisopropoxide. Then, the powders were treated in air at 500 °C for 2h.

A selected TEM image of PCN - TiO_2 is showed in Figure 3.21. Contrarily to the case of MeTT-TiO_2 system, the correct identification of the PCN - TiO_2 morphology results arduous, since the graphitic carbon nitride did not present a well-defined shape and dimension. Moreover, the low crystallinity of the organic part prevented the discernment between organic and inorganic. Basing our considerations on the difference of contrast, we suppose that the organic nano/micro-particles (dark) were trapped into an inorganic matrix as a result of the sol-gel impregnating procedure.

Raman spectrum of PCN - TiO_2 is reported in Figure 3.22. All the peaks are due to the presence of melon phase of carbon nitride (see chapter 2). However, no Raman modes ascribable to titanium dioxide are revealed. According to TEM images and the previous works [63], we believe that the thin TiO_2 was in amorphous state.

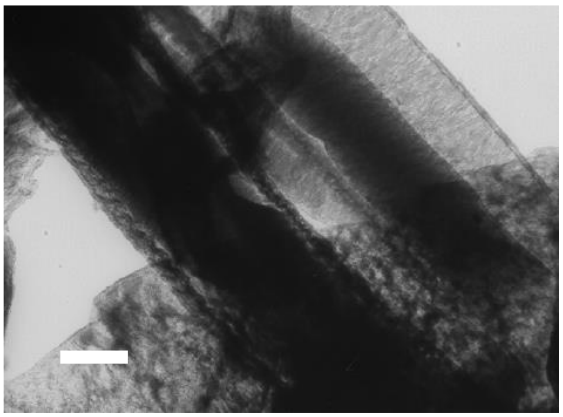

Figure 3.21: Transmission electron images of PCN- TiO_2 material. Bar data: 200 nm.

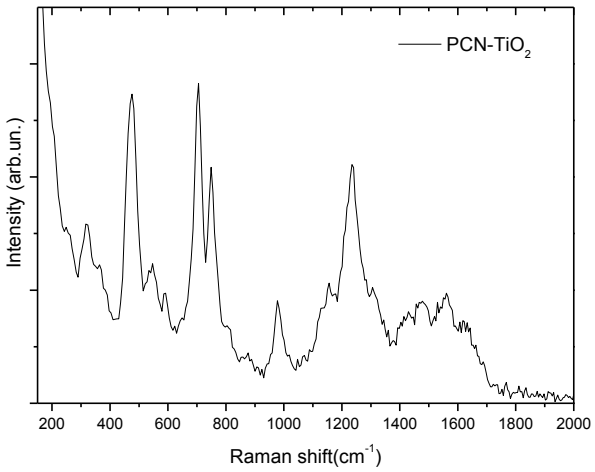

Figure 3.22: Raman spectrum of PCN-TiO_2.

In Figure 3.23 we compared the PL of bare PCN and hybrid under steady state excitation at λ_{exc} = 355 nm. The pristine sample displays the characteristic luminescence of PCN, obtained by annealing treatment at 500 °C. The PL is peaked at λ_{em} = 440 nm with a long tail up to 650 nm. PCN - TiO_2 hybrid presents an emission shifted at λ_{em} = 450 nm with a slight enlargement toward the low energies. This behavior was frequently observed in analogous TiO_2 / organic hybrids and it was attributed to the correct

functionalization of the metal oxide [68],[69]. In accordance, we observed a variation on the decay profile of PL as featured in figure 3.24. As mentioned in Chapter 2, graphitic carbon nitride based materials present a decay time of PL describable with a two exponential function. This behavior is retained in the hybrid, when we measure a decrease of the faster component lifetime, from 0.54 ns to 0.45 ns, suggesting the strong interaction between the core and shell system.

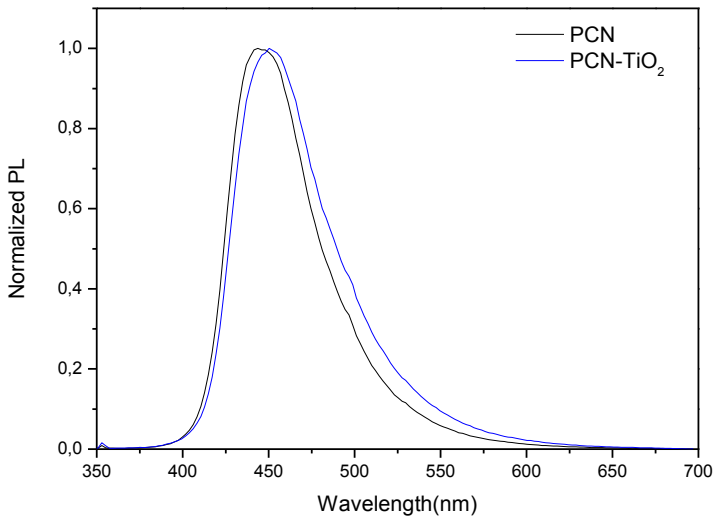

Figure 3.23: Steady state PL of PCN and PCN - TiO_2 at the excitation wavelength λ_{exc} = 355 nm.

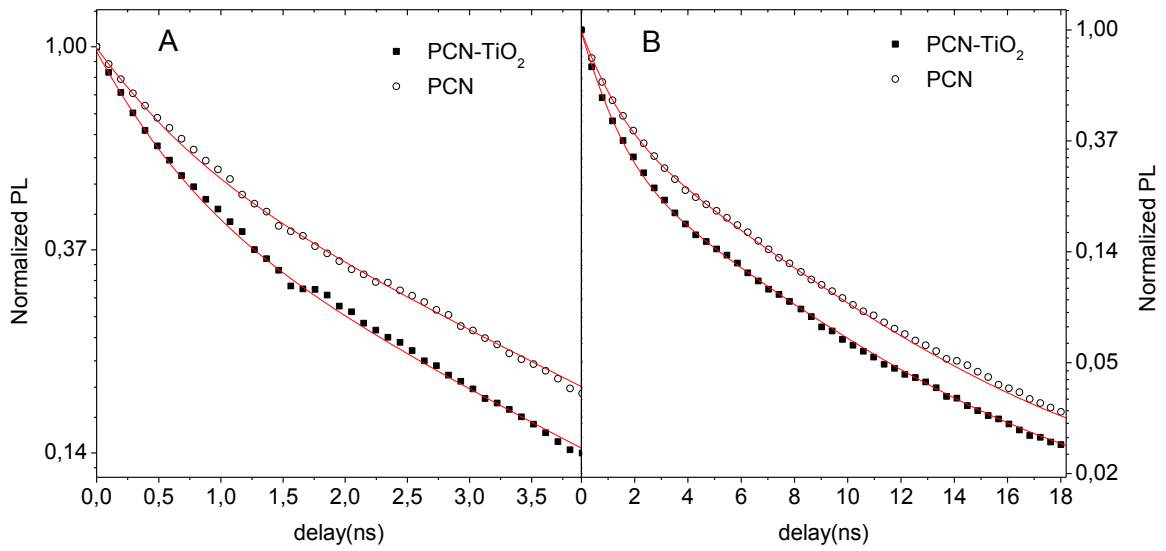

Figure 3.24: PL time decay of PCN and PCN - TiO_2 samples measured after the pulse laser (λ_{exc} = 355 nm). A) time range 5 ns. B) time range 20 ns.

The findings on the optical properties strongly suggest an interaction between organic and metal oxides, very similar to the situation of MeTT sample and the ALD method.

The aforementioned prospective related to PCN - TiO_2 and its chemical and thermal stability motivated the attempt to realize a heterostructure based on the CNTT_300 system as follow.

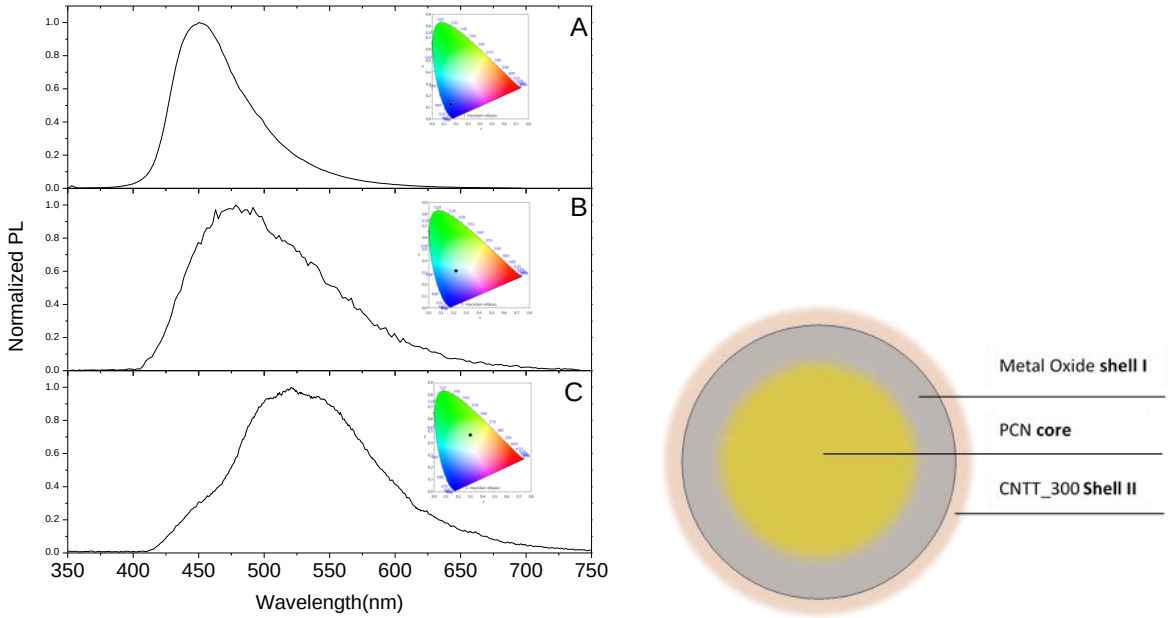

Figure 3.25:Left: PL spectra of PCN - TiO_2 (A), PCN - TiO_2 / CNTT_300 1:1 ratio (B) and PCN - TiO_2 / CNTT_300 1:4 ratio (C). Right: simplified scheme of the hybrid.

For the realization of heterostructure we have been guided by the work of Ricci and co-workers [68], who created an hybrid systems based on TiO_2 nanotubes and cumarine by the means of a thermal treatment of the oxide at a temperature higher than 100 °C in air, adding the solution of coumairne by dip-coating technique. Accordingly, we prepared a solution of CNTT_300 in DMSO. The PCN - TiO_2 system was treated at the temperature of 120 °C for 5 minutes. Then, the solution of CNTT_300 were deposited by dip coating. Finally, the functionalized sample was treated at 180 °C until the solvent evaporated.

The final heterostructure will have an internal core of heptazine, embedded in the inert inorganic shell of TiO_2. This outer shell has the function to provide efficient linkage to the second shell, formed by the CNTT_300 compound.

Figure 3.25 compares the photoluminescence excited at 355 nm of the PCN - TiO_2 (figure 3.25 A) and the PCN - TiO_2 / CNTT_300 (figure 3.25 B-C) with different concentration ratio of the starting heptazine and CNTT_300. The ratio 1:1 (fig. 3.25 B) determines a luminescence centered at about 480 nm

with a contribution at about 520 nm due to presence of CNTT_300. At the increase of CNTT_300 concentration a well-defined emission at 520 nm appears with a weak component at about 450 nm originated by PCN - TiO_2 (fig. 3.25 C).

To investigate the influence of TiO_2 shell on the optical properties of CNTT_300, we performed time resolved luminescence of the PCN- TiO_2 / CNTT_300 with 1:4 ratio.

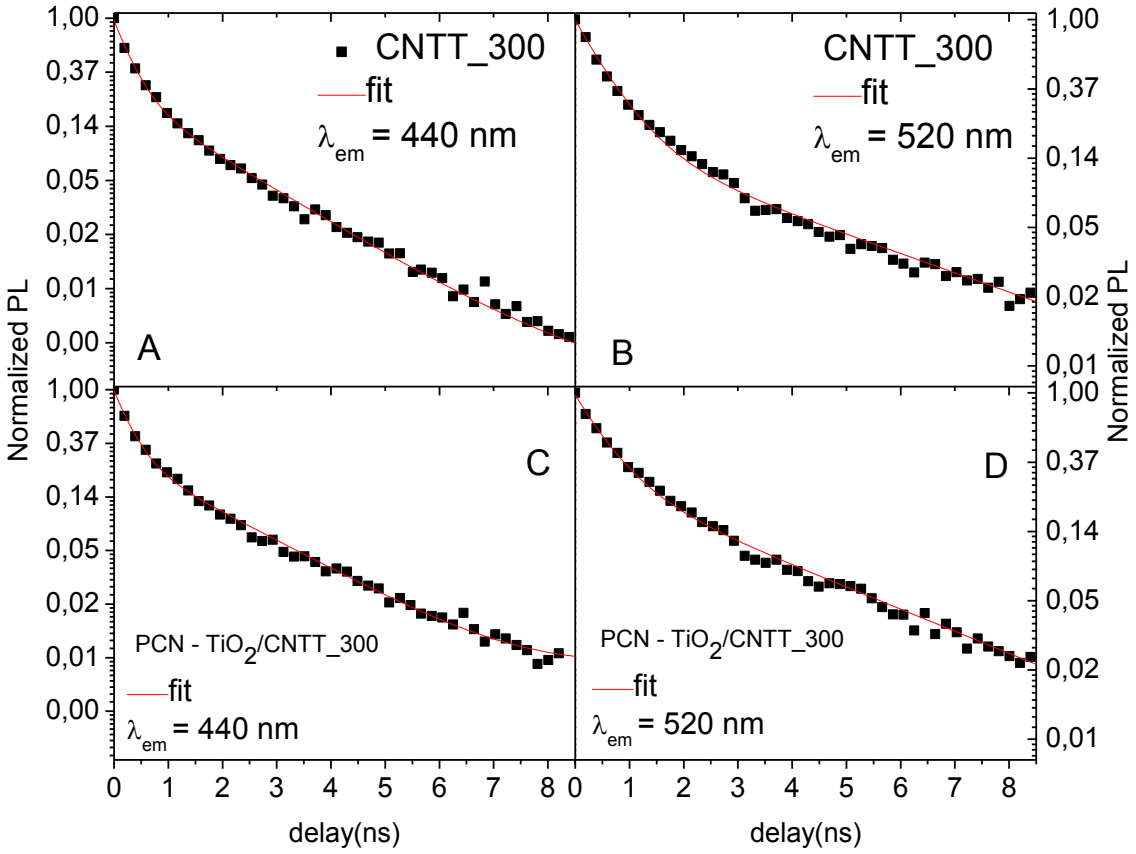

Figure 3.26: Time decay of photoluminescence. A) CNTT_300 λ_{em} = 440 nm; B) CNTT_300 λ_{em} = 520 nm; C) PCN - TiO_2 / CNTT_300 λ_{em} = 440 nm; D) PCN - TiO_2 / CNTT_300 λ_{em} = 520 nm.

Figure 3.26 reports the time decay of PCN-TiO_2/ CNTT_300 compared with the luminescence decay of CNTT_300. To study the PL decay process of the heterostructure PCN-TiO_2/ CNTT_300 is mandatory to take into account the different spectral contribution of two components, i.e. the emission wavelength at 440 nm, signature of PCN , and at 520 nm attributed to CNTT_300. Moreover, it is convenient for a correct analysis of experimental data to monitor the same wavelength for CNTT_300 sample.

In the time range of 10 ns, CNTT_300 decay at the emission wavelength λ_{em} = 440 nm is characterized by a two exponentials equation, whose lifetimes are τ_1 = 0.41 ns and τ_2 = 1.65 ns. At λ_{em} = 520 nm the experimental data fits with a two exponential law with τ_1 = 0.61 ns and τ_2 = 3.60 ns.

At λ_{em} = 440 nm we have to consider the emission of heptazine to better describe the kinetic of PL decay in PCN-TiO_2/ CNTT_300. The decay profile has to be fitted by three exponential equation, in which one contribution is fixed by the lifetime τ_3 = 3.04 ns of PCN -TiO_2 (see Table 2.7 in Chapter 2). The resulting fitting parameters for the whole PCN-TiO_2/ CNTT_300 system are τ_1 = 0.31 ns and τ_2 = 0.83 ns, evidencing a decrease of PL lifetime. At λ_{em} = 520 nm the experimental data for PCN -TiO_2/ CNTT_300 are well-fitted by two exponentials with τ_1 = 0.58 ns and τ_2 = 3.14 ns. Since the contribution of PCN -TiO_2 results negligible in the monitored spectral region, we conclude that the CNTT_300 life-time decrease when the heterostructure is created.

Table 3.7 : Lifetimes of CNTT_300 and PCN-TiO_2/ CNTT_300.

Lifetimes (ns)	CNTT_300		PCN-TiO_2/ CNTT_300	
	λ_{em} = 440 nm	λ_{em} = 520 nm	λ_{em} = 440 nm	λ_{em} = 520 nm
τ_1	0.41	0.61	0.2	0.58
τ_2	1.65	3.60	0.83	3.14
τ_3	-	-	3.04	-

Summarizing, we have engineered and realized a heterostructure with high optical efficiency and wide emission optically pumped in the blue spectral region. Both the contributions of the two organic systems contribute to a large emission in the visible range while the inorganic central shell has the double effect: to preserve the internal organic core (heptazine) and to provide the suitable linkage of the outset organic shell (CNTT_300). This proof of feasibility represents the starting point for new composite heterostructures further implementable with additional inorganic shells covered by emitting organic layers for photonic purposes.

3.3 Summary of Chapter 3

This chapter was devoted to the study of organic-inorganic hybrids. In the first part, we investigated energy transfer mechanism of rare earth doped matrix by the means of time-resolved photoluminescence technique, taking into account the exemplar case of Ce and Tb co-doped Y_2SiO_5. This host presents outstanding luminescent performances and the interaction between the two kind of active ions tends to assume a general behaviour, with no significant influence by the matrix. At nanoscale RE ions in oxide matrix rarely present a high quantum yield because of the high rate of non-radiative recombinations, caused by the defects at surfaces and the presence of OH- groups, mainly detrimental for IR emission. In the light of this, a functionalization of oxide surfaces with melamine has been obtained by thermal deposition method under nitrogen flux at 500 °C preventing the polymerization of organic ligand. The achieved hybrid exhibits a strong luminescence in the green region with an improvement of efficiency compared with pristine sample. This result can be explained in the framework of an energy transfer between melamine and RE ions and it is confirmed by the reduced lifetime of melamine emission. Moreover, the increase of Tb^{3+} lifetime suggests the removal of surface defects and related optical quenchers in the presence of organic ligand. High temperature synthesis of melamine-oxide hybrids compounds favors an OH- free strategy to obtain an effective improvement of lanthanides based nanoscaled phosphors.

In the second part, we studied different titanium dioxide based heterostructures demonstrating the feasibility of organic/inorganic core/shell system by ALD method and the interaction of triazine and oxides parts and extending this architecture to the heptazine-based compounds using most friendly chemical methods. Finally, we engineered a system based on organic/inorganic/organic heterostructures, evidencing the high degree of luminescence tunability for potential photonic applications.

3.3 References

[1] J. Garcìa Solé, L.E. Bausà , D. Jaque. An Introduction to the Optical Spectroscopy of Inorganic Solids. Wiley(2005).
[2] R. P. Powell Physics of Solid-State Laser Materials, AIP press-Springer
[3] M. Salis, C.M. Carbonaro, R. Corpino, A. Anedda, PC.Ricci, J. Phys. Condens. Matter, 24, 295401, (2012).
[4] X. Zhang, L.Zhou , Q.Pang,J. Shi J.;M.Gong , J. Phys. Chem. C, 118, 7591-7598 (2014).
[5] P.C. Ricci; C.M. Carbonaro; R. Corpino; C.Cannas; M. Salis, J. Phys. Chem. C, 115, 16630 (2011).
[6] Q. Guo ;L. Liao;Z. Xia; J. of Luminescence, 145, 65 (2014).
[7] P.C. Ricci;M. Salis, R.Corpino; E. Fortin; A. Anedda, J. Appl. Phys, 108, 043512, (2010).
[8] S.M.F.Vilela , D.Ananias, A.C.Gomes, A.A.Valente; L.D.Carlos; J.A.S. Cavaleiro; J.Rocha; J.P.C. Tomé, F.A. Almeida Paz, J. Mater. Chem. 2012, 22, 18354 (2012).
[9] H. Liang, Y. Tao Y.,Q. Su ;S. Wang, J. Solid State Chem. 2002, 167, 435 (2002).
[10] A. Potdevin, G. Chadeyron ; R. Mahiou, Chem. Phys. Lett., 490, 50-53, (2010).
[11] C. Cannas; M. Mainas;A. Musinu;G. Piccaluga; S. Enzo; M.Bazzoni; A. Speghini; M. Bettinelli ;Opt. Mater, 29, 585 (2007).
[12] T. Hirai; Y. Kondo; J. Phys. Chem. C 111, 168-174, (2007).
[13] S. Saha, P.S. Chowdhury,A. Patra, J. Phys. Chem. B 109, 2699-2702 (2005).
[14] Popovich N.V., Sarkisov P.D., Popova M.N., Lyamkina O.D., Galaktionov S. S., Soshchin N.P., Inorg. Mater.38, 734-738, (2002).
[15] P.C. Ricci; D. Chiriu; C.M.Carbonaro; S. Desgreniers, E. Fortin; A.Anedda J. Raman Spectroscopy, 39, 1268-1275 (2008).
[16] J. Reichardt, M. Stiebler, R. Hirrle andS. Kemmler-Sack physica status solidi (a) 1990, 119, 631–642.
[17] J. Shmulovich, G. W. Berkstresser, C. D. Brandle and A. Valentino J. Electrochem. Soc. 1988 135, 3141-3151
[18] H. Suzuki, T.A Tombrello, C.L. Melcher and J.S. Schweitzer: IEEE Trans. Nucl. Sci. Vol. 1993, 40, 380
[19] C. Wanarak, W. Chewpraditkul, A. Phunpueok, and J. Kaewkhao, Advanced Mater. Res. 2011, 199-200, 1796-1803
[20] B. Wang; Y. Lin; H. Ju, J. Alloys Compd., 584, 167-170, (2014).
[21] Inokuti M., Hirayama F., J. Chem. Phys., 43, 1978-89 (1965).
[22] D.L.Dexter ;J. Chem. Phys., 21, 836-850, (1953).
[23] T. Forster; Naturfurshung, 12, 233 (1950).
[24] S. Kim, K.Woo, K. Lim, K. Lee, H. Jang, Nanoscale, 5, 9255-9263 (2013).
[25] R. Reisfeld, N. Lieblich-Soffer, J. Solid State Chem., 28, 391-395, (1979).
[26] Z.G. Xia, R.S.Liu, J. Phys. Chem. C, 116, 15604,(2012).
[27] P. C. Ricci, C. M. Carbonaro, A. Casu, C. Cannas, R. Corpino, L. Stagi, A. Anedda, J. Mater. Chem., 2011, 21, 7771-7776
[28] C. Cannas, M. Casu, A. Lai, Musinu and G. Piccaluga PCCP, 4, 2286 (2002).
[29] T. Gougousi and Z. Chen, Thin Solid Films , 516, 6197 (2008).
[30] H.Guo, W. Zhang, L.Lou, A. Brioude and J. Mugnier, Thin Solid Films, 458 , 274 (2004).
[31] A. van Dijken, J. Makkinje and A. Meijerink, J. Lumin., 92, 323 (2001).
[32] M. A.A. Attia,S. Garroni, D. chiriu, C.Ricci, F.Delogu, R.Orrù and G. Cao, Chem. Phys. Lett. 618, 108(2015).
[33] C. Cannas, M. Casu, A. Musinu, G. Piccaluga, A. Speghini and M. Bettinelli J. of Non-Cryst.Sol., 306, 2, 193 (2002).
[34] H.J.Liang , G.Y. Chen, L.Li, Y. Liu, F. Quin, Z.G.Zhang, Opt.Commun. ,282, 3028 (2009).
[35] Q. Lü, Y. Wu, L. Ding, G. Zu, A. Li, Y. Zhao and H. Cui , J. Alloys Compd, 496, 488 (2010).
[36] L. Ji, N. Chen, G. Du, M. Yan and W. Shi, Ceramics International, 40 , 3117 (2014).
[37] A. Ishii and M. Hasegawa, Sci. Rep., 5, 11714 (2015).
[38] J-C. Bünzli and C. Piguet , Chem.Soc.Rev., 34, 1048 (2005).
[39] S. Som and S.K. Sharma J. Phys. D: Appl. Phys. 45, 415102 (2012).
[40] Y.H. Zhao, K. Zhang and K. Lu , Phys. Rev. B 56, 22 (1997).
[41] Y. Repelin, C. Proust, E. Husson and J.M. Beny. J. Solid State Chem. , 118, 163 (1995).
[42] J.Q. Xu , S.J. Xiong, X.L. Wu T.H Li, J.C. Shen and P.K. Chu J. App. Phys. 114, 093512 (2013).
[43] M.V, Abrashev, N.D. Todorov and J. Geshev J. App.Phys 116, 103508 (2014).
[44] M. Prabhaharan, A.R. Prabhaharan, S. Gunasekaran and S. Srinivasan, Spectr. Acta part A 123, 392 (2014).
[45] A. Kim, S.J. Barcelo, R. S. Williams and Z.Li Anal. Chem., 84 , 9303 (2012).
[46] M. J. S. Dewar and L. Paolini Trans. Faraday Soc., 53, 261 (1956).
[47] C. Yang, Y. Liu and F. Zhang, Spect. Acta part A 75, 1329 (2010).
[48] Y. Zhang, Q. Pan, G. Chai, M. Liang, G. Dong, Q. Zhang and J. Qiu, Scientific Reports, 3, 1(2013)
[49] Y.L. Soo, S. W. Huang, Z. H. Ming and Y.H. Kao, J. App. Phys., 83, 5404 (1998).
[50] M. Hasegawa, A. Ishii and S. Kishi, J. Photochem. Photobio.,178, 220. (2006)
[51] M. Hasegawa, A. Ishii, K. Habu, H. Ichikawa, K. Maeda, S. Kinshi and Y. Shigesato Sci. Tech. Advanced mater. , 7, 72 (2006).
[52] B. Mutelet, P. Perriat, G. Ledoux, D. Amans and F. Lux et al. J. App. Phys. 110, 094317 (2011).
[53] C. Louis, S. Roux, G. Ledoux, C. Duajadin, O. Tillement, B.L. Cheng and P. Perriat Chem. Phys Lett. 429, 157 (2006).
[54] P.C. Ricci, M. Salis, R. Corpino, C. M. Carbonaro, E. Fortin and A. Anedda J. Appl. Phys. 108, 043512 (2010).
[55] L. Stagi, J.A. De Toro, A. Ardu, C. Cannas, A. Casu, S.S. Lee and P.C. Ricci J. Phys. Chem C ,118, 2857 (2014).
[56] J. A. Dorman, J. H. Choi, G. Kuzmanich, J.R. Bargar and J.P. Chang J. Phys. Chem C, 116, 10333 (2012).
[57] P. Fattahi, G. Yang, G. Kim, M. R. Abidian Adv. Mater. 26, I, pages 1846 (2014).
[58] R. Pardo, M. Zayat. Chem. Soc. Rev., 40, 672–687 (2011).
[59] M. Wrigth, A. Uddin. Solar Energy Materials & Solar Cells 107 , 87–111, (2012).
[60] P. Judeinstein, C. Sanchez. J. Muter. Chem., 6(4), 511-525 (1996).

[61] C J Brinker and G Scherrer, in Sol-Gel Science, The Physics und Chemistry of Sol-Gel Processing, Academic Press, San Diego, (1989).
[62] J Livage, M Henry and C Sanchez, Prog Solid State Chem ,18,259,(1988).
[63] M. Bledowski; L.Wang; A. Ramakrishnan; O.V. Khavryuchenko; V.D. Khavryuchenko; PC. Ricci; J. Strunk; T.Cremer; Kolbeck, C.; R. Beranek , Phys. Chem. Chem. Phys., 13, 21511−21519 (2011).
[64] R. Beranek and H. Kisch, Electrochem. Commun., 9,761–766 (2007).
[65] R. Beranek and H. Kisch, Photochem. Photobiol. Sci., 2008, 7, 40–48.
[66] R. Beranek, J. M. Macak, M. Gaertner, K. Meyer and P. Schmuki, Electrochim. Acta, 54, 2640–2646 (2009).
[67] L. Zhang, D. Jing, X.She, H.Liu, D. Yang, Y. Lu, J. Li,Z. Zheng, L. Guob J. Mater. Chem. A,2, 2071–2078 (2014).
[68] P.C. Ricci A. Da Pozzo S. Palmas F. Muscas , C.M. Carbonaro Chemical Physics Letters 531, 160–163 (2012).
[69] S. Palmas, A. Da Pozzo , M. Mascia , A. Vacca, P.C. Ricci Chemical Engineering Journal 211–212; (2012).

Conclusions

The subject of this thesis was the realization of new interesting systems with potential applications in the ambits of materials science. The study was performed by the employment of different experimental techniques in order to achieve a deep insight in the optical and structural properties of inorganic and organic compounds.

As starting point, we focused on the characterization of nanometer-sized metal oxides (MOs) particles and the phenomenon of the crystal phase transformation. Our experiments are performed in different environments. In the case of TiO_2 anatase, we showed that a phase transition occurs when the system was irradiated through an athermal mechanism closely related to the interaction of the particle surface with the chemical surroundings. In particular, the electron excitation processes activated by irradiation affect the rate of absorption and desorption of oxygen molecules, which in turn can be related to the number of oxygen vacancies at the particle surface. Photoluminescence experiments revealed a strong correlation between the transformation process and the optical properties originated by intrinsic defects. The change of phase resulted in the formation of stable chemical bonds between the surfaces of neighbouring particles. Extending these considerations to the case of γ-Fe_2O_3 we learned to effective control the transformation effect by the realization of γ-Fe_2O_3/SiO_2 core/shell nanoparticles, where the phase transformation cannot be obtained by light irradiation but only by heat treatment at very high temperature (1100°C), almost 700 °C higher than that for γ-Fe_2O_3 bare nanoparticles. Moreover, we observed that the transformation is always accompanied by the shells collapse and the aggregation of Fe_2O_3 nanoparticles diffused inside the silica matrix, clearly suggested a general mechanism for oxide nanosystems. We believe that our findings proved the capability to preserve the physical properties of oxides with low stability in synthesis process at high temperature.

Some of the limited performances of the metal oxides are related to negligible absorption in the visible, lack of optical emission or conduction band edge inadequate to promote proton reduction. To increase the range of applicability we can create hybrid systems, whose organic part provides specific properties to support the use of the oxide. One of the crucial problem is the choice of the organic systems. In our work, we individuated C_3N_4 compounds as useful candidates. We showed trough experimental

data and ab initio calculations that heptazine polymers present a strict correlation between structural and optical properties as a function of annealing temperature. By studying the substituted triazine molecules, we individuated a high stable system, whose properties are easily tuned by thermal treatment.

All the mentioned organic compounds represented stable products that can be employed in synthesis or functionalization process taking place at high temperature.

Finally, we proposed some examples of hybrids applications.

To address the issue of the optical properties in RE doped materials, we considered the example of Y_2SiO_5 matrix, realized by sol-gel methods. The analysed system contributed to evidence the mechanism of radiative recombinations and concentration dependence of spectral emission.

Bearing in mind the results on C_3N_4 and Y_2SiO_5, we investigated the problem of low efficiency in nanosized Y_2O_3: Tb^{3+}, suggesting a possible solution by organic/inorganic hybrid approach. Terbium doped Y_2O_3 nanostructures were synthesized by hydrothermal method, displaying porous surfaces facilitating the anchoring and adsorption of ligand molecules. Consequently, a functionalization of oxide surfaces with melamine has been obtained by thermal deposition method under nitrogen flux at 500 °C. The achieved hybrid exhibits a strong luminescence in the green region with an improvement of efficiency compared with pristine sample. This result was explained in the framework of an energy transfer between melamine and RE ions and it is confirmed by the reduced lifetime of melamine emission. Moreover, the increase of Tb^{3+} lifetime suggests the removal of surface defects and related optical quenchers in the presence of organic ligand. High temperature synthesis of melamine-oxide hybrids compounds favours an OH- free strategy to obtain an effective improvement of lanthanides based nanoscaled phosphors.

The synthesis of organic/TiO_2 systems was carried out with different methods. Firstly, we analysed substituted-triazine /TiO_2 samples provided by the University of Gent. We demonstrated the feasibility of organic/inorganic core/shell system by ALD method and the interaction of triazine and oxides parts. We extended this architecture to the heptazine-based compounds using most friendly chemical methods.

Finally, we engineered a system based on organic/inorganic/organic heterostructures, evidencing the high degree of luminescence tunability for potential photonic applications.

We think that our research will be beneficial for the knowledge of fundamental properties of oxides and C_3N_4 compounds and we hope that these results will be an incentive towards the realization of organic/inorganic hybrids of high performaces for photocatalysis and photonic applications.

Appendix 1

Time-Resolved Luminescence

Photoluminescence spectroscopy measurements can be performed with two different approaches, depending on the excitation source characteristic. Two regimes can be identified: stationary and transient case. In the first situation, a continuous wave (CW) excitation is used and the excited level is populated with the same rate of the decay to the ground state, so the intensity is expected to remain constant [1]. In a transient regime, a pulsed excitation is used and the decay process from the excited to the ground state can be examined.

The population of the excited levels follow the time evolution general rule

$$\frac{dN(t)}{dt} = -A_T N(t)$$

$$A_T = A + A_{nr}$$

where A_T is the total decay rate and A and A_{nr} represent the radiative (Einstein coefficient of spontaneous emission) and non-radiative rate, respectively [1],[2]. Solving the equation and setting N_0 the density of excited centres at t = 0, we obtain

$$N(t) = N_0 e^{-A_T t}$$

Since the emitted intensity at t is proportional to excited centres we have

$$I_{em}(t) = C\text{x}A\text{x}N(t) = I_0 e^{-A_T t}$$

Consequently, the emitted intensity follows an exponential decay law with lifetime (or luminescence lifetime) equal to $\tau = 1/A_T$, the time necessary to lowering the di intensity I_0 (t=0) to I_0/e . As a result, we can write

$$\frac{1}{\tau} = \frac{1}{\tau_0} + A_{nr}$$

where $\tau_0 = 1/A$ is called radiative lifetime related to a perfectly radiative process ($A_{nr} = 0$).

It is important to realize that the transient luminescent emission can be more complicated than the one previously described. More complex decay laws, such as multi- or non-exponential decays, are observed [3] and by the studying and interpretation of the latters, relevant information can be acquired on the physical system [1].

Experimental techniques for time-resolved luminescence measurements

Gated technique. Gated technique consists in acquiring the emission spectrum at a certain delay time t, in respect to the excitation pulse and within a temporal gate Δt, so that the complete luminescence spectrum can be obtained at different times. Finally, by combining all of the spectra, the luminescence profile as a function of time is reconstructed (fig.A1.1) .

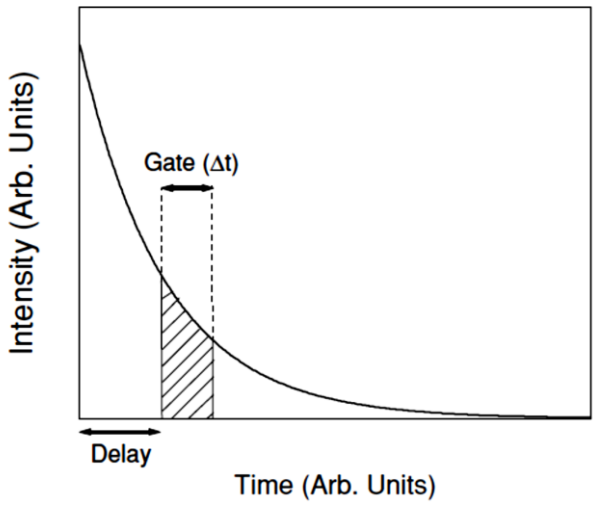

Figure A1.1: Principle of a typical gated measurement [1].

In our experiments the excitations wavelengths were provided by the emission of an optical parametric oscillator with frequency doubler device (Spectra Physics Quanta Ray MOPO-SL), with excitation energy ranging from 1064 nm to 250 nm, pumped by the third harmonic (355 nm) of a pulsed Nd-YAG laser (Spectra Physics QuantaRay PRO-270). The pulse width at half maximum was 8 ns with 10 Hz repetition rate.

After dispersion by spectrograph/monochromator designed with Image Czerney-Turner configuration (ARC Spectra Pro 300i), the luminescence spectra are monitored by a CCD (charge-coupled device) PI-MAX (Princeton Instruments). The PI-MAX is a time-gatable, image-intensified camera, with a 1024X256 pixel front illuminated CCD.

Streak camera for short signals. To handle with signal of the order of ps, we made use of a streak camera (fig. A1.2). The luminescence signal can be converted in electrons by the interaction with a photocathode. The electrons are accelerated by an electric field by a fast sweeping generator and then deflected before arriving on a phosphor screen, where they are reconverted in photons. The latters can be analysed by a CCD camera. Since the electrons emitted at different times are deviated at different angles, a time resolved image profile is thus achieved.

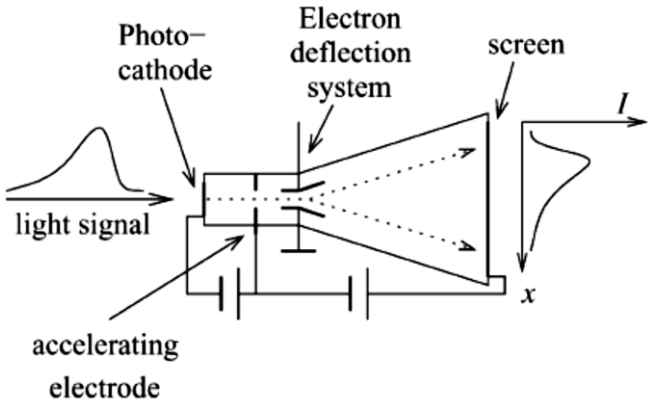

Figure A1.2: Principle of operation of a streak camera [2].

References

[1] J. Garcìa Solé, L.E. Bausà , D. Jaque. An Introduction to the Optical Spectroscopy of Inorganic Solids. Wiley. (2005)
[2] N. V. Tkachenko. Optical Spectroscopy: Methods and Instrumentations. Elsevier Science (2006).
[3] J. R. Lakowicz. Principles of Fluorescence Spectroscopy, Springer, (2006)

Appendix 2

Overview of Computational Methods

Contrary to configuration interaction (CI) or Møller–Plesset methods, density functional theory (DFT) has gained great popularity because of accurate calculations with less computationally cost [1].

DFT works on the concept of electron probability density

$$\rho(\boldsymbol{r}) = \sum_{i=1}^{n} |\psi_i(\boldsymbol{r})|^2$$

and on the expression of the electronic system energy in terms of the probability density. In other words, the total electronic energy can be expressed as a functional E[ρ].

From Kohn and Sham [2] we can write

$$E[\rho] = -\frac{\hbar^2}{2m_e}\sum_{i=1}^{n}\int \psi_i^*(\boldsymbol{r}_1)\boldsymbol{\nabla}_1^2\,\psi_i(\boldsymbol{r}_1)d\boldsymbol{r}_1 - \sum_{i=1}^{n}\int \frac{Z_I e^2}{4\pi\varepsilon_0}\rho(\boldsymbol{r}_1)d\boldsymbol{r}_1 + \frac{1}{2}\int \frac{\rho(\boldsymbol{r}_1)\rho(\boldsymbol{r}_2)e^2}{4\pi\varepsilon_0 r_{12}}d\boldsymbol{r}_1 d\boldsymbol{r}_2 + E_{XC}[\rho]$$

where ψ_i(i = 1, 2, …, n) are the Kohn-Sham (KS) orbitals (one electron spatial orbitals). The first term in the previous formula refers to the kinetic energy of electrons; the second one is the nucleus-electron interaction; the third term represents the total charge distribution at $\mathbf{r}_1$ and $\mathbf{r}_2$. Finally, the last term is the exchange-correlation energy of the system, a functional of the density taking into account the non-classic electron interactions [1]. KS orbitals are obtained by solving the KS equations for the one-electron orbitals

$$\left\{-\frac{\hbar^2}{2m_e}\boldsymbol{\nabla}_1^2 - \sum_{i=1}^{n}\frac{Z_I e^2}{4\pi\varepsilon_0} + \int \frac{\rho(\boldsymbol{r}_2)e^2}{4\pi\varepsilon_0 r_{12}}\,d\boldsymbol{r}_2 + V_{XC}(\boldsymbol{r}_1)\right\}\psi_i(\boldsymbol{r}_1) = \varepsilon_i\psi_i(\boldsymbol{r}_1)$$

where ε_i are the KS orbital energies and V_{XC} is the exchange-correlation orbital with the form:

$$V_{XC}[\rho] = \frac{\delta E_{XC}[\rho]}{\delta\rho}$$

Practically, KS equations are solved by self-consistence method in which an electron density ρ is firstly hypothesized. By the means of an approximate form for E[ρ], V_{XC} is calculated as a function of **r**. Then,

by knowing V_{XC} , we can obtain an initial set of KS orbitals that are used to compute an improved form of ρ and the process is reiterated until ρ and E_{XC} reach the convergence[1],[3] .

The approximate form of the functional for the exchange–correlation energy is generally composed by an exchange and a correlation part and it represents the principal source of error in the accuracy of calculations. At the ground level we can express the exchange–correlation energy in local-density approximation (LDA):

$$E_{XC} = \int \rho(\boldsymbol{r})\varepsilon_{XC}[\rho(\boldsymbol{r})]d\boldsymbol{r}$$

where ε_{XC} is the exchange-correlation energy per electron in a homogeneous electron gas of constant density. In this approximation the difference between computed and experimental data increases with the increase of electron density inhomogeneity and an approximation taking into account the gradient of ρ needs to be employed .

A large amount of exchange-correlation functionals have been proposed like B3LYP, MPW1K, BLYP, PBE. BLYP is for instance a combination of the gradient-correlated exchange functional of Becke [1],[4] and that developed by Lee, Yang and Parr[5]. B3LYP is an hybrid functional based on the use of Hartree-Fock corrections together with density functional correlation and exchange[1] with the form

$$E_{XC} = {E_{XC}}^{LDA} + a_0\left({E_X}^{HF} - {E_X}^{LDA}\right) + a_X\left({E_X}^{GGA} - {E_X}^{LDA}\right) + {E_C}^{LDA} + a_C({E_C}^{GGA} - {E_C}^{LDA})$$

where a_0 = 0.20, a_X = 0.72 and a_C = 0.81. ${E_X}^{HF}$ is the Hartree-Fock exact exchange functional

$$E_X^{HF} = -\frac{1}{2}\sum_{i,j}\iint \psi_i^*(\boldsymbol{r}_1)\psi_j^*(\boldsymbol{r}_1)\frac{1}{r_{12}}\psi_i(\boldsymbol{r}_2)\psi_j(\boldsymbol{r}_2)d\boldsymbol{r}_1 d\boldsymbol{r}_2$$

${E_X}^{GGA}$ and ${E_C}^{GGA}$ are generalized gradient approximations to account for the inhomogeneity of electron density.

The Electronic and vibrational calculations cannot neglect a preliminary geometry optimization process [3]. Structural changes in a molecule can generate significant differences in energy and related properties. The potential energy surface (PES), the mathematical relation between molecular structure and result energy, allows exploring the effects of slight changes in coordinates on the total energy.

As known, we can approach the solution of the Schrödinger equation for a molecular system by using the approximation of Born-Oppenheimer. Based on the difference between electrons and nuclei masses, it allows us to write the complete wavefunctions for the molecule as the product

$$\psi(\boldsymbol{x}, \boldsymbol{R}) = \psi_e(\boldsymbol{x}, \boldsymbol{R})\chi_n(\boldsymbol{R})$$

where ψ_e satisfies the Schrödinger equation in the field of fixed nuclei

$$H_e\psi_e(\boldsymbol{x}, \boldsymbol{R}) = E_e(\boldsymbol{R})\psi_e(\boldsymbol{x}, \boldsymbol{R})$$

and the nuclear wavefunction is solution of the equation

$$(T_n + E_e)\chi_n(\boldsymbol{R}) = E(\boldsymbol{R})\chi_n(\boldsymbol{R})$$

It follows that we are able to solve the Schrödinger equation for electrons in different nuclei arrangements. The solutions at distinct positions determine the construction of potential energy curve [1].

In general, it is a function characterized by maxima and minima. Local minimum represents a point in a limited region of low energy; in contrast, the global minimum is the lowest energy point on the whole potential surface and whose related physical properties we look for [1]. By the means of a geometry optimization, it is attempted to individuate local minima providing equilibrium structures of the molecules. In other words, when a molecular structure is proposed, energy and gradient of energy at that point are calculated. Then, the gradient indicates the direction along the PES in which the energy decreases most rapidly from the point. That process ends when a convergence is reached [1],[3].

Taking into account the harmonic oscillator model, every molecule has 3N-6 frequencies (3N-5 for linear molecules), excluding translations and rotations contributions. The minimum of energy is expected to be the zero point vibrational energy (ZPE), $\frac{1}{2}\sum_i \hbar\omega_i$ [6].

The calculation of frequencies starts with the 3N x 3N (N = number of atoms) Hessian matrix **f**, containing the second partial derivatives of the potential V with respect to the displacement of the atoms in cartesian coordinates

$$f_{ij} = \left(\frac{\partial^2 V}{\partial\xi_i \partial\xi_j}\right)_0$$

where ξ_1 , ξ_2, … ξ_{3N} are the displacement in cartesian coordiantes and thee derivatives are taken at the equilibrium positions of atoms [7].

f can be converted in weighted cartesian coordinates

$$f_{ij} \rightarrow f_{(mwc)ij} = \frac{f_{ij}}{\sqrt{m_i m_j}} = \left(\frac{\partial^2 V}{\partial q_i \partial q_j}\right)_0$$

where $q_i = \sqrt{m_i}\xi_i$ is the mass weighted cartesian coordinate, and then diagonalized providing 3N eigenvectors and 3N eigenvalues. The wanted frequencies are the square roots of the eigenvalues.

A scaling factor is then applied to correct the systematic errors introduced by the approximate form of exchange functional and by using finite basis set [8],[9].

To deal with electronic excites states, the DFT has to be extended to the time domain (TD-DFT). We will not discuss the formalism in this brief overview. However, it is worth to underline that, we do not need to know the electronically excited state and energy gradient, because of the nature of the vertical transition [10][11]. On the contrary, to estimate the emission transition from excited to ground state it is necessary to perform a further geometry optimization of the excited level. Even if the problem of fluorescence was not addressed in this work, we want to clarify the concept. In Figure A2.1 is reported the principle of the processes involved at the excitation of a molecular system. To make things easy, only the ground state and the first excited state are represented. According to Franck-Condon principle [1] an idealized vertical transition is expected when light is absorbed (1). The energy absorption determines an electronic transition of an electron to the first excited state. Out of equilibrium, the system relaxes to the energy minimum of geometric configuration at the excited level. Then the energy of molecule can decrease by emitting a photon (2) and relaxing to the low value of energy at the ground state.

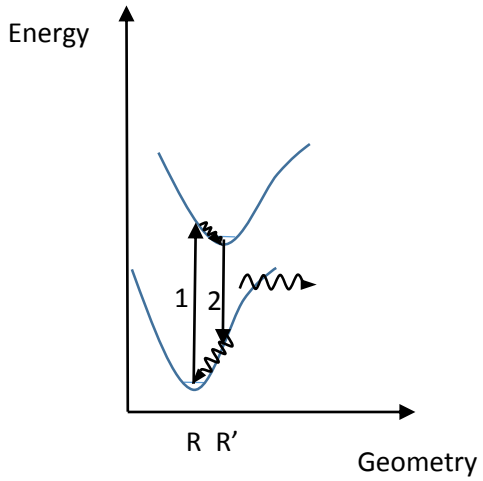

Figure A2.1: Simplified scheme of transition between ground and first excited state

References

[1] P.W. Atkins, R.F. Friedman. Molecular Quantum Mechanics. Oxford University Press. (2005)
[2] W. Kohn and L.J. Sham, Phys. Rev., 1133, A140 (1965).
[3] J.B. Foresman, A. Frish .Exploring Chemistry with Electronic Structure Methods. Gaussian, Inc. (1996)
[4] A.D. Becke, J. Chem. Phys., 4524, 84 (1986); Phys. Rev. A, 3098, 38 (1988).
[5] C. Lee, W. Yang, and R.G. Parr, Phys. Rev. B, 785, 37 (1988).
[6] R. S. Grev, C. L. Janssen, and H. F. Schaefer .J. Chem. Phys. 95, 5128 (1991)
[7] J.W.Ochterski. Vibrational Analysis in Gaussian. 1999 http://www.gaussian.com/g_whitepap/vib.htm
[8] A. P. Scott , L. Radom. J. Phys. Chem., 1996, 100 (41), 16502–16513
[9] Y. Tantirungrotechai, K. Phanasant, S. Roddecha, P. Surawatanawong , V. Sutthikhum, J. Limtrakul J. Mol. Struct.: THEOCHEM 760 (2006) 189–192
[10] R. Bauernschmitt, R. Ahlrichs Chemical Physics Letters 256 (1996) 454-464
[11] C.Adamo, D. Jacquemin. Chem. Soc. Rev. 2013,42,845

Acknowledgments

Luigi Stagi gratefully acknowledges Sardinia Regional Government for the financial support of his PhD scholarship (P.O.R. Sardegna F.S.E. Operational Programme of the Autonomous Region of Sardinia, European Social Fund 2007-2013 - Axis IV Human Resources, Objective l.3, Line of Activity l.3.1.).

Publications:

Anatase-to-Rutile Phase Transition in TiO_2 Nanoparticles Irradiated by Visible Light
P.C. Ricci, C.M. Carbonaro, L. Stagi, M. Salis, A. Casu, S. Enzo, F. Delogu
The Journal of Physical Chemistry C 117 (15), 7850-7857. (2013)

Surface Effects Under Visible Irradiation and Heat Treatment on the Phase Stability of γ-Fe_2O_3 Nanoparticles and γ-Fe_2O_3− SiO_2 Core–Shell Nanostructures
L. Stagi, J.A. De Toro, A. Ardu, C. Cannas, A. Casu, S.S. Lee, P.C. Ricci
The Journal of Physical Chemistry C 118 (5), 2857-2866. (2014)

Structure Solution of $NaYO_2$ Compound Prepared by Soft Chemistry from X-Ray Diffraction Powder Data.
L. Stagi, P. C. Ricci, D. Chiriu, E. Napolitano, S. Enzo
Chemical Engineering Transactions vol. 41 p. 409-414. (2014)

Selective Reading of Stored Information in RE doped Aluminium Perovskites
D. Chiriu, C. M. Carbonaro, R. Corpino, L. Stagi, P. C. Ricci
Crystal Research and Technology 50 (1), 43-48. (2015)

Light Induced TiO_2 Phase Transformation: Correlation with Luminescent Surface Defects
L. Stagi, C.M. Carbonaro, R. Corpino, D. Chiriu, P.C. Ricci
Physica Status Solidi (b) 252 (1), 124-129. (2015)

Luminescence Enhancement by Energy Transfer in Melamine-Y_2O_3: Tb^{3+} Nanohybrids
L. Stagi, D. Chiriu, A. Ardu, C. Cannas, C.M. Carbonaro, P.C. Ricci
Journal of Applied Physics 118 (12), 125502. (2015)

Towards the Development of New Phosphors with reduced content of Rare Earth Elements: Structural and Optical Characterization of Ce:Tb: Al_2SiO_5.
D. Chiriu, L. Stagi, C.M. Carbonaro, R. Corpino, M. F. Casula, P.C. Ricci
Materials Research Bulletin 77, 15-22. (2016)

Energy Transfer Mechanism Between Ce and Tb Ions in Sol-Gel Synthesized YSO Crystals
D. Chiriu, L. Stagi, C.M. Carbonaro, R. Corpino, P.C. Ricci
Materials Chemistry and Physics 171, 201-207. (2016)

Proceedings:

Surface effects and phase stability in metal oxides nanoparticles under visible irradiation
P.C. Ricci, C.M. Carbonaro, R. Corpino, D. Chiriu, L. Stagi
AIP Conference Proceedings 1624 (1) (2014)

Conference Participations:

Structural Phase Transformation in TiO_2 nanoparticles induced by visible light.
E-MRS Spring Meeting May 2014 Lille, France. Oral presentation
Surface Effects under Visible Irradiation and Heat Treatment on the Phase Stability of γ-Fe_2O_3 Nanoparticles and γ-Fe_2O_3 –SiO_2 Core-Shell Nanostructures. Poster session at E-MRS Spring Meeting May 2014 Lille France.
Mechanism of Phase Transformation in Magnetic/Silica Core/Shell Nanoparticles.
X Symposium SiO_2, Advanced Dielectrics and Related Devices June 2014 Cagliari, Italy. Oral presentation